1-1-2013

Mechanics of Interactions and Atomic-Scale Wear of Tips ian Amplitude Modulation Atomic Force Microscopy

Vahid Vahdat
University of Pennsylvania, vvahdat@seas.upenn.edu

Recommended Citation

Vahdat, Vahid, "Mechanics of Interactions and Atomic-Scale Wear of Tips ian Amplitude Modulation Atomic Force Microscopy" (2013). *Publicly Accessible Penn Dissertations*. 812.
http://repository.upenn.edu/edissertations/812

Mechanics of Interactions and Atomic-Scale Wear of Tips ian Amplitude Modulation Atomic Force Microscopy

Abstract

Wear is one of the main factors that hinders the performance of probes for atomic force microscopy (AFM), including for the widely-used amplitude modulation (AM-AFM) mode. Unfortunately, a comprehensive scientific understanding of nanoscale wear is lacking. We initially investigate and discuss the mechanics of the tip-sample interaction in AM-AFM. Starting from existing analytical formulations, we introduce a method for conveniently choosing an appropriate probe and free oscillation amplitude that avoids exceeding a critical contact stress to minimize tip/sample damage. We then introduce a protocol for conducting consistent and quantitative AM-AFM wear experiments. The protocol involves determining the tip-sample contact geometry, calculating the peak repulsive force and normal stress over the course of the wear test, and quantifying the wear volume using high-resolution transmission electron microscopy (TEM) imaging. The peak repulsive tip-sample interaction force is estimated from a closed-form equation accompanied by an effective tip radius measurement procedure, which combines TEM and blind tip reconstruction. The contact stress is estimated by applying Derjaguin-MÃ¼ller-Toporov contact mechanics model and also numerically solving a general contact mechanics model recently developed for the adhesive contact of arbitrary axisymmetric punch shapes. We discuss the important role that the assumed tip shape geometry plays in calculating both the interaction forces and the contact stresses. We find that contact stresses are significantly affected by the tip geometry, while the peak repulsive force is mainly determined by experimentally-controlled parameters, most critically, the free oscillation amplitude. The applicability of this protocol is demonstrated experimentally by assessing the performance of diamond-like carbon-coated and silicon nitride-coated silicon probes scanned over ultrananocrystalline diamond substrates in repulsive-mode AM-AFM. There is no sign of fracture or plastic deformation in the case of diamond-like carbon (DLC); wear could be characterized as a gradual atom-by-atom process. In contrast, silicon nitride wears through apparent removal of the cluster of atoms and plastic deformation. DLC's gradual wear mechanism can be described using reaction rate theory, which predicts an exponential dependence of the rate of atom removal on the contact average normal stress, allowing us to estimate kinetic parameters governing the wear process.

Degree Type
Dissertation

Degree Name
Doctor of Philosophy (PhD)

Graduate Group
Mechanical Engineering & Applied Mechanics

First Advisor
Robert W. Carpick

Keywords
AFM, AM-AFM, Contact Mechanics, Contact Stress, Tapping mode, Wear

Subject Categories
Mechanical Engineering

MECHANICS OF INTERACTIONS AND ATOMIC-SCALE WEAR OF TIPS IN AMPLITUDE MODULATION ATOMIC FORCE MICROSCOPY

Vahid Vahdat

A DISSERTATION

in

Mechanical Engineering and Applied Mechanics

Presented to the Faculties of the University of Pennsylvania

in

Partial Fulfillment of the Requirements for the

Degree of Doctor of Philosophy

2013

Supervisor of Dissertation

____

Robert W. Carpick, Professor and Chair, Mechanical Engineering and Applied Mechanics

Graduate Group Chairperson

____

Jennifer R. Lukes, Associate Professor, Mechanical Engineering and Applied Mechanics

Dissertation Committee:

Kevin T. Turner, Associate Professor, Mechanical Engineering and Applied Mechanics

Robert W. Carpick, Professor and Chair, Mechanical Engineering and Applied Mechanics

John L. Bassani, Richard H. and S.L. Gabel Professor of Mechanical Engineering

Daniel S. Gianola, Skirkanich Assistant Professor, Material Science and Engineering

MECHANICS OF INTERACTIONS AND ATOMIC-SCALE WEAR OF TIPS IN AMPLITUDE MODULATION ATOMIC FORCE MICROSCOPY

To my parents, Asad Baba and Nahid Maman, and my sisters, Kati and Soody, for your unconditional love and support.

ACKNOWLEDGMENTS

Professor Carpick, thank you for your support, understanding, and guidance in both my academic and personal life. You not only taught me science, but also showed me how to be a caring and kind person, positive, and make the best out of everything especially experimental data!

I also would like to thank Professor Arvind Raman, Dr. David S. Grierson, Dr. Tevis D. B. Jacobs, Graham E. Wabiszewski, Dr. Filippo Mangolini, and Dr. Vivekenanda P. Adiga for your useful and stimulating discussions on various topics during my studies at Penn.

I would also like to thank Dr. Andrew R. Koniceck and Dr. Philip Egberts for your comments and suggestions on my scientific writings and presentations.

I would also like to take the chance to thank the administrative staff in the Department of Mechanical Engineering and Applied Mechanics, including Susan W. Pilder, Maryeileen B. Griffith, and Desirae Johnson. Thank you for your kindness and help over the course of my PhD. Consulting and talking with you have always calmed down my anxious mind before qualifying and proposal exams, departmental seminar, and dissertation defense.

Peter Szczesniak and Peter Rockett, Department of Machanical Engineering and Applied Mechanics technical staff, thank you for your technical advice and your readiness to build and fabricate research related devices.

Finally, I would like to thank Dawn Norris, Towne Business Office staff member, for your help to resolve my complicated visa issues when I started to work at Carpick research group.

ABSTRACT

MECHANICS OF INTERACTIONS AND ATOMIC-SCALE WEAR OF TIPS IN AMPLITUDE MODULATION ATOMIC FORCE MICROSCOPY

Vahid Vahdat

Professor Robert W. Carpick

Wear is one of the main factors that hinders the performance of probes for atomic force microscopy (AFM), including for the widely-used amplitude modulation (AM-AFM) mode. Unfortunately, a comprehensive scientific understanding of nanoscale wear is lacking. We initially investigate and discuss the mechanics of the tip-sample interaction in AM-AFM. Starting from existing analytical formulations, we introduce a method for conveniently choosing an appropriate probe and free oscillation amplitude that avoids exceeding a critical contact stress to minimize tip/sample damage. We then introduce a protocol for conducting consistent and quantitative AM-AFM wear experiments. The protocol involves determining the tip-sample contact geometry, calculating the peak repulsive force and normal stress over the course of the wear test, and quantifying the wear volume using high-resolution transmission electron microscopy (TEM) imaging. The peak repulsive tip-sample interaction force is estimated from a closed-form equation accompanied by an effective tip radius measurement procedure, which combines TEM and blind tip reconstruction. The contact stress is estimated by applying Derjaguin-Müller-Toporov contact mechanics model and also numerically solving a general contact mechanics model recently developed for the adhesive contact of arbitrary axisymmetric punch shapes. We discuss the important role that the assumed tip shape geometry plays in calculating both the interaction forces and the contact stresses. We find that contact stresses are significantly affected by the tip geometry, while the peak repulsive force is mainly determined by experimentally-controlled parameters, most critically, the free oscillation amplitude. The applicability of this protocol is demonstrated experimentally by assessing the performance of diamond-like carbon-coated and silicon nitride-coated silicon probes scanned over ultrananocrystalline diamond substrates in repulsive-mode AM-AFM. There is no sign of fracture or plastic deformation in the case of diamond-like carbon (DLC); wear could be characterized as a gradual atom-by-atom process. In contrast, silicon nitride wears through apparent removal of the cluster of atoms and plastic deformation. DLC's gradual wear mechanism can be described using reaction rate theory, which predicts an exponential dependence of the rate of atom removal on the contact average normal stress, allowing us to estimate kinetic parameters governing the wear process.

TABLE OF CONTENTS

LIST OF TABLES

LIST OF ILLUSTRATIONS

Chapter 1 : Introduction

Since its revolutionary invention in 1986 by Binnig *et al.*,[1] the atomic force microscopy (AFM) has been one of the most powerful tools in nanotechnology. It has been widely used for atomic-scale studies of chemical, biological, and engineering materials, and has opened major opportunities for the advancement of nanoscale science. AFM has three primary operation modes for obtaining topographic images and material property measurements of samples: contact mode, non-contact mode (sometimes called frequency modulation AFM – FM-AFM), and intermittent-contact or amplitude modulation AFM (AM-AFM, also known as tapping mode AFM), where the latter two involve an oscillating cantilever. Over the last decade, AM-AFM has become the most popular imaging mode because of its minimal interaction with the sample, its relative ease of use, and its ability to obtain high resolution images of materials. More recently, the use of oscillating probes has emerged in industry as a tool to facilitate nanoscale lithography, patterning, manipulation, surface characterization, and metrology.[2–7]

The mechanics of AM-AFM have been widely investigated by researchers since being introduced in 1987 by Martin *et al.*[8] Most of these studies have focused on understanding the dynamics of AM-AFM. Tip-sample interactions due to van der Waals forces, capillary forces, *etc.* have also been studied broadly, although there are aspects of tip-sample interactions still not yet fully understood. Continuum contact mechanics models such as the Hertz,[9] Johnson-Kendall-Roberts (JKR),[10] and Derjaguin-Müller-Toporov (DMT)[11] models are typically applied to estimate stresses and deformations at the tip-sample interface. These models assume, among other things, that the tip terminates in a paraboloidal shape. Clearly, for an arbitrary punch shape, as in the case of AFM tips, a more general approach is necessary to precisely capture the mechanics of interaction. While such continuum mechanics models could be inaccurate when applied to nanoscale geometries, they can give reasonable values in several cases depending on the atomic structure of the tip and sample (according to Luan and Robbins[12]). Considering the lack of a general atomistic method and the unknown atomic structure of the tip and surface, continuum models are a significant improvement over existing state-of-the-art which often does not even address stresses in the contact during AM-AFM.

1.1: Overview of the Importance of Wear

One of the major limitations for AFM is probe-tip blunting as a result of nanoscale wear. Wear is also problematic for soft samples, such as polymers and biological materials, which are of great interest for interrogation by AFM, as they typically possess nanoscale structural features not easily accessible by other material characterization methods. Wear of both sample and tip during contact mode imaging has been examined in multiple studies, although it is yet to be fully understood.[13–18] AM-AFM was invented in part to reduce the problem of wear by nearly eliminating shear stresses acting on the tip due to sliding (intrinsically present in contact mode imaging), and reducing the total amount of time the tip interacts strongly with the sample. However, these advantages could be offset by the high frequency of the cantilever oscillations, which can be on the order of hundreds of thousands of tip-sample contacts per second.

Having many cycles of interaction is not intrinsically a problem by itself; however, the effect of any gradual process such as atom-by-atom removal or dislocation movement can scale up as a result. Therefore, tip wear can still be a limiting and costly factor in AM-AFM. Consequently, users often have to periodically replace probes to maintain high and consistent imaging resolution. A changing tip makes quantitative analysis of tip-sample interactions and sample property measurements challenging since tip-to-tip variations in shape and surface composition can be substantial.

Despite the importance of wear in AM-AFM as well as in other oscillating-probe applications, there are limited systematic studies on the phenomenon of tip wear itself. This motivates the present study, which is focused on developing and deriving novel insights from a new method for a controlled wear studies with accurate determination and control of the tip-sample interaction forces and the resulting stresses. Another motivation is application-driven. In tip-based nanomanufacturing and metrology, which can involve AM-AFM operation of the probe, wear must be avoided for the process to be commercially viable. Silicon as a common material utilized in microelectromechanical systems, which is also widely used to make sharp AFM tips, wears out rapidly at the nanoscale.[14–16] More wear-resistant materials such as ultrananocrystalline diamond (UNCD)[19] and silicon carbide, for example, are potential candidates to replace silicon. Understanding wear mechanisms will provide guidance for developing new wear-resistant materials.

At the nanoscale, there are three primary wear mechanisms that have been identified: fracture,[14,20] plastic deformation,[21] and atom-by-atom removal.[16,18,22] All of these mechanisms could exist in both contact mode and AM-AFM. However, how these mechanisms occur and which one(s) dominates strongly depends on the stress state and the nature of tip-sample interactions at the contact. In contact mode, tip wear occurs during sliding and is influenced by the magnitude of stresses in the contact and the nature of the interfacial interactions. The causes of wear in AM-AFM can be quite different. While interfacial shear stresses are significantly reduced, the effects of cyclic loading and impact, uniquely related to repeated contact formation and breakage of AM-AFM, and the potential for excursions to high compressive stresses may lead to distinct types of wear processes compared with contact mode AFM. Besides tip wear, tip contamination is also an important issue when it comes to reliable application of AFM[15,23–27] but that requires a different comprehensive approach than what is discussed here.

1.2: Amplitude Modulation Atomic Force Microscopy

In AM-AFM, a cantilever is excited at or near its primary flexural resonance frequency by a piezoelectric actuator. When far from the sample, the oscillation amplitude is called the free amplitude, A_0; while approaching the sample, the oscillation amplitude reduces as a result of tip-sample interaction. During approach, the amplitude continues to reduce until it reaches a value set by the user. This designated amplitude is called the amplitude setpoint or tapping amplitude, A. While scanning a surface, the oscillation amplitude tends to change as a result of interacting with topographic features. The AFM feedback loop monitors the oscillation amplitude and keeps it constant by adjusting the height of the sample continuously. The quality of the image, and the precision to which the amplitude setpoint is maintained, is therefore determined by the feedback loop. During scanning, the variation of the material properties depending on its magnitude could create artifacts in the topography image. Some of these artifacts come from different tip-sample deformation, adhesion, viscoelasticity, and roughness at the contact. Some of the changes in material properties are mainly observable in the phase image.

In AM-AFM, as the tip approaches and then retracts from a surface during a tapping cycle, it experiences two different force regimes (Figure 1.1): when far from the sample's surface, the tip experiences long-range attractive forces, mainly as a result of the van der Waals interaction with the sample; when close to the sample's surface, the tip experiences short-range repulsive forces as a result of Pauli and electrostatic repulsion, and strong short-range attractive forces as a result of metallic, covalent, ionic, or hydrogen bonding interactions for example. Capillary interactions can also contribute to attractive forces over intermediate separation ranges. The maximum repulsive (*i.e.*, normal) force is experienced by the tip during contact when it reaches its farthest distance away from its equilibrium position. Finally, the cantilever begins to pull it away from the sample. Then, the same sequence of the tip-sample force regimes are passed through in reverse.

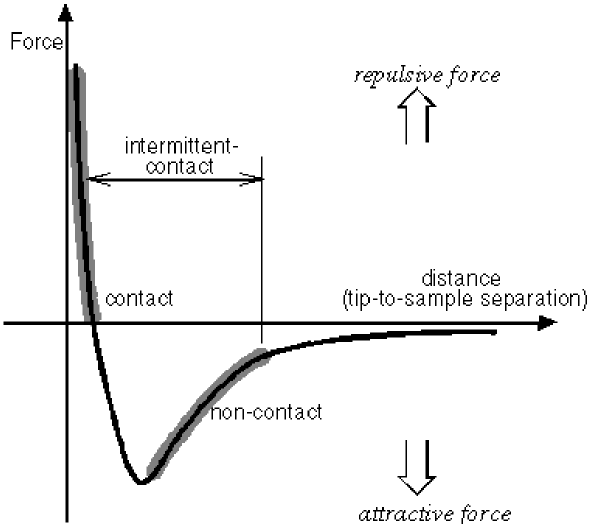

Figure 1.1: Inter-atomic force vs. distance curve. Image is taken from a Veeco Instruments Inc. guide to scanning probe microscopy.[28]

To understand the physics of AM-AFM, one needs to consider the dynamic behavior of an oscillating cantilever as well as the tip-sample interaction. Researchers have frequently simulated the dynamic response of the AFM cantilever as a point-mass-spring model with one degree of freedom, driven by an external sinusoidal signal. The equation of motion includes the contribution of the cantilever's elastic response, the hydrodynamic damping due to the medium, the tip-sample interaction, and the excitation force. These terms appear in the following equation:

$$m_{eff}\frac{d^2z(t)}{dt^2}+kz+\frac{m_{eff}\omega_0}{Q}\frac{dz}{dt}=F_{ts}+F_{drive}\cos(\omega t). \tag{1.1}$$

where z is the instantaneous tip displacement, m_{eff} is the cantilever effective mass, k is the cantilever's spring constant, ω_0 is the angular resonance frequency, Q is the quality factor, F_{ts} is the tip-sample interaction force, F_{drive} is the driving force amplitude, and ω is the angular frequency of the driving force. The use of cantilever effective mass instead of actual mass originates from that fact that the cantilever body does not oscillate with the same amplitude along its full longitudinal length. The effective mass is calculated to be $\frac{33}{140}m$, where m is the cantilever's real mass, and is arrived at by equating the kinetic energy of the oscillating cantilever to that of the lumped-mass model. Care should be taken while using this equation as it ignores the contribution of the higher harmonics in the cantilever motion. This simplification does not create a fundamental problem simulating AM-AFM as the cantilever is operated at or near its first harmonic. Changes in the hydrodynamic damping of the cantilever during its motion are neglected in this modeling.[29]

The tip-sample interaction can be expressed by the following equation. The attractive forces arise from van der Waals interactions and the DMT contact model describes the repulsive portion of the contact force:

$$F_{ts}(z_c, z) = \begin{cases} -\dfrac{HR}{6\left(z+z_c\right)^2} & \text{for } z+z_c > a_0 \\ -\dfrac{HR}{6a_0^2} + \dfrac{4}{3}E^*\sqrt{R}(a_0 - z - z_c)^{\frac{3}{2}} & \text{for } z+z_c \le a_0 \end{cases},$$

$$\text{where} \qquad \frac{1}{E^*} = \frac{(1-\nu_t^2)}{E_t} + \frac{(1-\nu_s^2)}{E_s}$$

(1.2)

where H is the Hamaker constant, R is the tip radius, $(z + z_c)$ is the instantaneous tip-sample separation, a_0 is the intermolecular distance, E_t and E_s are Young's moduli for the tip and sample, and ν_t and ν_s are Poisson's ratios for the tip and sample.[29] z_c and z are shown in Figure 1.2.

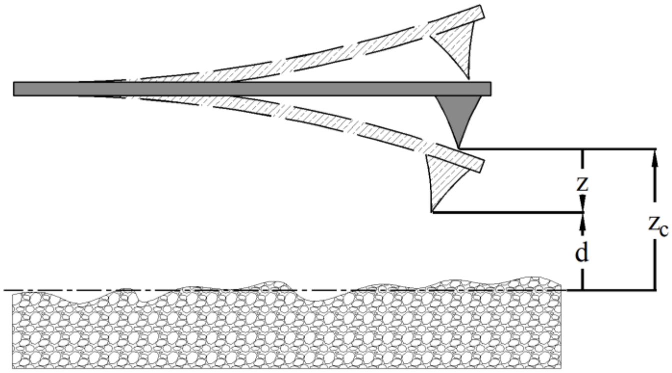

Figure 1.2: Scheme of cantilever-tip sample positions.

Numerical simulations of the cantilever response using the above equation of motion reveal some interesting characteristics of the AM-AFM. For example, the presence of both attractive and repulsive interactions and their nonlinear character creates two stable oscillation states (Figure 1.3). These oscillation states are called the high amplitude solution or repulsive regime, and the low amplitude solution or attractive regime. If the average force experienced by the tip during a cycle is attractive (negative), the cantilever operates in the low amplitude state. On the other hand, if the average force is repulsive (positive), the cantilever oscillates in the high amplitude state. In other words, there are two tip-surface separations that can attain the same stable tapping amplitude (Figure 1.3).

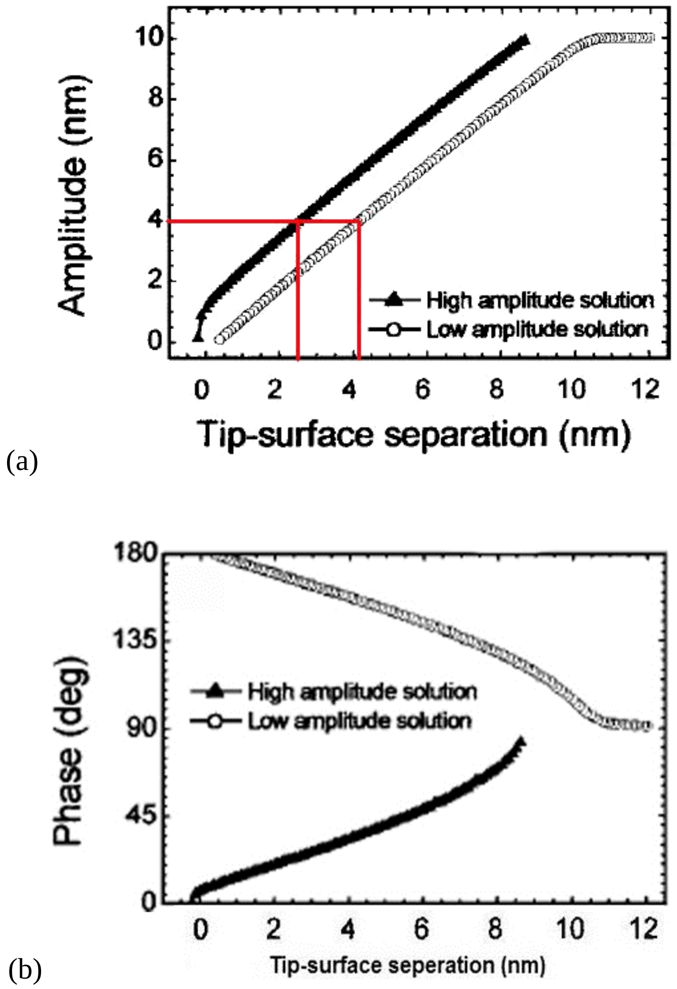

Figure 1.3: (a) Amplitude and (b) phase as a function of tip-surface separation. The coexistence of two solutions for different tip-surface separations gives rise to the formation of branches. Image is taken from García *et al*.[30]

Transitions between these states are affected by the deterministic character of the equation of motion, the presence of perturbations (noise), and the basins of attraction of the two tapping states.[30] The basins of attraction refer to the two regions of the tip motion phase space which can be determined from nonlinear dynamics analysis. If the basin of attraction of an oscillating state dominates the phase space, it is unlikely that the perturbations trigger a transition to the other state. However, if both states contribute nearly equally in the phase space, the presence of noise can create instability and frequent transitions between the states. In other words, the deterministic character of the equation of motion implies that once a stable state is reached, the tip should oscillate indefinitely there. However, a perturbation could disturb the tip motion by introducing new initial conditions.[31] These transitions are shown from actual experimental data obtained here in Figure 1.4.

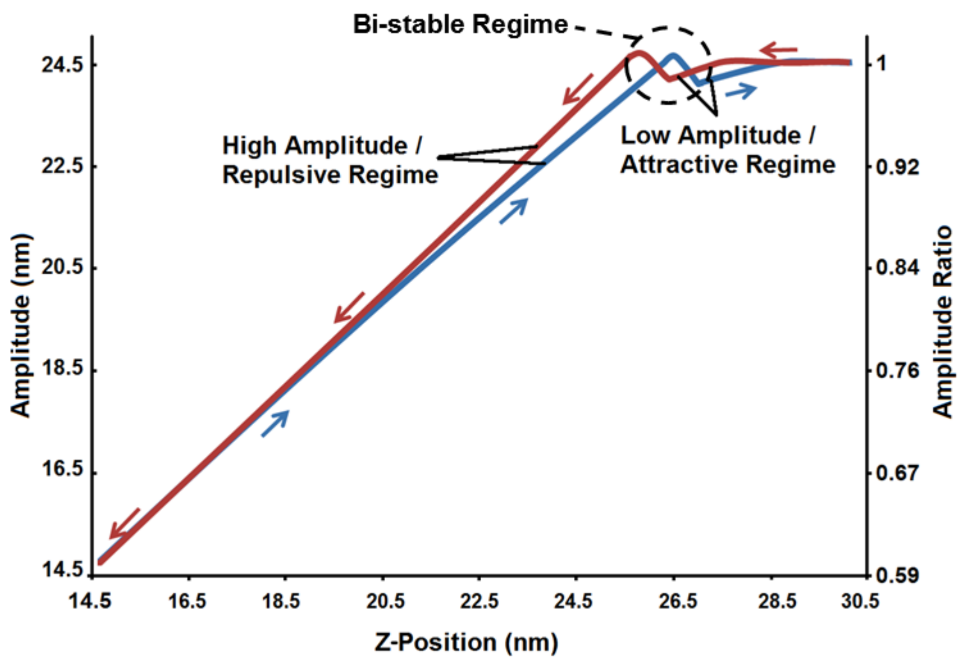

Figure 1.4: Amplitude curve (approach and retraction) taken on a UNCD sample using a silicon tip with 24.5 nm free oscillation amplitude. The transition between the two branches happens at different z-positions upon approach and retraction.

In addition to the oscillation state, attractive and repulsive regimes shift the resonance frequency of the cantilever (Figure 1.5). The effective resonance frequency of a cantilever interacting with a surface can be approximately calculated by

$$\omega_e = \left(\frac{k - (dF_{ts} / dz)}{m_{eff}} \right)^{\frac{1}{2}} . \tag{1.3}$$

The approximation comes from the assumption that the tip-sample interaction potential is parabolic.

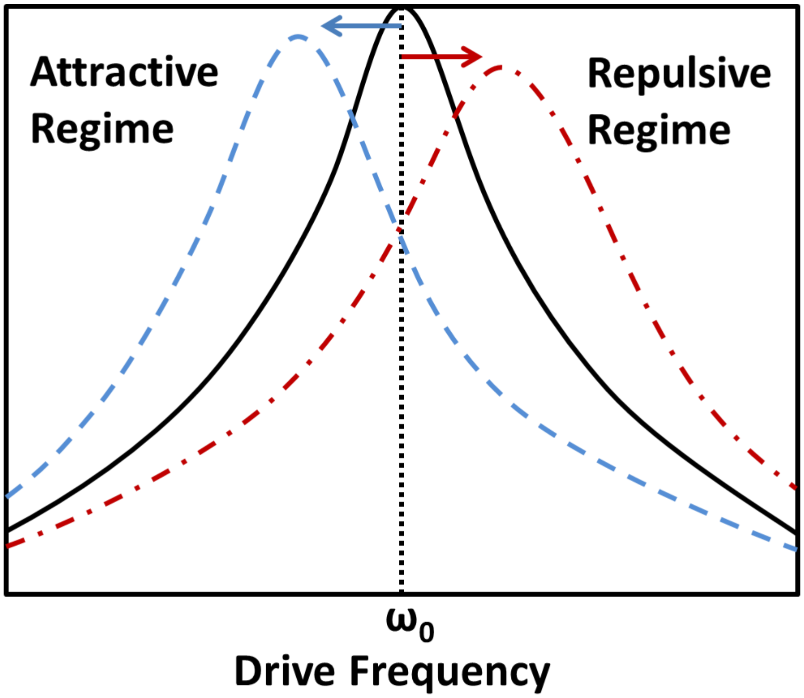

Figure 1.5: Resonance curve for a harmonic oscillator (solid black line) and under the influence of attractive (dashed blue line) and repulsive forces (dash-dotted red line).

The shift in resonance frequency is responsible for the amplitude reduction that occurs when the cantilever approaches the surface and for the presence of two steady-state solutions in AM-AFM. As the cantilever is oscillated at a fixed frequency near or equal to its resonance frequency, the shift in resonance frequency moves the oscillation off resonance, resulting in amplitude reduction. If the oscillation is dominated by the attractive force or the repulsive force (which is dependent on the tip-sample separation), the resonance frequency shifts lower or higher, respectively (Figure 1.5).

1.3: Previous Studies of Wear in AM-AFM

Existing studies of the wear of AM-AFM probes to date involved experimental investigations of wear reduction by using different tip materials[32,33] or by controlling the AM-AFM parameters,[34] and modeling wear as a thermally activated process.[35] Su *et al.*[34] showed that operating in hard tapping regime with a relatively low amplitude ratio (tapping amplitude divided by free oscillation amplitude) has the advantage of reducing tip wear and increasing the scanning speed as opposed to operating with a high amplitude ratio (*i.e.*, close to free amplitude). They also found that by decreasing the amplitude setpoint the interaction force goes through a maximum and then reduces as the low amplitude setpoint is approached. This implies that 50-60% oscillation damping is the most damaging condition as the tapping velocity is maximum. They verified this by performing a set of wear tests on silicon probes scanning titanium flakes, which is a sample with hard and sharp features. With the relative amplitude setpoint equal to 0.5, they demonstrated faster tip wear observable through degradation of lateral resolution in the topographic image. This work sheds light on some of the experimental parameters affecting tip wear. However, it does not explain the wear process in a quantitative and predictive way, since the tip geometry, the tip-sample deformation, and the attractive/repulsive force regimes are not included in the analysis.

Bassani and D'Acunto[35] performed analytical modeling of wear in AM-AFM. They considered wear as an irreversible atom-by-atom mass transfer from the sample to the tip as a result of adhesive interactions. The tip-sample interaction was modeled as a double-well potential, and mass transfer was treated as a transition between the two potential wells. They calculated wear volume as an exponential function of the energy barrier, and predicted that the wear rate of a single atomic volume in the model depends on an Arrhenius rate law, which describes a thermally activated wear process. This model represents an important first step since previously such effects on the process of material removal had not been modeled from an atomistic point of view. However, the model neither considers atoms that can move from the tip to the sample, nor does it consider diffusion of atoms from one region of the tip (or the sample) to another region without transferring across the interface. In addition, the model does not take into account the elastic deformation of the tip and sample, and that mass transfer can occur via removal of clusters of atoms instead of single atoms. Although these complex issues are not addressed, this model is useful because it introduces a framework for modeling gradual wear processes in AM-AFM. To develop further insights, we must consider other parameters like contact stresses and radius that promote and determine the reaction rate besides the adhesion.

To highlight the key issues one might encounter and should take into account while studying wear in AM-AFM, in the following chapters we first discuss available analytical models to estimate contact forces and stresses, and propose methods to apply them accurately by discussing parameters that may affect the results. We then explore the manifestation of these calculations in practice and examine the influence of the various parameters involved by performing wear experiments with different probes as a function of different experimental parameters.

Chapter 2 : Mechanics of the Tip-Sample Interaction

Quantification and control of the interaction forces and the resulting stresses on the tip are crucial for AFM tip wear studies. As discussed previously, the maximum repulsive normal force is experienced by the tip during contact when it reaches its farthest distance away from its equilibrium position (*i.e.* cantilever's rest position). At this point of highest normal stress and overall strain energy, the tip has the greatest potential to become damaged. Therefore, the most relevant interaction force for studying AM-AFM wear is the peak repulsive force.

2.1: Attractive Mode Imaging and Wear in AM-AFM

Although in attractive mode measurements, wear could potentially occur by atoms being pulled off from the tip, the long-range attractive forces at play are typically small compared to forces needed to break bonds. In a study by Tello *et al.*[36] it was demonstrated that repeated imaging of cobalt nanoparticles in attractive mode did not change the height and width of the particles while imaging in repulsive mode permanently changed their height. Although in this study, the contact forces and stresses were not controlled in the repulsive regime imaging to avoid sample deformation, it confirms that forces in attractive regime are not significant enough to cause any form of deformation. So, attractive forces are not considered to be significant in tip wear.

Here, one might question why all the AM-AFM experiments are not done in attractive regime to avoid any tip/sample wear and deformation. There are several issues that make imaging in attractive regime either impossible or undesirable. As mentioned before, in attractive regime imaging the attractive forces dominate repulsive forces. In a lot of cases depending on the tip and sample elastic properties, cantilever's physical properties, and AM-AFM experimental settings, the range of amplitude ratios that attractive forces dominate repulsive forces is very short. Sometime even the attractive regime does not exist and the tip-sample interaction jumps into the repulsive mode as soon as the interaction begins. This short range of amplitude ratio's makes stable imaging (*i.e.* effectively tracking of the sample features and avoiding bi-stability) very difficult (Figure 1.4).

In the cases that there is a wide range of amplitude ratios where the tip-sample interaction is in attractive regime, the tip broadening[37] (*i.e.* showing the features wider than their real size because of the fact that attractive forces are long-range. This is in addition to the effect of the tip finite size on the sample's features size which will be discussed in section 3.1) or losing track of the surface makes attractive imaging in a lot of cases undesirable. Losing track of the surface can cause image artifacts and out of control impact of the tip with surface resulting in the tip damage.[34] This problem arises from the fact that the transient time for amplitude error to reach equilibrium exponentially increases as the amplitude ratio approaches 1, which is required for attractive imaging in most cases. And whenever there is a transient component in the amplitude error, it can be falsely interpreted as the sample features resulting in the losing track of the surface by the control system.[34]

In the following section, a literature review of the current techniques used to quantify tip-sample forces in AM-AFM will be discussed.

2.2: Peak Repulsive Force

Measuring the normal force acting on a tip is rather complicated in AM-AFM due to the dynamic and nonlinear tip-sample interactions, compared to the same measurement performed in contact mode. Several studies examining tip-sample interactions in AM-AFM have attempted to resolve this issue.[38–41] However, to date, a straightforward technique which is accurate over the entire range of tip-sample separations and can be used directly during the course of AM-AFM experimentation has not been established. Below we review a force inversion technique proposed by Katan *et al.*[38] which uses the amplitude- and phase-distance curves acquired from approaching to and retracting from the sample surface to estimate force as a function of the tip-sample separation distance. We also discuss a closed-form analytical solution proposed by Hu *et al.*[40] which estimates peak repulsive force as a function of the cantilever and sample physical properties and experimental settings.

Katan *et al.*[38] extended a force inversion technique primarily derived for frequency modulation atomic force microscopy by Sader *et al.*[42] to AM-AFM. This technique was based on a point-mass and spring model of the AFM tip-cantilever and requires one to obtain data for the amplitude and phase as a function of the tip-sample separation distance. Although this technique does not require any information to be provided regarding the tip geometry and solely depends on the experimental measurements of the phase and amplitude as a function of z-motion, it is quite sensitive to small offsets of the phase data and miscalculates the interaction force in cases where the tip-sample interaction stiffness exceeds the cantilever stiffness.[39] In addition, it cannot be used in a straightforward, real-time manner by an AFM user during an experiment. Specifically, the interaction force cannot be deduced from the phase and amplitude images alone, as such images are acquired at a nominally fixed tip-sample distance. Rather, data corresponding to a range of tip-samples distances are required for the application of this method. These challenges make this technique unsatisfactory for the purpose of monitoring forces during wear studies.

Hu *et al.*[40] proposed closed-form equations for peak attractive and repulsive interaction forces derived from applying a nonlinear, dynamical one-term harmonic-balance method to the point-mass model. These equations are accurate over a wide range of experimental parameters, including various environments such as vacuum and air. Having closed-form equations to calculate peak interaction forces would be convenient for AFM users. However, these equations are limited to cases where the tip remains paraboloidal, and requires that the tip radius be accurately measured experimentally.

In the present work, the peak repulsive force experienced by our AFM tips in wear studies are estimated using equations developed by Hu *et al*. Given the importance of the tip shape to this method, we periodically characterize the tips using two independent techniques: high-resolution transmission electron microscopy (HR-TEM) and blind tip reconstruction (BTR). This requires interrupting the AFM experiment, removing the tip from AFM, transporting to the TEM, taking back to the AFM after TEM imaging and so on. This is a time-consuming, delicate, and fairly onerous task which affects throughput; however, it is necessary to accurately estimate the forces and stresses and calculate the wear volume. The procedure for quantifying the tip shape with these two techniques will be discussed in Section 3.1.

In determining the peak repulsive forces, we have assumed the DMT model.[11] Justification for the choice of a DMT contact model will be given in Section 4.1. The equation of motion of the point-mass spring model (Eq. (1.1)) and Eq. (1.2) to describe the tip-sample forces are used to predict peak repulsive force using asymptotic theory of the periodic averaging. In this theory, the driving, interaction, and damping forces are assumed to be small perturbations to an undamped harmonic oscillator. Then, the time-averaged effects of the forces and the frequency detuning between drive and oscillator resonance frequencies are used to determine the response of the harmonic oscillator. All the assumptions used for the DMT contact model described in the section 2.2 apply to the derivation of the following equation. Also, it is assumed that F_{ts}/k and F_{drive}/k are very small and negligible in compare to the tip oscillation amplitude.[40] Given the DMT contact mechanical model, the equation for the peak repulsive force is as follows:

$$\begin{aligned} F_{peak}^{rep} \approx\ & 2^{\frac{1}{8}} 3^{\frac{-1}{4}} \pi^{\frac{3}{4}} \left(E^{*}\sqrt{R}\right)^{\frac{1}{4}} \left(k/Q\right)^{\frac{3}{4}} A_{0}^{\frac{9}{8}} A_{ratio}^{\frac{9}{8}} \\ & \times \left\{ \left(-1+\Omega^{2}\right)Q + \sqrt{\frac{1}{A_{ratio}^{2}}\left[\Omega^{2} + \left(1-\Omega^{2}\right)^{2} Q^{2}\right] - \Omega^{2}} \right\}^{\frac{3}{4}}, \\ & - F_{adhesion}/2 \end{aligned}$$

(2.1)

where E^{*} is the reduced Young's modulus, R is the tip radius, k is the cantilever spring constant, Q is the cantilever's quality factor for the primary flexural mode, A_0 is the free oscillation amplitude, A_{ratio} is tapping amplitude A divided by A_0, Ω is drive frequency ω divided by resonance frequency of the primary flexural mode ω_0, and $F_{adhesion}$ is the adhesion force.[40] All the above mentioned parameters except adhesion force are discussed in Chapter 1. Here, $F_{adhesion}$ is also calculated using the DMT model:

$$F_{adhesion} = -2\pi w R\,.$$

(2.2)

where w is the work of adhesion, which is determined independently by performing pull-off force measurements using tips of the same type from the same vendor, *i.e.*, composed of the same material as the tips studied in the wear experiment. This is described in section 3.2.1.

To verify the accuracy of the equation, one can use an online tool developed by Melcher *et al.*[41], provided by http://nanohub.org, and called the Virtual Environment for Dynamic AFM (VEDA). This tool numerically solves the Euler-Bernoulli partial differential equation of a thin cantilever beam to construct amplitude and phase approach curves and to calculate the peak repulsive/attractive forces for a given set of experimental parameters. It also provides a more accurate estimation of forces since it does not involve the same mathematical approximations used to derive Eq. (2.1).

2.3: Contact Mechanics Model and Average Normal Stress

Before calculating interaction forces and stresses in any contact mechanics problem, an appropriate model needs to be chosen. In AM-AFM, initially one needs to investigate if the tip-sample impact can be considered to be quasi-static. If the impact is quasi-static, then the well-developed contact mechanics models derived for static contact problems can be safely applied to AM-AFM. According to Johnson, dynamic effects of an impact can be ignored or assumed to be quasi-static if the contact time is either short or long compared with the time required for the elastic wave to travel back and forth through the impacted object.[9] The next paragraphs examine the suitability of this assumption in AM-AFM contact mechanics.

The shortest estimated contact time (using VEDA) in AM-AFM experiments typically measured in this thesis is about 0.13 μs. Given the longitudinal elastic wave speed in silicon is equal to 8.43×10^5 cm/s, the elastic stress wave should oscillate through the height of the tip and the thickness of the cantilever, which is 22 μm corresponding to the tallest possible tip of the probes used in this thesis, at least 50 times during the 0.13 μs contact time. In other words, in AM-AFM, the tip-sample contact time is long compared with the time required for the elastic wave to travel back and forth through the impacted object. Therefore, the quasi-static assumption for our dynamic problem in AM-AFM is valid and allows for the use of static contact mechanics models to describe the stress distribution in the vicinity of the contact area ignoring the inertial effects.

In contact mechanics models, it is normally assumed that the tip and sample are composed of homogeneous, isotropic, linear elastic materials, and that the tip shape is a paraboloid. It is also assumed that deformations in the surface and tip are small compared to the contact radius, which in turn is small compared to the tip's radius of curvature. One then needs to calculate the Maugis parameter, λ, and the non-dimensional load, $\bar{P}$, and use the adhesion map proposed by Johnson and Greenwood[43] to select the proper contact mechanics model. The Maugis' parameter, λ, and the non-dimensional load, $\bar{P}$, are calculated as follows:[43]

$$\lambda = 1.16\left(\frac{Rw^2}{E^{*2}z_0^3}\right)^{\frac{1}{3}}, \tag{2.3}$$

$$\bar{P} = \frac{P}{\pi w R}. \tag{2.4}$$

where z_0 is the equilibrium separation and P is the normal load, which in this case is the peak repulsive force. As will be shown in the section 4.1, our tip and sample interaction are best described by the DMT contact model.

In a DMT-like contact the normal contact stress distribution is similar to that of Hertz theory and has a parabolic form (Figure 2.1). However, including the adhesion between the contacting bodies results in larger stress values and contact area (Figure 2.1 and Figure 2.2(a)). Also, at zero applied load, the contact area and stresses are not zero in a DMT-like contact (Figure 2.2).

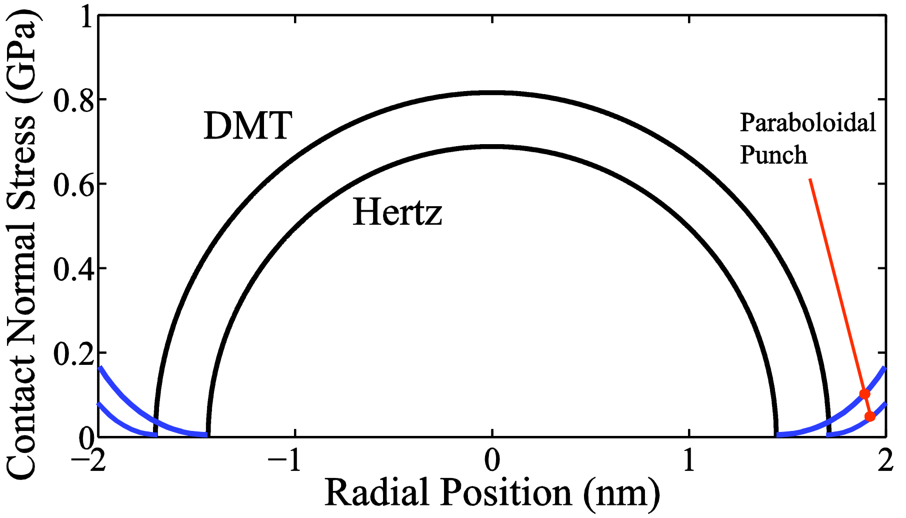

Figure 2.1: The Hertz/DMT normal stress distribution at the contact plotted by setting E^* = 0.75 GPa, R = 1 nm, πw = 1 J/m^2, and the normal applied load equal to 3 nN. In a DMT-like contact the normal contact stress distribution is similar to that of a Hertzian contact with a parabolic form. The larger stress values in the case of DMT come from adding the adhesion force to the normal applied load.

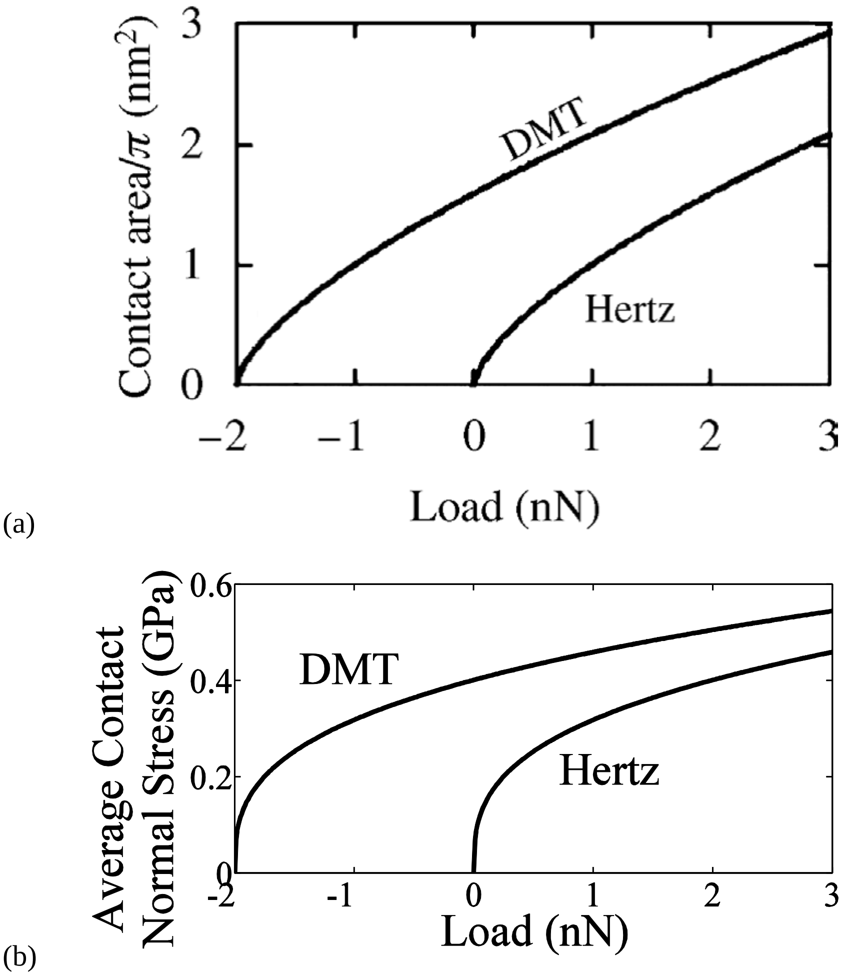

Figure 2.2: The Hertz/DMT (a) area–load and (b) average contact normal stress–load curve plotted by setting E^* = 0.75 GPa, R = 1 nm and πw = 1 J/m^2. The DMT approaches the Hertz curve in the limit $w \rightarrow 0$ (no adhesion). In (a) adhesion increases the contact area from the Hertz case for a given load by an amount dependent upon the range of attractive forces. (a) is taken from Grierson *et al.*[44] and modified to be presented here. In (b), because of the adhesion, the contact stress is not zero at zero applied load for the DMT case.

Using DMT model, the average normal stress, when the tip is at its farthest distance away from its equilibrium position, is calculated to be:

$$\sigma_{avg}^{norm} = \frac{1}{\pi}\left(\frac{4E^*}{3R}\right)^{\frac{2}{3}}\left(F_{peak}^{rep} - F_{adhesion}\right)^{\frac{1}{3}}.$$

(2.5)

Comparing this equation with Eq. (2.1), one can recognize that the dependence on tip radius is stronger in the stress calculation as compared to the repulsive-force calculation. In Eq. (2.1), *R* is raised to the power of 1/8, while in Eq. (2.5) *R* is raised to -5/8 (= -2/3 + (1/8)(1/3)), a factor of 5 larger. It should be mentioned that the values of the force and stress are dominated by the first terms in Eq. (2.1) and (2.5); therefore, the dependence of the second term, $F_{adhesion}/2$, on *R* does not significantly contribute to the calculation of the force and stress. This shows how errors in the determination of the tip geometry (or deviation of the tip shape from paraboloidal) can greatly influence the stress calculation. As will be demonstrated in the following HR-TEM images, AFM tips are not always simple spheres or paraboloids and can have nanoscale roughness. Additionally, they are often not axisymmetric. Thus, imposing contact mechanics models that assume a simple tip shape can introduce significant errors in the calculation of the stress.

To mitigate this issue, in the present work, the average normal stress and correspondingly the contact radius and deformation are also calculated numerically by solving a general contact mechanics model proposed by Zhou *et al.*[45] for the adhesive contact of arbitrarily shaped axisymmetric punches described in the following section and section 3.5.

2.3.1: Average Normal Stress of an Axisymmetric Arbitrary Punch Shape

As the AFM tip apices are not always simple smooth paraboloids, it is important to consider the difference between the stress calculated by simply fitting a paraboloid to the tip apex and the stress calculated using a line fit to the actual tip profile. As mentioned earlier, we use the solution presented by Zhou *et al.*[45] for an axisymmetric arbitrary punch shape. All the classic contact mechanics models, including Sneddon's and Boussinesq's solutions, are special cases of the proposed solution. To solve this adhesive contact problem (Figure 2.3(a)), Zhou *et al.* superpositioned two contact problems with different boundary conditions. One of the contact problems was a rigid punch pushing against an elastic half space with displacement prescribed inside the contact zone similar to that of a Hertzian contact (Figure 2.3(b)). For this problem, the normal stresses inside the contact zone and the normal stresses and the displacements outside the contact zone were sought. In the second contact problem, adhesive traction was prescribed outside the contact zone (Figure 2.3(c)) and the expressions for the normal stresses inside and the displacements outside the contact zone were derived. The second problem is similar to the external circular crack problems in fracture mechanics.[45]

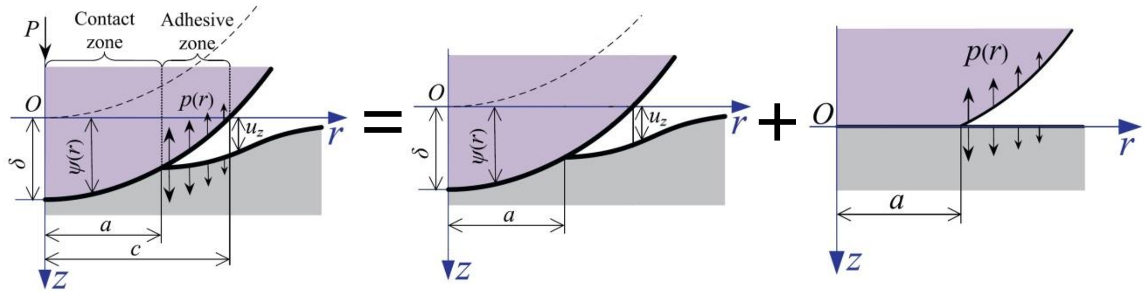

(a) (b) (c)

Figure 2.3: Schematic illustration of (a) an adhesive contact problem, (b) a contact problem with displacement prescribed within the contact zone, and (c) a contact problem with adhesive traction prescribed outside the contact. The punch is assumed to be rigid and the half space is elastic. This picture is taken from Zhou *et al*.[45]

The general solution of an adhesive contact problem with an axisymmetric arbitrary punch shape by Zhou *et al.* is summarized in the following equations. The displacement components and the radial and tangential stress components at the contact are not presented here as they are not used in this thesis.

$$\delta = \int_0^a \frac{af'(t)}{\sqrt{a^2-t^2}}\,dt + \frac{1-\nu}{\mu}\int_a^\infty \frac{tp(t)}{\sqrt{t^2-a^2}}\,dt \quad , \tag{2.6}$$

$$\sigma_{zz}\big|_{z=0} = -\frac{2\mu}{\pi(1-\nu)}\int_r^a \int_0^x \frac{[tf'(t)]'}{\sqrt{(x^2-t^2)(x^2-r^2)}}\,dt\,dx - \frac{2}{\pi}\int_a^\infty \frac{tp(t)}{t^2-r^2}\sqrt{\frac{a^2-r^2}{t^2-a^2}}\,dt, \quad r < a \quad , \tag{2.7}$$

$$P = 4a\int_a^\infty \frac{tp(t)}{\sqrt{t^2-a^2}}\,dt + \frac{4\mu}{1-\nu}\int_0^a \frac{t^2 f'(t)}{\sqrt{a^2-t^2}}\,dt + 4\int_a^\infty tp(t)\cos^{-1}\frac{a}{t}\,dt \quad .$$

(2.8)

where δ is the rigid-body displacement, a is the contact radius, *f(t)* is the shape function of the axisymmetric punch, t is the integration variable representing the radial position, ν is the Poisson's ratio, μ is the shear modulus, *p(t)* is the adhesive interaction force function, σ_{zz} is the normal stress distribution, r is the radial position at the contact, χ is another integration parameter to represent radial position at the contact, and P is the applied normal load. To utilize these equations, the term *p(t)* is set to zero because of the fact that there is not a straightforward way to accurately determine the adhesive function for the AFM tips. Instead, the adhesion force is added to the peak repulsive force as is done for the Hertz model to lead to the results for the DMT model. Although here we are applying this concept to the arbitrary tip profiles which are not necessarily paraboloidal, it is the most straightforward approach currently available. By setting *p(t)* to zero Eqs. (2.6) to (2.8) will be reduced to the following equations. Using these equations, one can easily derive the Hertzian solution by replacing *f(r)* with the equation of a parabola, $f\left(r\right)=\frac{r^2}{2R}$.

$$\delta = \int_0^a \frac{af'(t)}{\sqrt{a^2-t^2}}\,dt \quad ,$$

(2.9)

$$\sigma_{zz}\big|_{z=0} = -\frac{2\mu}{\pi(1-\nu)}\int_r^a \int_0^x \frac{[tf'(t)]'}{\sqrt{(x^2-t^2)(x^2-r^2)}}\,dt\,dx, \quad r < a \tag{2.10}$$

,

$$P = \frac{4\mu}{1-\nu}\int_0^a \frac{t^2 f'(t)}{\sqrt{a^2-t^2}}\,dt \tag{2.11}$$

.

To apply this solution to the more complicated AFM tip shapes, one needs to determine the correct orientation of the AFM tip's profile with respect to the sample, and the approximate region in the profile that makes the initial contact with the sample. Also, the AFM tip profiles are not necessarily axisymmetric imposing another challenge in the application of Zhou *et al.* solution to AFM tips. These issues and how to address them are described in section 3.5.

2.4: Mapping Stress and Selection of AM-AFM probe and Free Oscillation Amplitude

The advantage of minimizing the sample-tip interaction in AM-AFM compared to contact mode AFM can be lost if one selects experimental settings (*i.e.* free oscillation amplitude, A_0 and amplitude ratio, A_{ratio}) that result in the contact stresses beyond the tip/sample material's yield/failure stress. This can readily happen as an AM-AFM user may not have a clear understanding of the complex mechanics and dynamics of the nonlinear tip-sample interactions, and consequently may fail to appropriately control the experimental parameters to ensure that contact stresses are sufficiently low to prevent failure.

In this section, we simplify Eqs. (2.1) to (2.5) for two objectives. First, with a simpler closed-form equation, one will be able to then more easily choose free oscillation amplitude, which is the most critical parameter controlling tip/sample wear and permanent deformation. Second, this simplification will be used to plot stress maps. These maps will be used to reveal the achievable range of contact stresses for a particular tip and sample, guiding one in choosing the appropriate probe for a particular AM-AFM experiment.

2.4.1: Peak Repulsive Force: Assumptions and Dependence on Amplitude Ratio

An AM-AFM experiment involves two distinctive steps: approaching the sample, and then scanning it. We briefly discuss approaching the tip to the sample as this imposes a constraint to the calculation of the maximum possible normal contact stress. Before approaching the sample, the primary flexural resonance frequency of the cantilever is determined. The cantilever is then excited at a fixed drive frequency at or near this measured resonance frequency. Subsequently, the sample is brought closer to the tip, either through moving the sample up or the probe chip down. As the approach continues, the oscillation amplitude decreases as a consequence of a shift in resonance frequency and increased damping. Both the shift in the cantilever resonant frequency and increased damping result from the tip-sample interaction. This reduction continues until the oscillation amplitude reaches a predetermined value, usually referred to as the set-point amplitude/tapping amplitude, defined by the user.

If one plots the peak repulsive force as a function of the amplitude ratio using Eq. (2.1), it can be seen that as the tip approaches the sample and consequently the amplitude ratio decreases, the peak repulsive force increases until it reaches a maximum value. If the approach continues beyond this point, the tip-sample repulsive force is reduced, despite a common misconception among users who generalize that a further reduction in oscillation amplitude suggests increased repulsive forces (Figure 2.4). An intuitive physical explanation for this can be found by examining the impact velocity of the tip. Right before the beginning of the tip-sample interaction, the impact velocity is zero as it is where the tip stops moving down and begins going upward in an oscillation cycle. As the tip gets closer to the sample, it begins interacting with the sample with a nonzero velocity. In other words, the impact velocity will not be zero anymore. Now, if the approach continues until tip snaps into the sample which corresponds to the amplitude ratio approaching zero, the impact velocity becomes zero again as there will be no impact anymore. This suggests that the impact velocity is increased to a maximum value somewhere in between these two initial and final situations and is decreased afterward. Su *et al.*[34] attempted to analytically calculate the impact velocity as a function of the amplitude ratio. They observed the same behavior as described here. Now, if one approximates the tip sample force as a rate of momentum exchange between the tip and sample, the peak repulsive force should follow the same trend as the impact velocity. The approximate amplitude ratio, where the peak repulsive force reaches its maximum value, is an important parameter to take into account in the following calculations to estimate the maximum possible contact stress.

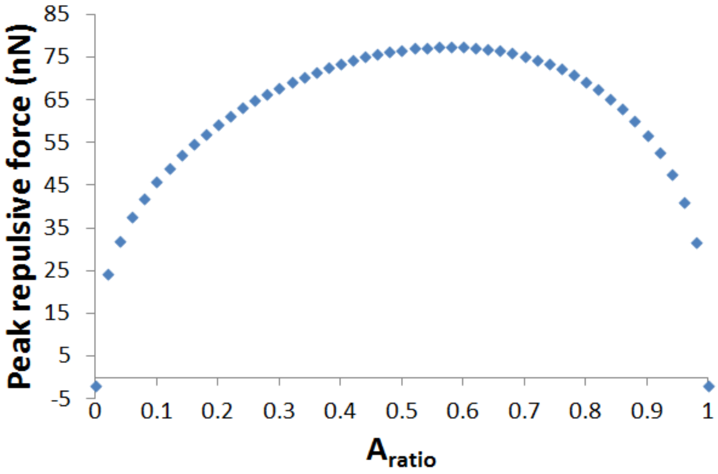

Figure 2.4: Peak repulsive force as a function of amplitude ratio for a cantilever with a spring constant of 42 N/m, quality factor of 480, tip radius of 20 nm, reduced Young’s modulus of 136 GPa corresponding to a diamond-like carbon-coated tip and a UNCD sample, and free oscillation amplitude of 23 nm.

Before proceeding to the next section, the following important assumptions used in the subsequent analytical expressions will be listed. First, we assume that the tip-sample contact is either Hertzian or DMT-like. Therefore, if the contact cannot be described by the Hertz or DMT contact mechanics model, the results here will not be accurate and one should seek other means such as VEDA to calculate relevant forces.

Another important assumption is the absence of any capillary formation between the sample and tip. Capillary formation alters the value of the peak repulsive force from what is calculated here. There are multiple studies discussing the effect of capillary formation in AM-AFM that can be used to account for the additional stresses caused by the formation of a capillary. Through friction force microscopy, it has been shown that the time required for capillary meniscus nucleation between the sample and tip at 40% relative humidity (RH) is on the order of few milliseconds.[46] However, in typical AM-AFM experiments, the contact time is on the order of a few microseconds; in the experiments performed in this thesis, contact time ranges from 0.1 to 0.2 μs. Because of the short contact times and the strong dependence of water condensation on RH,[47] Sahagún *et al.*[48] concluded that in AM-AFM, capillary bridges only form when the RH exceeds 50%.

In another study, Zitzler *et al.*[49] did not observe any significant change in the transition from attractive to repulsive regime across a wide range of RH, from 3 to 96%, where operating AM-AFM on a hydrophobic sample. This finding implies that, in the case of hydrophobic samples, capillary formation does not influence AM-AFM operation. However, Zitzler *et al.* observed a moderate change in the transition from attractive to repulsive regime between 30 to 70% RH and significant change above ~70% RH where the tip and sample were both hydrophilic. To summarize the conclusions of these two studies, capillary forces can be ignored when determining tip-sample forces if the RH is below 40% or the sample is hydrophobic. In other cases that capillary formation is significant one must use the VEDA to include capillary formation in the calculation of peak repulsive force. All the experiments in this thesis are performed in a mixture of humid air and dry nitrogen with 15% RH. Just one experiment is performed in 40%RH to consider the effect of humidity on the wear rate of diamond-like carbon (DLC).

Therefore, the capillary forces are not accounted in the estimation of forces and stresses in this thesis. Under these assumptions, we consider the Hertzian and DMT-like contacts separately in the following sections.

2.4.2: Hertzian Contact

2.4.2.1: Non-Dimensionalization of the Maximum Contact Stress

When one considers the contact to follow Hertzian behavior, the adhesion force is ignored. Therefore, we just use the first term of the Eq. (2.1) to calculate the peak repulsive force. In a Hertzian contact, the maximum normal stress is located at the center of contact and can be calculated through:

$$\sigma_{max} = \frac{3}{2\pi}\left(\frac{4E^*}{3R}\right)^{\frac{2}{3}} {F_{peak}^{rep}}^{\frac{1}{3}}, \tag{2.12}$$

Notice that Eq. (2.12) is different from Eq. (2.5), which gives the average stress in the contact, through an additional pre-factor of 3/2. By plugging in the Eq. (2.1) with $F_{adhesion} = 0$ into (2.12) and rearranging the parameters, we obtain:

$$\left(\frac{\sigma_{max}}{E^*}\right) \approx 0.723\left(A_0 A_{ratio} C_{cs}^{\frac{2}{3}}\right)^{\frac{3}{8}}\left\{\left(-1+\Omega^2\right)Q+\sqrt{\frac{1}{A_{ratio}^2}\left[\Omega^2+\left(1-\Omega^2\right)^2 Q^2\right]-\Omega^2}\right\}^{\frac{1}{4}} ,$$

where $$C_{cs} = \frac{k}{E^* Q R^{\frac{5}{2}}}$$

(2.13)

Eq. (2.13) is in non-dimensionalized format. We call C_{cs} the "cantilever-sample constant" which is a critical parameter to minimize tip/sample damage by choosing the correct cantilever properties and experimental settings for AM-AFM experiments. It should be mentioned that C_{cs} is not dimensionless, having units of $\mathrm{nm}^{\frac{-3}{2}}$ as k is N/m, E^* is in GPa, and R is in nm. Also, C_{cs} is primarily defined by the physical properties of the cantilever, although it includes some information regarding the sample material's Young's modulus and Poisson's ratio through E^*.

As mentioned previously, there is a particular A_{ratio} at which the peak repulsive force reaches its maximum value as the tip approaches the sample. This situation can be avoided by operating with larger A_{ratio} values; otherwise, if the cantilever is operated blow this critical A_{ratio}, which corresponds to smaller peak force, the tip still has to pass through this ratio during the approach. In other words, the tip will experience the highest peak force and maximum stress transiently during approach, and this can exceed the tip's failure stress. Therefore, one should consider the worst-case scenario, which is operating at this maximum peak force and contact stress. This further simplifies the above non-dimensionalized expression. From differentiating Eq. (2.1), the critical A_{ratio} is going to be equal to $\frac{1}{\sqrt{3}}$. By inserting this value into (2.13) and rearranging the equation, we can write:

$$A_0 \approx 4.109 C_{cs}^{\frac{-2}{3}} \left(\frac{\sigma_{max}}{E^*}\right)^{\frac{8}{3}} \left\{\left(-1+\Omega^2\right)Q+\sqrt{2\Omega^2+3\left(\Omega^2-1\right)^2 Q^2}\right\}^{\frac{-2}{3}} ,$$

(2.14)

And if we set Ω to 1 which applies when the drive frequency is equal to the resonance frequency, we have:

$$A_0 \approx 3.261 C_{cs}^{\frac{-2}{3}} \left(\frac{\sigma_{max}}{E^*}\right)^{\frac{8}{3}} .$$

(2.15)

Eqs. (2.14) or (2.15) can be used to quickly and accurately choose a free oscillation amplitude such that contact stresses are low enough to prevent tip/sample damage. To accomplish this, one would first choose the maximum contact stress so that it is lower than the yield/failure stress of either the tip or sample material, whichever is smaller. Second, the cantilever-sample constant, C_{cs}, must be calculated after determining the cantilever's resonance frequency, quality factor, spring constant, and tip radius through measuring these, or acquiring them from the manufacturer's specifications. The Young's modulus and Poisson's ratio of the material comprising sample and the tip are also required in the determination of the C_{cs}, as stated before. Given the difficulty of measuring the tip radius, much greater accuracy in determining the C_{cs} can be realized through a simple measurement of the cantilever's resonance curve and spring constant.

Considering the wide range of values for these parameters given by the manufacturers, the measured values for the cantilever resonance frequency and spring constant often deviate significantly from the manufacturer's specifications. The value of the tip radius is the most important among all the other parameters of C_{cs} as it has the strongest dependence ($R^{-5/2}$). As with the other specifications mentioned, the value of the tip radius provided by the manufacturer is not necessarily accurate. On the other hand, measuring the tip radius is very difficult and the instrumentation required to perform this measurement is not readily available to all users. Performing BTR, scanning electron microscopy (SEM), and TEM are the methods that can be used to estimate the tip radius.

2.4.2.2: Stress Map for Hertzian Contact in AM-AFM

It is useful to create a map that relates the maximum contact stress, free oscillation amplitude and C_{cs} using Eq. (2.15). Figure 2.5 shows the variation of the free oscillation amplitude A_0 with the maximum applied stress normalized by the reduced Young's modulus (σ_{max}/E^*) for various C_{cs} values. To create a map with reasonable ranges, a variety of commercially available AFM probes that can be operated in AM-AFM mode are considered. Based on the cantilever specifications provided by the manufacturer, one observes two extremes for the calculated C_{cs}: one extreme is dominated when tapping against a compliant sample, such as polystyrene, setting an upper bound on the cantilever constant; a second extreme occurs when tapping against a stiff sample, such as diamond, setting a lower bound. Based on these calculations, C_{cs} varies from 2.4×10^{-9} (corresponding to a probe from Advanced Diamond Technology, Inc. (ND-SSCRL) made of monolithic UNCD tapping against diamond) to $1.8\times10^{-2}\ \mathrm{nm}^{\frac{-3}{2}}$ (corresponding to a silicon probe coated with chromium-gold from MikroMasch (HI'RES-C15/Cr-Au) tapping against polystyrene). As can be seen, Figure 2.5 covers a wider range including values of the cantilever-sample constant ranging from 2×10^{-10} to $0.2\ \mathrm{nm}^{\frac{-3}{2}}$, beyond the values typical of commercially available probes, to demonstrate the stresses incurred at the extremes. The vertical axis, A_0, varies from 1 to 100 nm which is the most common range used in AM-AFM. In this map, the spring constant is in (N/m), the tip radius and free oscillation amplitude are in (nm), and the maximum normal contact stress and reduced Young's modulus are in (GPa).

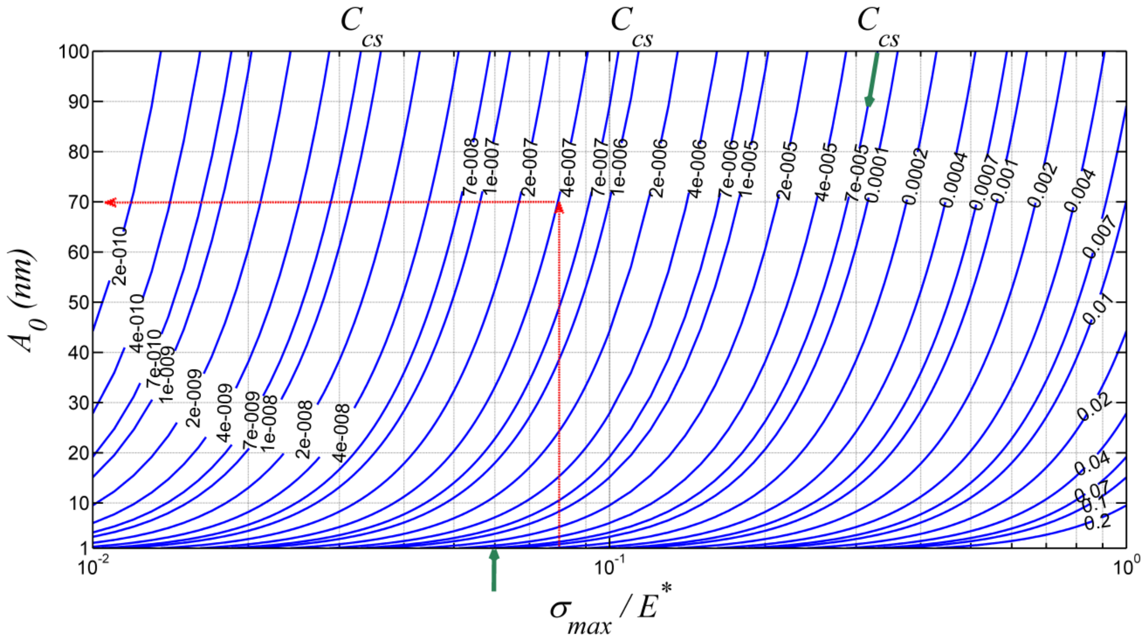

Figure 2.5: AM-AFM Hertzian contact stress map. The free oscillation amplitude is plotted against the maximum applied stress normalized by the reduced Young's modulus for a variety of cantilever-sample constants ranging from 2×10^{-10} to 0.2 $\text{nm}^{-\frac{3}{2}}$. A vertical red arrow denotes the normalized maximum applied stress that can be used when imaging a silicon sample with a diamond-like carbon-coated tip. The corresponding intersection point with the cantilever-sample constant curve ($C_{cs} = 4\times10^{-7}$ $\text{nm}^{-\frac{3}{2}}$) gives the maximum appropriate free oscillation amplitude permitted to avoid damaging the sample/tip during imaging. Green arrows indicate that the minimum achievable σ_{max}/E^* using a cantilever with $C_{cs} = 7 \times 10^{-5}$ $\text{nm}^{-\frac{3}{2}}$ with 1 nm free oscillation amplitude is 0.06.

For example, Figure 2.5 can be used to choose the optimal AM-AFM experimental parameters when imaging a silicon sample with a diamond-like carbon-coated probe from MikroMasch (HQ:NSC15/HARD). First, given that the yield strength of silicon (7 GPa[50]) is lower than diamond-like carbon (15-30 GPa[51]), the maximum stress, σ_{max}, should be chosen to be less than 7 GPa to avoid any damage or deformation to the sample features. Although the yield strength of silicon is well defined, the yield strength of diamond-like carbon (DLC) varies significantly depending on the deposition technique and composition. Gan *et al.*[51] reported a yield strength of 15 to 30 GPa for a DLC thin film deposited by filtered cathodic vacuum arc. The reduced Young's modulus of DLC against silicon (assuming E_{si} = 130 GPa, υ_{si} = 0.28, E_{DLC} = 150 GPa,[52] and υ_{DLC} = 0.3[53]) is calculated to be 76 GPa. Choosing $\frac{\sigma_{max}}{E^*} = 0.08$ results in a σ_{max} = 6.1 GPa, which is less than the silicon yield strength and is safe to preserve the sample features. The vertical arrow (red-dashed line) in Figure 2.5 corresponds to $\frac{\sigma_{max}}{E^*} = 0.08$. The cantilever-sample constant C_{cs} was then determined for the selected probe, which corresponds to approximately $4\times10^{-7}\,\text{nm}^{\frac{-3}{2}}$. Given these two parameters, the free oscillation amplitude must be set equal to or less than 70 nm for imaging this particular sample with the selected tip. The horizontal arrow in Figure 2.5 indicates the location of the preferred amplitude.

From Figure 2.5, one can determine that any C_{cs}, which corresponds to a specific cantilever and sample is confined to a particular range of maximum contact stresses. This is because of the instrumental limitations in achieving very small amplitudes, typically less than 2 to 3 nm, which sets a lower bound to the achievable maximum contact stress. For example, if C_{cs} is approximately equal to $7\times10^{-5}\ \text{nm}^{\frac{-3}{2}}$, corresponding to a particular experiment where a MikroMasch's HI'RES-C19 silicon cantilever coated with chromium-gold is used in an AM-AFM experiment examining a silicon sample, the lower bound for $\frac{\sigma_{max}}{E^*}$ is approximately 0.06 if the free oscillation amplitude is chosen to be 1 nm (green arrows in Figure 2.5). This means the smallest possible σ_{max} is approximately 4.0 GPa. Given that gold is the outermost material on this particular cantilever, we will assume its material properties in determining the reduced Young's modulus and whether or not the tip gets damaged. The ultimate tensile strength of the gold thin film at room temperature varies from 0.7 to 1.45 GPa.[54] Even though unrealistically small free oscillation amplitude is chosen, the contact stresses are larger than the yield stress of the gold, resulting in tip wear. Now, if one chooses MikroMasch's HQ:NSC19 silicon cantilever with no coating, it yields a corresponding C_{cs} of $3.5\times10^{-7}\,\mathrm{nm}^{\frac{-3}{2}}$ and consequently the $\frac{\sigma_{max}}{E^*}$ is then calculated to be 0.016 if the free oscillation amplitude is set at 1 nm. This means that the minimum achievable σ_{max} will be approximately 1.1 GPa, well below the silicon yield strength and neither the tip nor the sample should be damaged. In fact using this cantilever to examine the silicon sample, one can safely increases the free oscillation amplitude to approximately 56 nm, which results in $\sigma_{max} \approx 5$ GPa, without damaging the tip or sample. Care should be taken here as all the calculations in this section are based on the assumption of Hertzian contact with no adhesion force. The adhesion force can significantly alter these results. The examples presented here are solely for the purpose of demonstrating how to utilize Eqs. (2.14) and

(2.15) and Eqs. (2.18) and (2.19), derived for the DMT-like contact in the following section, and the stress maps.

2.4.3: DMT-Like Contact

2.4.3.1: Non-Dimensionalization of the Maximum Contact Stress

The Hertzian approach discussed in the previous section does not include the effects of adhesion, which are often significant in nanoscale contacts. This section applies DMT contact mechanics to the calculations of the peak repulsive force and maximum contact normal stress, thus including the effects of adhesive interactions in the limit of stiff, small-radii materials interacting via weak, long range forces. Therefore, the second term of the Eq. (2.1) is not eliminated as it was in the case of the Hertzian contact. Furthermore, the adhesion force is added to Eq. (2.12) in the subsequent calculations. The maximum contact stress then becomes:

$$\sigma_{max} = \frac{3}{2\pi}\left(\frac{4E^*}{3R}\right)^{\frac{2}{3}}\left(F_{peak}^{rep} - F_{adhesion}\right)^{\frac{1}{3}}, \tag{2.16}$$

By plugging in the Eq. (2.1) into (2.16) and rearranging the parameters, we can write:

$$H \approx 0.378\left(A_0 A_{ratio} C_{cs}^{\frac{2}{3}}\right)^{\frac{9}{8}} \left\{\left(-1+\Omega^2\right)Q + \sqrt{\frac{1}{A_{ratio}^2}\left[\Omega^2 + \left(1-\Omega^2\right)^2 Q^2\right] - \Omega^2}\right\}^{\frac{3}{4}},$$

$$\text{where} \qquad H = \left(\frac{\sigma_{max}}{E^*}\right)^3 - 1.824\left(\frac{w}{E^* R}\right)$$

(2.17)

Again, as with Eq. (2.13), Eq. (2.17) is put in a non-dimensionalized format. Similar to the Hertzian contact model discussed earlier, the maximum possible contact stress encountered during an AM-AFM experiment need to be considered. This situation occurs when $A_{ratio} \approx 1/\sqrt{3}$. At this point, this amplitude ratio can be used to simplify and rearrange Eq. (2.17), so that we can write:

$$A_0 \approx 4.109 C_{cs}^{\frac{-2}{3}} H^{\frac{8}{9}} \left\{\left(-1+\Omega^2\right)Q + \sqrt{2\Omega^2 + 3\left(\Omega^2-1\right)^2 Q^2}\right\}^{\frac{-2}{3}},$$

(2.18)

If we set Ω to 1, which applies when the drive frequency is equal to the resonance frequency, we have:

$$A_0 \approx 3.261 C_{cs}^{\frac{-2}{3}} H^{\frac{8}{9}}.$$

(2.19)

It is interesting to notice that Eqs. (2.18) and (2.19) are quite similar, including their respective pre-factors, to Eqs. (2.14) and (2.15) in the case of the Hertzian contact.

The only difference is the replacement of $\frac{\sigma_{max}}{E^{*}}$ in Eqs. (2.14) and (2.15) with $H^{\frac{1}{3}}$ in Eqs. (2.18) and (2.19) which includes the tip-sample work of adhesion. Again, Eqs. (2.18) or (2.19) can be used to quickly and accurately choose a free oscillation amplitude such that tip/sample damage is prevented. Similar to the procedure described before, the first step is to choose a maximum contact stress that is lower than the yield/failure stress of the tip or sample material, whichever is smaller. Second, the tip-sample work of adhesion should be measured through pull-off force measurements as described in sections 3.2.1 and 4.1. It is then possible to determine the dimensionless parameter H, by combining the desired maximum contact stress, tip-sample reduced Young's modulus, and work of adhesion. Finally, the cantilever-sample constant, C_{cs}, should be calculated as before to be plugged into the Eqs. (2.18) or (2.19).

2.4.3.2: Stress Map for DMT Contact in AM-AFM

Similar to Figure 2.5 in the case of Hertzian contact, Figure 2.6 shows the map that can be constructed to relate the H value, free oscillation amplitude and cantilever-sample constant using Eq. (2.19). The same range for C_{cs} (values ranging from 2×10^{-10} to 0.2 $\text{nm}^{\frac{-3}{2}}$) is displayed on Figure 2.6, as was done in Figure 2.5. The range of C_{cs} corresponds to 6 orders of magnitude variation in H. The vertical axis, A_0, varies from 1 to 100 nm, typical of most AM-AFM measurements. The spring constant is in (N/m), the tip radius and free oscillation amplitude are in (nm), the maximum normal contact stress and reduced Young's modulus are in (GPa), and work of adhesion is in (J/m^2).

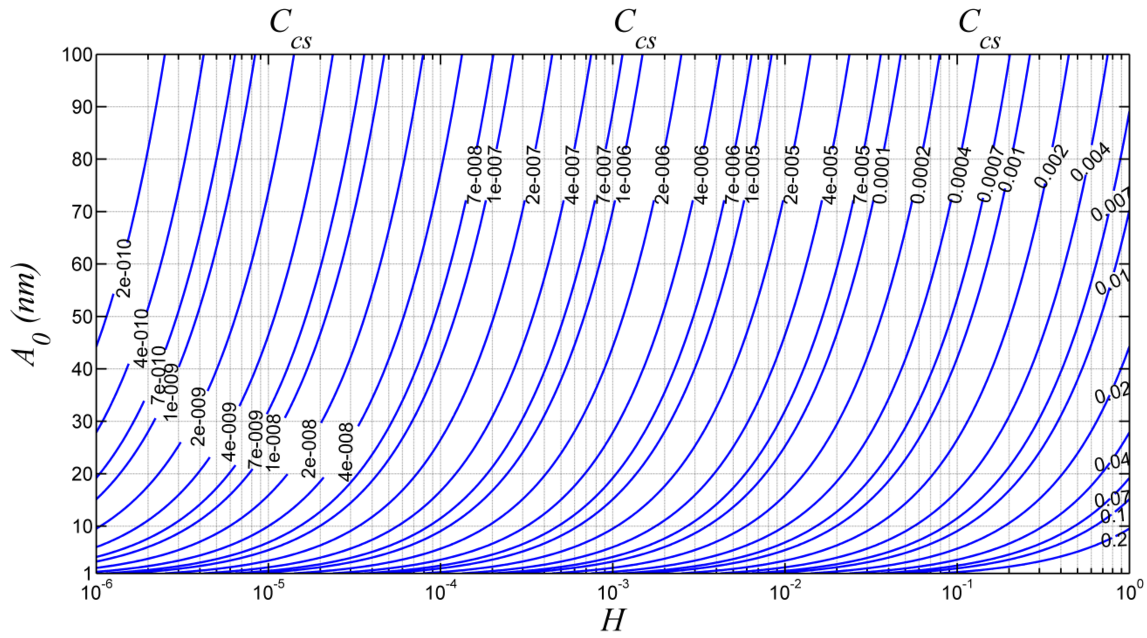

Figure 2.6: AM-AFM DMT-like contact stress map. The free oscillation amplitude is plotted against the dimensionless parameter *H* for a variety of cantilever-sample constants ranging from 2×10^{-10} to 0.2 $\text{nm}^{\frac{-3}{2}}$. The map can be used to choose appropriate cantilever and free oscillation amplitude in a particular AM-AFM experiment to avoid tip/sample damage or plastic deformation.

Applying Figure 2.6 to selecting the appropriate cantilever and free oscillation amplitude can be performed in a similar way as described in Section 2.4.2.2. Also, similar observations made from Figure 2.5 on the minimum achievable σ_{max} can be made here. Although Hertzian contact can be safely used for selection of an appropriate cantilever and free oscillation amplitude if one chooses the maximum contact stress conservatively such that it is well below the yield/fracture strength of the tip/sample, it is recommended to use the DMT-like approach as adhesion can have considerable impact on the tip-sample forces and stresses.

In summary, in this chapter we discussed the mechanics of tip-sample interaction in AM-AFM. The available techniques and equations to calculated peak repulsive force and contact stress are introduced. The analytical equations applicable for Hertzian and DMT-like contacts are used to make stress maps. These maps can be used to easily determine the experimental parameters necessary in AM-AFM to prevent tip/sample wear.

Chapter 3 : Experimental Methods to Study Wear in AM-AFM

Understanding the physics of wear and developing an accurate model to describe and understand this phenomenon in AM-AFM requires an experimental methodology that reveals and quantifies the influence of different factors in this process. For example, the effects of different tip and sample materials on wear are of interest. How the scanning parameters like free oscillation amplitude and amplitude ratio change the wear rate are also important to examine. It is also critical to observe the wear progress closely and progressively. In this section, the wear experimental methods and data analysis and quantification to achieve these goals are described.

3.1: HR-TEM and Blind Tip Reconstruction

As the change in tip geometry is the primary result of tip wear, tracking the evolution of the tip geometry during scanning is crucial. As mentioned previously, the shapes of the AFM tips are generally not simple paraboloids or spherical shapes; therefore, accurate determination of the shape and, if paraboloidal, the effective tip radius to be used for force and stress calculations is not straightforward.

There are several ways to measure the tip geometry, including HR-TEM, SEM, and reverse imaging or BTR. Unfortunately, HR-TEM and SEM are somewhat time-consuming, and depending on conditions and the tip material, prolonged exposure to the electron beam can contaminate the probe being imaged.[55] Here, HR-TEM is used as it captures high-resolution images of the tip apex that exceed what is attainable by SEM, and the HR-TEM profiles can be used to estimate the worn volume and the radius of the tip. Furthermore, care is taken to avoid long exposure times to the electron beam, such that no TEM-induced contamination or other alteration of the tip is observed.

One limitation of this method is that it only provides a two-dimensional profile of the tip since the tip is viewed in the plane transverse to the electron beam. Furthermore, the TEM can only access the plane that is parallel to the axes of the cantilever and the tip (the *y*-direction in Figure 3.1). A profile along the *x*-direction cannot be obtained since the TEM's electron beam is blocked by the cantilever carrier chip.

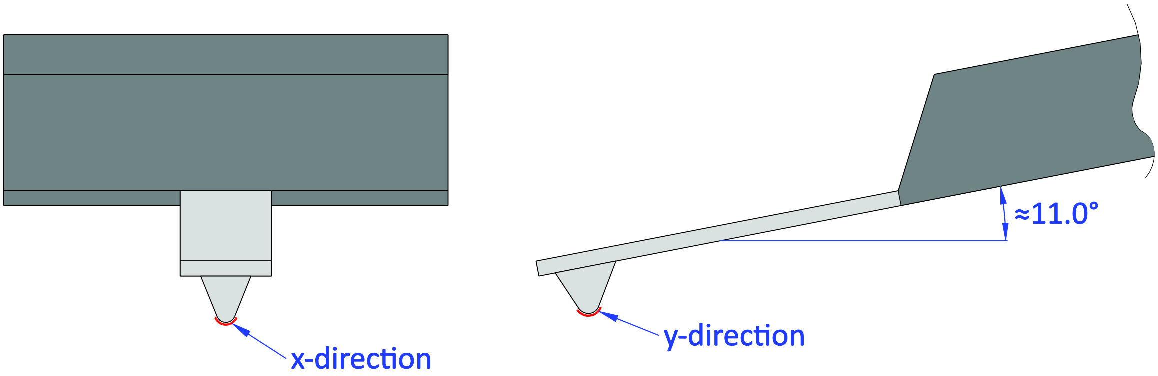

Figure 3.1: AFM probe tip *x*- and *y*-direction profiles. HR-TEM imaging is only able to capture the *y*-direction profile.

An alternate method to determine tip shapes, which is convenient and rapid but indirect, is to perform BTR using a sample with small, random, and durable sharp features, such as the Nioprobe® or TipCheck® (Aurora NanoDevices Inc.) commercial samples or UNCD, which has fine random features on its surface. The BTR method relies on the fact that an AFM topography image is a convolution of the tip geometry and the surface features. As a result of the finite size of an AFM tip, topographic images do not directly reflect the actual sizes of the sample features, and thus an AFM topographic image contains information regarding the shape of the tip. Image processing, performed here with the commercial software package Scanning Probe Image Processor (SPIP, Image Metrology A/S), can generate a reconstructed image of the tip that was used to obtain the topography image. From this reconstruction, the shape and approximate radius of the tip can be determined in two directions, which correspond to the x- and y-directions of the topography image. The x-direction tip profile determined by BTR gives information about the tip that is not accessible by HR-TEM. Strictly speaking, the tip shape provided corresponds to the largest possible tip that could have generated the recorded image data, and thus represents an upper bound on the tip shape. However, good quantitative agreement between BTR and HR-TEM images has been demonstrated.[13,14] The primary disadvantage of BTR is that it only provides information of the tip geometry over a region that is a few nanometers from the tip's apex. Therefore, to determine the tip-sample interacting geometry, both HR-TEM imaging and BTR are used, as described below.

As BTR provides information about the portion of the tip that interacts directly with the sample, its *y*-direction profile can be aligned with the HR-TEM image profile to identify the tip apex. However, the HR-TEM image must be rotated as the cantilever carrier chip is mounted in the AFM instrument at an angle, (*e.g.*, 11° in several instruments including the one used in this thesis), with respect to the sample (Figure 3.1).

This way, one can determine what specific portion of the tip apex is interacting with the sample during imaging (Figure 3.2). A circle or parabola can then be fit to the appropriate portion of the tip to determine the effective tip radius of that region. In this work, several reasonable circles and parabolas are fit to account for subjectivity in measurement, and an average radius of these fits is used. This fitting provides the radius of the tip in the direction parallel to the long axis of the cantilever, denoted here as R_y. BTR can be also used to estimate the tip radius in the direction perpendicular to the long axis of the cantilever, denoted here as R_x. However, the accuracy of the tip radius determined by BTR depends on the amount of noise in the height image. Therefore, to estimate R_x, we obtain an image where the fast scan direction is chosen to be perpendicular to the long axis of the cantilever (*i.e.*, along the *x*-direction), since the tip radius acquired along the fast scan direction is more reliable as it is acquired more quickly, and is thus subject to less noise and drift than the slow scan direction.

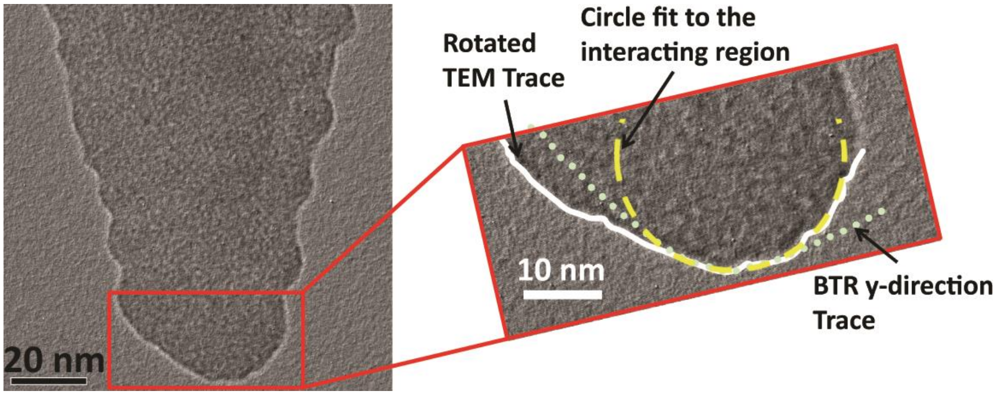

Figure 3.2: Determination of the effective tip radius (along the *y*-direction profile, $R = R_y$) by combining HR-TEM and BTR.

3.2: Wear Experiment Protocol

To perform consistent and comparable wear tests on different tip materials, all experiments need to follow a common protocol. For this study, the experimental protocol was developed by adapting a previous contact mode wear test protocol[14] to AM-AFM wear testing. The protocol involves performing pull-off force measurements using a comparable AFM probe to estimate the work of adhesion for the probe tip of interest, controlling the tip-sample attractive/repulsive force regime, calculating maximum contact forces and normal stresses, and quantifying the wear volume using HR-TEM imaging. Figure 3.3 summarizes the overall AM-AFM wear protocol.

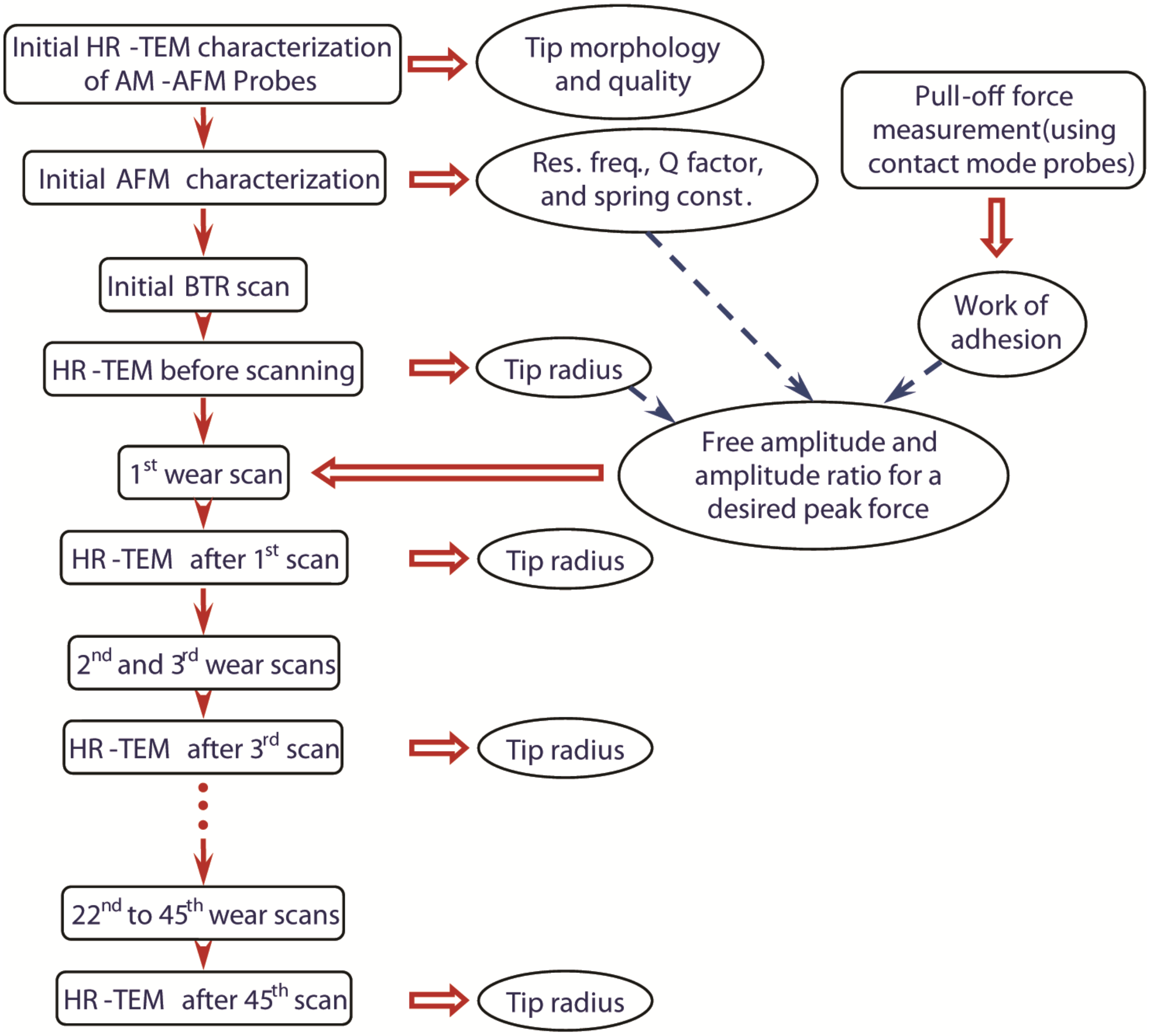

Figure 3.3: Flow chart illustrating the wear experiment protocol.

3.2.1: Pull-Off Force Measurements

As mentioned above, the work of adhesion is required to calculate peak repulsive force. If the work of adhesion between the tip and sample materials is unknown, pull-off force measurements can be performed using contact mode probes made out of the same materials as the AM-AFM probes. Preferably, contact mode probes from the same vendor, made of the same tip material, where the tip is formed using the same standard process, should be used to ensure that the tip morphology and chemical properties are as similar as possible for both the contact mode and AM-AFM probes.

Here, for each tip-sample material pair tested for wear in AM-AFM, three separate contact mode probes, all with identical specifications, from the same vendor as the AM-AFM probes and composed of the same tip material, were used to measure the work of adhesion between that tip material and a UNCD sample. UNCD is chosen as the sample for the experiments performed in this thesis because it exhibits sharp, random features that can be used for BTR and is highly wear-resistant, leading to the tip wearing more than the sample. A total of 150 force-distance curves (5 different locations on the sample, with 30 force-distance curves taken at each location) were acquired from each probe in a mixture of humid air and nitrogen gas at 15% RH. The reported work of adhesion, calculated using the DMT contact model, is the average of 450 data points (3 probes with 150 force-distance curves each). As apparent from Eq. (2.2), to calculate work of adhesion one needs to measure the tip radius. Here, HR-TEM images of the contact mode probe tips are obtained to measure the tip geometry and to estimate the effective tip radius both before and after obtaining the force-distance curves. Tips whose geometries deviate substantially from paraboloidal shape are discarded, and measurements with a new probe are acquired. For suitable tips, an average of the tip radius before and after pull-off force measurements is used along with the average pull-off force. From this, using Eq. (2.2), a value of the work of adhesion between the specific tip material and UNCD is extracted.

This method assumes no significant change in the tip's surface chemistry during AM-AFM wear tests. In fact, tip chemistry could change if contamination or the native oxide layer is removed or modified. However, we assume that this is not an issue, since the experiments are performed in air, there likely is rapid re-contamination from ambient species and re-oxidation. Thus, based on these measurements using contact mode tips, a value for the work of adhesion to apply to the AM-AFM tips is obtained.

3.2.2: Determination of the Cantilever Physical Properties and Tip Shape

The next step in the protocol involves obtaining HR-TEM images of new, unused AM-AFM probes to determine the initial tip shape and morphology. Once again, tips with unusual shapes or observable contamination are discarded. Then, using the AFM, each cantilever's quality factor and resonance frequency are measured, and its normal force spring constant is determined using the Sader method.[56] The quality factor and resonance frequency are measured by both regular mechanical tuning and by thermal noise spectra using built-in features of the AFM systems. Values obtained from these two methods are theoretically the same[56] and are averaged to provide more reliable measurements. The inverse optical lever sensitivity (InvOLS) of the cantilever's normal deflection signal, which is the conversion factor between the amplitude expressed in volts to nanometers, is required in order to calibrate the amplitude. This is calculated by measuring the thermal noise spectrum of the first flexural mode, and fitting it with a Lorentzian function scaled so that it integrates to the thermal energy $k_BT/2$. This scaling is based on the equipartition theorem, which relates the cantilever's Brownian motion of the first flexural mode to its thermal energy.[57] As the spring constant is known through Sader method, the Lorentzian curve fit determines the InvOLS.

After characterizing the tips and the cantilevers, the probes were used to scan a UNCD sample (1×1 μm^2, 512×512 pixels, 1 Hz scan rate) to obtain a high-quality topography image that can be used for BTR; we call this the BTR scan. For the BTR scan, the imaging parameters are chosen to avoid any significant tip wear: the free oscillation amplitude is kept small (on the order of few nanometers), and the amplitude ratio is set as close to 1 as possible while still tracking the topography of the sample. The tip profile extracted from the initial HR-TEM image is compared to that obtained from the BTR scan to determine an initial effective tip radius as described in section 3.1 (Figure 3.2). The same procedure for determining the tip radius is applied over the course of the entire wear test, using topographic images acquired immediately before TEM imaging for blind tip reconstruction.

3.2.3: AM-AFM Scanning to Induce Wear

To establish and maintain the force regime (low amplitude/attractive *vs.* high amplitude/repulsive) in which the tip operates during scanning and to determine the peak repulsive force, the free oscillation amplitude and the amplitude ratio are selected and held constant throughout the duration of the wear test. In the present work, wear scans are performed in the high amplitude/repulsive regime. In the following section, the method for determining appropriate amplitude ratios for a given free oscillation amplitude to ensure imaging stability is explained. Once the initial measurements have been obtained and the wear-test parameters have been chosen, the wear testing begins. For our studies, a total of forty five 1×1 μm^2 images of a UNCD sample are acquired. All the experiments used for examining wear models are performed in 15% RH. Two consecutive extra sets of 12 scans in less than 5% RH and in 40% RH are performed on two of the DLC-coated tips with some DLC coating left after the 45 wear scans to investigate the effect of moisture on the wear rate. HR-TEM images of the tips were acquired after 1, 3, 9, 21, and 45 scans of all the tips and also after 57 and 69 scans of the two tips studied in different relative humidity. The HR-TEM images, along with BTR analysis of the topographic images, provide information about the evolution of the tip shape and radius throughout the wear test, and are used to calculate peak repulsive forces and average normal stresses.

3.3: Controlling and Maintaining Force Regime

As mentioned before, an AM-AFM experiment can be performed in two different force regimes: attractive/low amplitude, or soft tapping, in which attractive forces are dominant; and repulsive/high amplitude, or hard tapping, in which repulsive forces are dominant. Depending on the free oscillation amplitude, tip/sample material properties, and cantilever properties, the tip and sample interaction could be entirely in the attractive or repulsive force regime.

The force regime plays an important role in the wear of AM-AFM probes as the tip-sample interaction forces and dissipated energy will vary depending on the force regime.[29,58] The parameters used for maintaining and controlling the force regime could differ depending on the particular tip and sample materials, cantilever properties, tip morphology, and experimental set up. Usually, higher amplitude ratios (*i.e.*, tapping amplitude close to free amplitude) result in attractive regime operation, while low amplitude ratios will lead to repulsive regime operation. For given tip and sample materials, cantilever properties, and free amplitude, there will be a range of amplitude ratios within which transitions between the two force regimes can occur. This is the so-called “bi-stable regime” (Figure 1.4).[30] The range can be found by obtaining amplitude and phase *vs.* *z*-position plots using a sacrificial probe of the same type (and nominally of the same tip size and surface chemistry) as that which will be used in the experiment. Upon approaching the surface, a transition from the attractive to repulsive regime will be observed; the reverse transition will occur upon retracting from the surface. Working significantly below or above this transition range ensures imaging stability by avoiding the bi-stable regime. The most straightforward way to determine the force regime while scanning the sample is by examining the phase shift. The phase shift between the excitation signal and the cantilever response in AM-AFM is routinely obtained simultaneously with the topography. Typically, an average phase angle between 0° and -90° (-90° and -180°) is an indication that the system is operating in the repulsive (attractive) regime. Care should be taken as the raw phase angle may not be reported in certain commercial AFM instruments; some systems offset the phase by 90° or change the sign, for example.

3.4: Wear Volume Calculation

As an example of the wear volume calculation, Figure 3.4(a) shows overlaid profiles of a DLC-coated silicon tip used in our experiments. The profiles are obtained from HR-TEM images acquired before scanning and after 1, 3, 9, 21, and 45 scans. A custom MATLAB script is used to trace the edges of the tip boundaries. The 2D profiles are used to approximate the volume of material that has been worn and/or plastically displaced by integrating over the tip profile up to a certain height of the tip shank using the method of disks.[14] This integration approach assumes that the tips are circularly symmetric at each height increment. However, the application of this procedure to the SiN_x-coated tips (another type of tips used here) that exhibit plastic deformation and bulging (flow of the tip material to the sides, as will be presented in section 4.2) requires careful selection of the integration height. As demonstrated in Figure 3.4(b), the integration height should be just above the worn or plastically deformed region. This is because the plastic deformation is not necessarily produced evenly on the periphery of the tip. Therefore, if one includes the displaced material in the integration using method of disks, which assumes axisymmetry at any given height, a large error can be introduced to the wear volume calculation.

Also, before determining the integration height, it may be necessary to rotate the overlaid profiles to take advantage of any symmetry of the worn region, as shown in Figure 3.4(c). This rotation is different from the rotation that will be described in the following section which helps to determine the initial point of contact of the actual tip profile. Rather, the rotation described here is solely to simplify the integration of the displaced material around the tip apex.

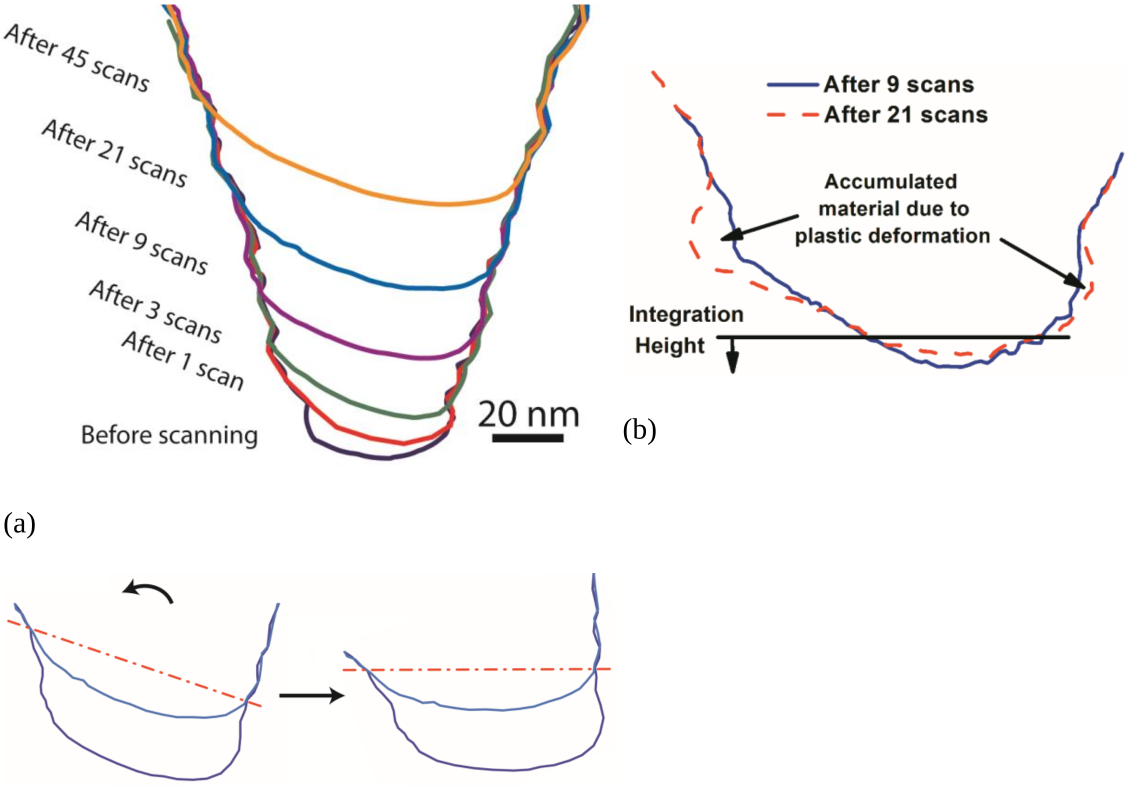

(b)

(a)

(c)

Figure 3.4: (a) Overlaid HR-TEM profiles of a DLC-coated tip before AM-AFM scanning, and after completing 1, 3, 9, 21, and 45 scans. (b) Overlaid HR-TEM profiles of a SiN_x-coated tip after 9 and 21 scans, showing the height chosen for estimating removed material. (c) Overlaid HR-TEM profiles of the same DLC-coated tip after 9 and 21 scans, before and after being rotated by 16° so that they are oriented with respect to the horizontal as they are in the AFM. The 16° rotation is particular to these two profiles. The angle for other profiles could be different. The rotated profiles are used for the stress calculations.

3.5: Axisymmetric Arbitrary Punch Shape Solution Applied to the Arbitrary AFM Tip Shapes

As mentioned before, there are two issues arising when it comes to applying the solution for an axisymmetric arbitrary punch to the actual profile of an AFM tip. First, it is important to determine the location in the profile estimated to be the region of initial contact with the sample, and thus the profile's correct orientation with respect to the sample. This is performed by examining the overlaid HR-TEM images (Figure 3.4(a)). It is apparent that the tip is not worn evenly about its axis of symmetry, as there is more wear towards the left side of the tip shank. This is more obvious in the case of the tip profiles of the two successive HR-TEM images in Figure 3.4(c). One source of this asymmetry is due to the fact that the probe chip is mounted in the AFM instrument at an angle, in this case for the Asylum MFP-3D AFM instrument, at 11˚, with respect to the sample (Figure 3.1). This mounting angle does not necessarily determine the true tip-sample orientation as the presence of any contamination between the chip and the chip holder, any slope in the cantilever with respect to the chip, or any slope in the sample's surface with respect to the AFM stage can alter the angle somewhat. Furthermore, the cantilever is tilted by an additional angle during AM-AFM operation when it is at the bottom of its oscillation cycle. For the cantilevers and AM-AFM parameters used in this study, this angle is estimated to be at most 0.02° corresponding to a DLC-coated tip with largest tapping amplitude of 25 nm. As it appears, this angle is negligible in compare to the AFM chip mounting angle.

Another possible mechanism to explain the asymmetric tip shape is plastic shearing of the Si beneath the coating. If this was the case, then the deformation of the coating and Si should be coupled. Figure 3.5(a) demonstrates the HR-TEM images of the two DLC-coated tips after 45 AM-AFM wear scans. To highlight the orientation of the worn region with respect to the Si, Figure 3.5(b) show the same images with black lines tracing the Si, red lines tracing the DLC coating, and the yellow lines showing the direction of the worn region and the tip axis. In the case of tip asymmetry as a result of the plastic deformation of the silicon substrate, the angle between yellow lines should be approximately 90° because the deformation would be coupled. However, the angle measured between the yellow lines is considerably deviated from 90°. Therefore, this deformation mechanism can be ruled out and it can be concluded that the wear of the DLC is anisotropic, and does not involve shearing of the Si substrate.

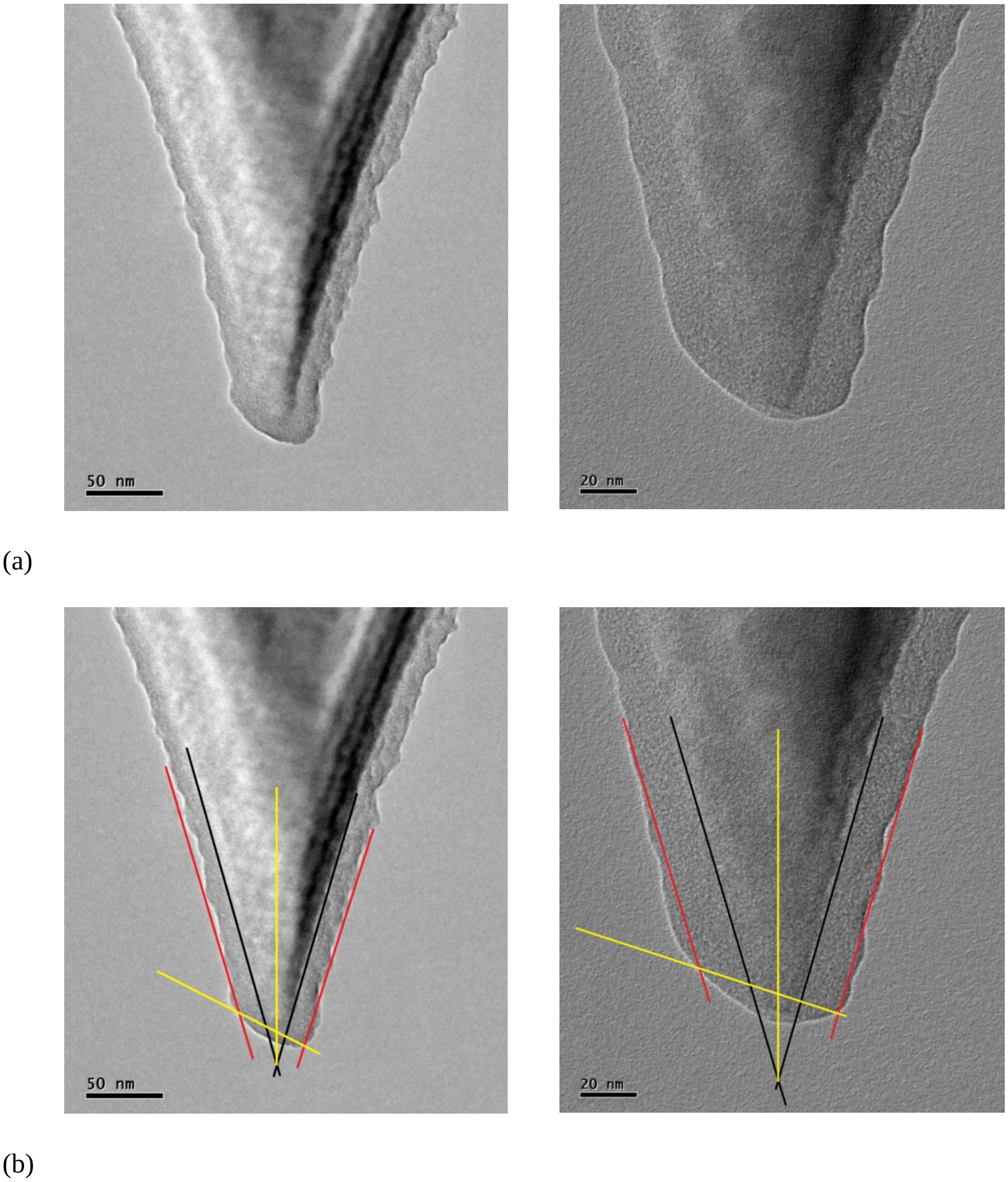

Figure 3.5: (a) HR-TEM images of the two DLC-coated tips after 45 AM-AFM wear scans and (b) the same images with black lines tracing the Si, red lines tracing the DLC coating, and the yellow lines showing the direction of the worn region and the tip axis. In the case of tip asymmetry as a result of plastic deformation of the silicon substrate, the angle between the yellow lines should be approximately 90° because the deformation would be coupled.

As the asymmetry of the worn region is mainly because of the tilt angle of the cantilever; therefore, rotating the tip profiles until the worn region is symmetric (Figure 3.4(c)) provides a better approximation of the tip profile orientation with respect to the sample. In the case shown in Figure 3.4(c), the orientation angle is determined to be 16º, which is particular to these two profiles. The angle for other profiles could be different, and in this study ranged from 8° to 22° including the total variation seen among all the tips. Consequently, the lowest point in the rotated initial tip profile is then assumed to be the point of initial contact.

Due to the tilt of the lever, one might argue that the slight relative lateral displacement (and consequent shear stress) between the tip and sample parallel to the sample can significantly contribute to the asymmetry of the worn region. A simple geometrical consideration of the worst-case scenario here, which is the case of the DLC-coated tip with largest tip-sample deformation (≈ 0.5 nm), reveals that the largest tip-sample relative motion is about 1 Å; less than the length of an atomic bond. Therefore, the resulting shear strain is insignificant.

Another challenge in applying the method of Zhou *et al.*[45] to the actual AFM tip profiles is that, even after performing this rotation, the tip apex's profile may not have mirror symmetry about the vertical axis. Figure 3.6(a) shows how the left side of a DLC-coated silicon tip apex is different from its right side. To address this, one can consider three different axisymmetric tip profiles (Figure 3.6(b)); one is constructed with the left side of the profile, the other one with the right side, and the third tip is the average of the left and right profiles. For this work, the average profile is used to calculate the average normal interfacial contact stress, which is calculated by dividing the total applied normal load, which is the peak repulsive force plus adhesion force, by the contact area. The stress values extracted from left and right profiles are used to calculate the range of uncertainty. A custom MATLAB script is used to perform these procedures and apply the solution of the axisymmetric arbitrary punch shape. The script can be found in the Appendix.

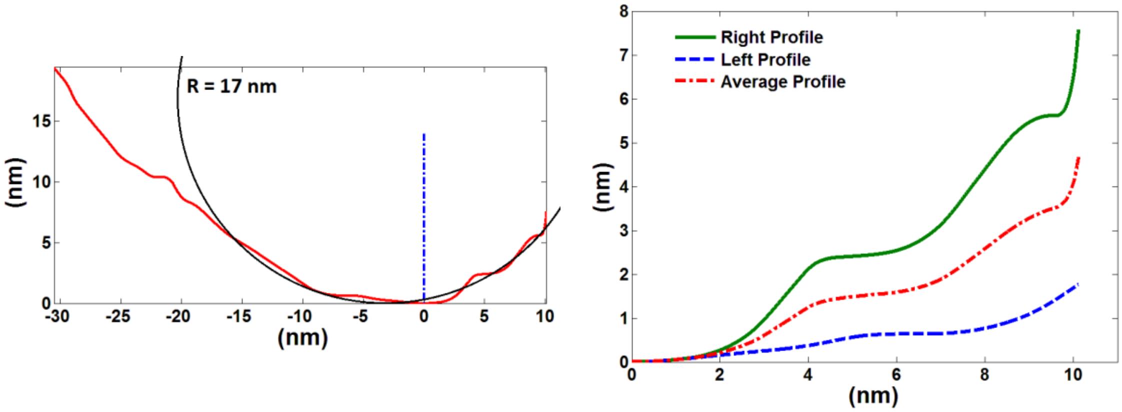

(a) (b)

Figure 3.6: (a) Profile of an AFM tip apex with a fitted circle, *R* = 17 nm. (b) Right profile, left profile (mirrored), and the average profile of the tip apex, used for constructing the three different axisymmetric tip shapes.

The normal stress distribution at the contact of these three profiles and a circle fit to the tip apex (Figure 3.6(a)) are plotted in Figure 3.7 for 10 and 100 nN applied normal loads. It is apparent that the stress distribution of the fitted circle is substantially different from that of the profiles determined from the actual geometry. For the case of the 10 nN applied load, the stress distribution of the left, right, and average profiles are similar due to the fact that the tip profiles are quite similar within the contact radius, which is less than 1 nm. However, these stress distributions begin to deviate from one another in the case of the 100 nN applied load because the tip profiles begin to be different as we move further in the radial direction. This justifies our selection of the average of the actual tip profile (with the left and right portions of the profile used for the uncertainty limits) in addition to fitting a circle or parabola for estimating the average normal contact stress.

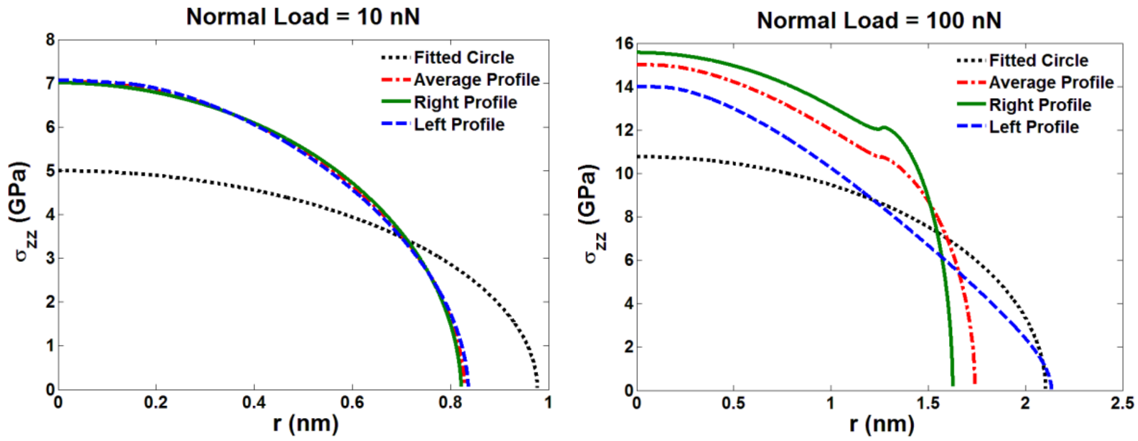

(a) (b)

Figure 3.7: Normal stress distribution at the contact of the left, right, and average profiles of the tip apex and the fitted circle in Figure 3.6 for (a) 10 and (b) 100 nN normal loads.

Chapter 4 : Wear of Silicon Nitride and Diamond-Like Carbon Coated Silicon Probes in AM-AFM

To improve the lifespan and reliability of AFM probe tips, materials with high wear resistance such as silicon nitride and DLC are often used to coat Si AFM tips. It should be mentioned that the wear of Si by itself are dominated by fracture events in typical AFM operations;[14] consequently, we decided to focus on wear-resistant coatings as they are more relevant and have better performance. To examine the applicability of the proposed wear protocol, three DLC-coated silicon probes (PPP_NCHR, Nanosensors; DLC thickness nominally 20 nm) and two silicon nitride-coated silicon probes (NSC15, MikroMasch, silicon nitride thickness nominally 10 nm) were tested. The counter surface was a UNCD[13–15] film deposited on a Si substrate (Aqua 25, from Advanced Diamond Technologies, Inc.). The 20 nm DLC coating (as measured by HR-TEM) was deposited on the silicon probes using the plasma immersion ion implantation and deposition process[52] by Dr. K. Sridharan (University of Wisconsin-Madison, Center for Plasma-Aided Manufacturing). The hydrogen content of the DLC film is about 41±2 at.%, and approximately 50 to 70% of the carbon structure is in the sp^3 state. Thus, this particular DLC is considered to be an amorphous hydrogenated carbon film (a-C:H).[59] Here, it should be mentioned that these experiments are not studying just the wear of DLC or SiN_x, but the wear of the film-substrate "system" that comprises the tip, since after all, it's the overall tip shape and size that matters.

The AM-AFM experiments are performed using the Asylum MFP-3D AFM at a fixed relative humidity of 15% in a mixture of dry N_2 gas and humid air. The AM-AFM parameters, which are listed in Table 1 along with the cantilever properties, are chosen to that the scanning occurs in the repulsive regime. The material properties used for calculating the Maugis parameter, the peak repulsive force, and the average normal stress are summarized in Table 2.

Table 1: Cantilever properties and experimental parameters used for wear experiments.

Cantilever	Spring Constant (N/m)	Resonance Frequency (kHz)	Free Oscillation Amplitude, A_0 (nm)	Amplitude Ratio, A_{ratio}
PPP_NCHR (Nanosensors), 20 nm DLC coating, Tip 1	43 ± 2	308.6 ± 0.1	50.0 ± 1.3	0.50 ± 0.03
PPP_NCHR (Nanosensors), 20 nm DLC coating, Tip 2	48 ± 2	318.3 ± 0.1	35.0 ± 1.0	0.40 ± 0.04
PPP_NCHR (Nanosensors), 20 nm DLC coating, Tip 3	42 ± 2	308.6 ± 0.1	23.0 ± 1.2	0.40 ± 0.07
NSC15 (MikroMasch), 10 nm SiN_x coating, Tip 1	44 ± 2	315.5 ± 0.1	35.0 ± 1.7	0.40 ± 0.04
NSC15 (MikroMasch), 10 nm SiN_x coating, Tip 2	50 ± 2	337.6 ± 0.1	23.0 ± 1.9	0.40 ± 0.04

Table 2: Material properties used in calculations of the contact properties. Silicon nitride material properties are the average of different values reported in literature.[60–63]

	Young's Modulus (GPa)	Poisson's Ratio
UNCD	790±30 [64]	0.057±0.038 [64]
DLC	150±30 [52]	0.3±0.05 [53]
SiN_x	230±50 [60–63]	0.23±0.05 [60–63]

As demonstrated later in this chapter (Figure 4.6 and Figure 4.12), to discuss the number of atoms removed due to wear, it is necessary to estimate the number of atoms per nm^3 of the measured worn volume. Calculating the number of atoms removed is also beneficial for making comparisons between the two different tips studied. Using the density and the atomic percentage of hydrogen, one can calculate the number of carbon and hydrogen atoms per nm^3 of DLC. The DLC coating is estimated to have 41±2 at.% hydrogen content and a density of 1.79±0.1 g/cm^3, based on secondary ion mass spectroscopy experiments and x-ray reflectivity measurements (Evans Analytical Group, Sunnyvale, CA) performed on DLC films deposited on flat substrates using the same deposition system and conditions as the films deposited on the tips. Using these measured values, it is estimated there to be 85±1 carbon atoms per nm^3, and 59±5 hydrogen atoms per nm^3 in our DLC. For silicon nitride, we use a literature value of 3.1±0.2 g/cm^3 for the silicon nitride density[65] and assume the equilibrium stoichiometry of Si_3N_4, resulting in an estimate of 40±3 silicon atoms and 53±4 nitrogen atoms per $nm^{3.}$

4.1: Estimation of the Work of Adhesion

Using the procedure described by Grierson *et al.*[44] as a first estimate of the work of adhesion, an upper bound to the work of adhesion is obtained by assuming that the JKR model applies; if Maugis' parameter is found to still be in the DMT regime despite this extreme value of the work of adhesion used, then the contact is safely in the DMT regime and corrected values for the work of adhesion can be determined. The JKR work of adhesion (calculated using $F_{adhesion} = -1.5\pi wR$) determined from pull-off force measurements is found to be 42±16 mJ/m^2 between the DLC tip and the UNCD sample, and 48±25 mJ/m^2 between the silicon nitride tip and UNCD. The reported error is based on the standard deviation of all the pull-off force measurements taken initially for a given tip, and propagating the error determined from the tip radius measurement. The substantial standard deviation comes from errors associated with estimation of the tip radius and the fact that the UNCD surface is rough and inhomogeneous. The inhomogeneity could be structural in origin as UNCD is composed of randomly oriented nanoscale grains composed of sp^3-bonded C atoms, and grain boundaries composed of a mixture of sp^2- and sp^3-bonded C atoms. It may also have a chemical origin, as the local chemical termination of the UNCD may involve hydrogen atoms, hydroxyl groups, or other species as affected by modest amounts of contamination that are inevitable upon exposing a sample to ambient conditions. Therefore, depending on where the AFM tip lands, the local surface energy and thus the pull-off force will vary. In addition, the variation may also arise from the tip and UNCD surface roughness, in which case the assumption of a paraboloidal tip interacting with a flat surface used for all the contact mechanics analysis in this study will introduce error.

To address this, we performed roughness analysis on the tip and sample surfaces within the scale of the tip-sample contact area. To assess the roughness of the UNCD sample, we analyzed high-resolution topographic AFM images that were 200×200 nm^2 in area with 2048 scanning lines and 2048 pixels per line (*i.e.*, every pixel is less than 1×1 $Å^2$ in size). We then corrected the image by reducing the effect of tip convolution using the tip deconvolution algorithm of the SPIP software. From this, we analyzed a series of 5 nm-long line profiles to extract the rms roughness of the sample. For each tip, as described before, we fit a parabola to the tip profile captured from TEM imaging and then subtracted that parabola from the actual tip profile over a 5 nm range centered at the tip's apex (*i.e.*, the region over which tip-sample contact is made). The roughness of the profile that resulted from the subtraction was then calculated to obtain a roughness value that would be equivalent to that of a flat surface. We chose the value of 5 nm based on the calculated contact diameters, which ranged from 1.3 to 4.3 nm according to our contact mechanics modeling; thus, 5 nm is a conservative upper bound to the possible contact diameter. The calculated rms roughness of the UNCD profiles ranged from below 0.3 nm (within the noise limit of the AFM) to a maximum of 0.9 nm, while the calculated rms roughness of the tips ranged from 0.2 to 0.5 nm. The true work of adhesion is going to be larger than what we extract from calculations assuming a parabolic tip and a flat sample. Thus, our values (calculated in the following paragraph) are lower bounds. However, this does not necessarily mean that the real adhesion force that the AFM tips feel is larger than what we estimated here from pull-off force measurements. The pull-off force measurements necessarily involve the tip and sample roughness, and whatever we measure in the force-distance curves is hypothesized to be an appropriate representation of what AFM probes experience in the subsequent AM-AFM mode measurement.

Tip and sample roughness are of concern, since we use the DMT model, which assumes perfectly smooth surfaces, to relate a pull-off force obtained with a slightly rough tip and sample to an effective work of adhesion (not the true work of adhesion); we then use that effective work of adhesion to estimate the pull-off force that other rough tips with different overall radii experience. If the roughness varies substantially between different tips, then this will introduce error.[66] The ideal approach would be to replace the DMT model with a model that takes into account the contacting bodies' roughness, and to precisely characterize the roughness of the tip at each stage. Unfortunately, no reliable method for that exists, and even if it did, it would require frequent measurement of the evolving tip roughness and the local sample roughness. At this time, such an undertaking is beyond the state-of-the-art for any practical AFM applications (the only report dealing with this issue required combining *in-situ* TEM measurements of contact with detailed atomistic simulations,[66] and still only allows two dimensional tip profiles to be considered, not full three dimensional tip structures). Given that the roughness of all of the tips varies within a reasonably narrow range, from 0.2 to 0.5 nm, the error introduced will not dramatically alter our conclusions.

As discussed before, to determine which contact mechanics model is most appropriate, the Maugis' parameter, λ, and the non-dimensional load, $\bar{P}$, should be calculated using Eqs. (2.3) and (2.4). For the DLC-coated probe, the average peak repulsive force is 90 nN, the average tip radius is 50 nm, and we choose z_0 = 0.3 nm, a reasonable value used for the equilibrium separation. Using Eqs. (2.3) and (2.4), λ is approximately 0.06 and $\bar{P}$ is found to be 14. For the silicon nitride-coated probes, the average peak repulsive force is 46 nN and the average tip radius is 27 nm. Likewise, λ is calculated to be approximately 0.05 and $\bar{P}$ is approximately 11. According to the adhesion map (Figure 5 of the Johnson and Greenwood paper[43]) the contact mechanics of both cases of DLC-coated and silicon nitride-coated probes against UNCD are best described by the DMT model. This holds despite using upper-level estimates for the work of adhesion (*i.e.*, the JKR equation provides lower-level values for $\bar{P}$ and higher-level values for λ, but the transition from the DMT to JKR limit strongly depends on the value of λ). Therefore, the work of adhesion values can now be correctly calculated using the DMT equation. From this, one finds the DMT work of adhesion based on measurements with contact mode tips for DLC-UNCD to be 31±12 mJ/m^2, and silicon nitride-UNCD to be 36±19 mJ/m^2. These values are then used for calculating the peak repulsive force and contact stress in subsequent wear experiments.

4.2: Silicon Nitride Coated Silicon Probes

The HR-TEM images of the silicon nitride coated probes before any AFM scanning and after completing 1, 3, 9, 21 and 45 scans (1×1 μm^2, 512×512 pixels, 2 Hz scan rate) are presented in Figure 4.1.

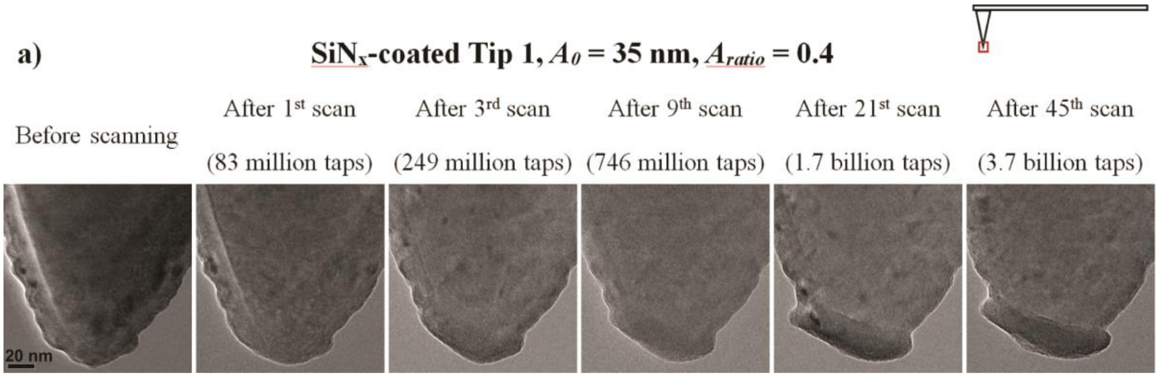

a) SiN_x-coated Tip 1, A_0 = 35 nm, A_{ratio} = 0.4

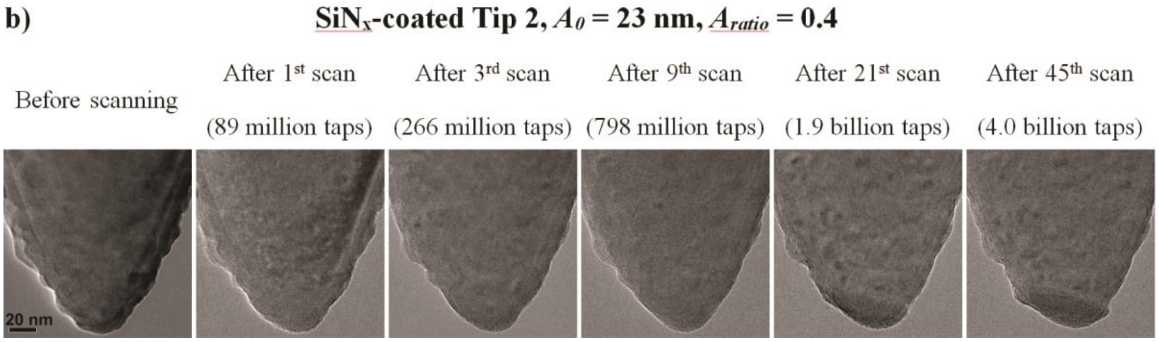

b) SiN_x-coated Tip 2, A_0 = 23 nm, A_{ratio} = 0.4

Figure 4.1: HR-TEM images of the SiN_x-coated silicon tips before any AFM imaging and after completing 1, 3, 9, 21, and 45 AM-AFM images on the UNCD sample. (a) and (b) correspond to two tips with different free oscillation amplitudes, A_0, and amplitude ratios, A_{ratio}.

In Figure 4.2, estimated tip radii as they evolve due to tip shape modification are plotted for the two SiN_x-coated tips. For each tip, there are two different plots corresponding to two different methods of estimating the tip radius. The first is estimated by BTR from the topographic images using the fast scan direction, which is perpendicular to the cantilever axis here and denoted by R_x; the second is estimated by comparing HR-TEM, and BTR from the topographic images using the slow scan direction as described earlier in section 3.1 and denoted by R_y. It is observed that R_x and R_y increase in magnitude as wear of the tips progresses. These increase in tip radii result in the degradation of the imaging performance and resolution.

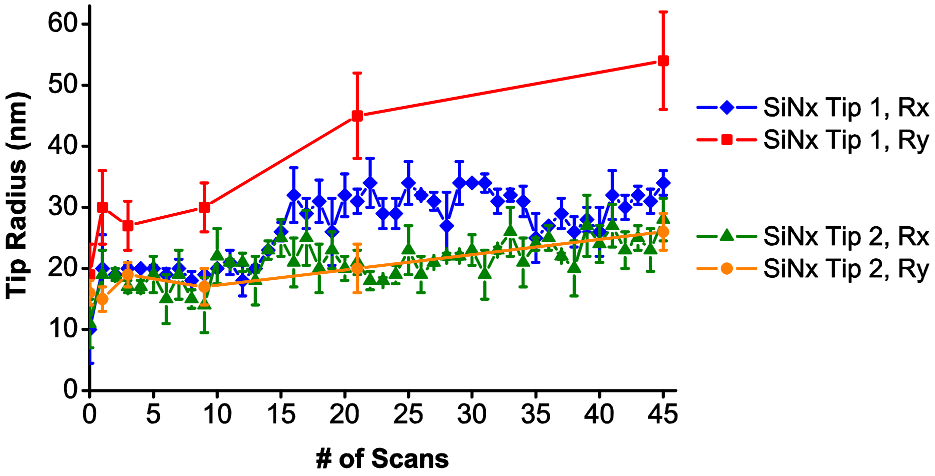

Figure 4.2: Tip radius estimated for the SiN_x-coated tips by BTR from the height images' fast scan direction (R_x), and combined HR-TEM and BTR of the height images' slow scan direction (R_y).

In Figure 4.3, the calculated peak repulsive forces as they evolve due to tip shape modification are plotted for the two tips. For each tip, there are three different plots corresponding to three different methods of calculating the peak repulsive force. The first is obtained by using Eq. (2.1) with $R = R_x$; the second using Eq. (2.1) with $R = R_y$; and the third using VEDA, the online tool mentioned in section 2.2, to verify our approach. R_y is used as the tip radius input for VEDA. In all cases, there is a close agreement between these two methods of force determination and the VEDA results sit within the standard error of the forces calculated using Eq. (2.1).

Tip 1 has the higher variation in the peak repulsive force (from about 54 nN at the beginning to 65 nN at the end using $R = R_y$). Considering this more closly, one can see that the tip radius changes from 19 ± 5 nm to 54 ± 8 nm. In other words, the final tip radius is approximately 2.8 times larger than the initial tip radius, while the final peak repulsive force is only 1.2 times larger than the initial force, supporting the fact that the peak repulsive force is not highly sensitive to the tip shape. Therefore, the approximation used here of fitting a circle or a parabola to the tip shape to calculate force does not introduce significant error in the peak repulsive force. For both tips, a modest increase in the peak repulsive force is seen early in the wear test, followed either by a leveling off or a more gradual increase. The initial rapid increase is attributable to the rapidly changing tip size at the outset of the wear test.

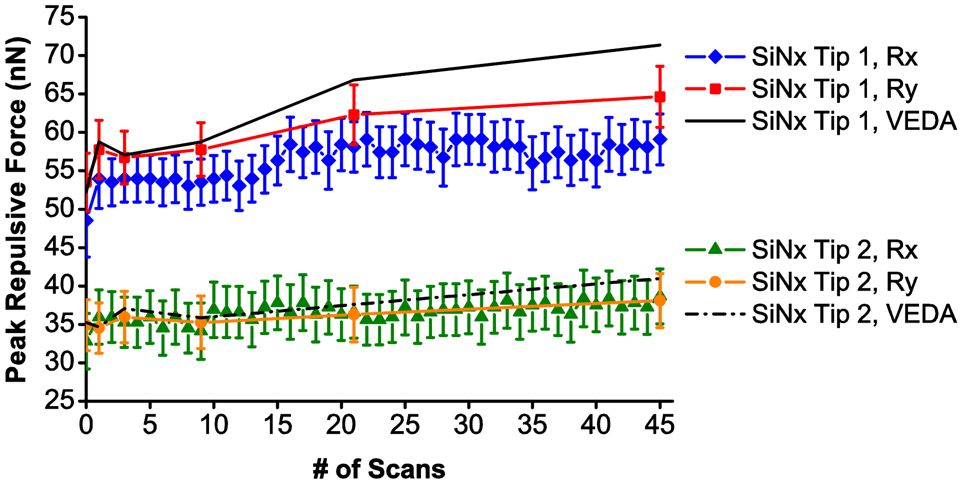

Figure 4.3: Peak repulsive forces calculated for the SiN_x-coated tips based on the tip radii estimated by BTR from the height images' fast scan direction (R_x), and combined HR-TEM and BTR of the height images' slow scan direction (R_y). Peak repulsive forces are also calculated using VEDA for verification.

The average normal stress versus the number of wear scans for the two SiN_x-coated tips is plotted in Figure 4.4. There are three stress values for each tip obtained by using the DMT model: one calculated assuming a paraboloidal tip with $R = R_x$, one assuming $R = R_y$, and finally one where the model of Zhou *et al.*[45] is applied to the axisymmetric tip shape based on the actual tip profile. The dramatic influence of ignoring the local details of the tip profile (by simply fitting a parabola/circle to the tip) is obvious, and demonstrates that an accurate stress calculation requires consideration of the actual tip profile.

The stresses using actual tip profiles of the SiN_x-coated tips are very large (beyond the elastic regime) because of the high local curvature at the contact as a result of the roughened tip. In other words, the asperity in contact is always rather sharp even though the entire tip gets generally blunter. The higher roughness of the SiN_x-coated tips can be observed in TEM images and calculated through roughness measurement discussed in section 4.4. Here, we assume elastic behavior for the stress calculation; since the stress exceeds the elastic limit and plastic behavior is observed, which is especially evident with the SiN_x-coated tips, the actual stresses are lower, and thus our calculated stresses are upper bounds. The stresses calculated from the parabola/circle fits provide a lower bound for the contact stresses because tip and sample roughness are ignored.

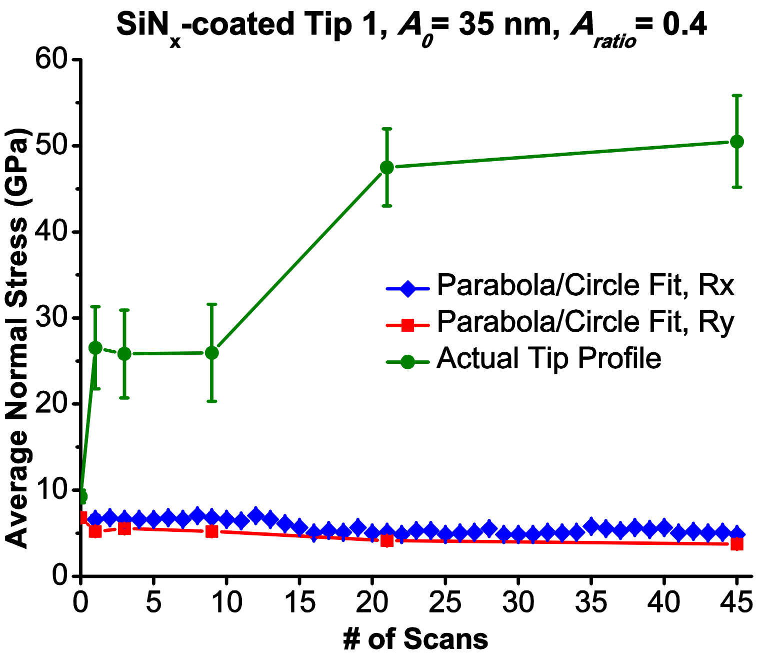

(a)

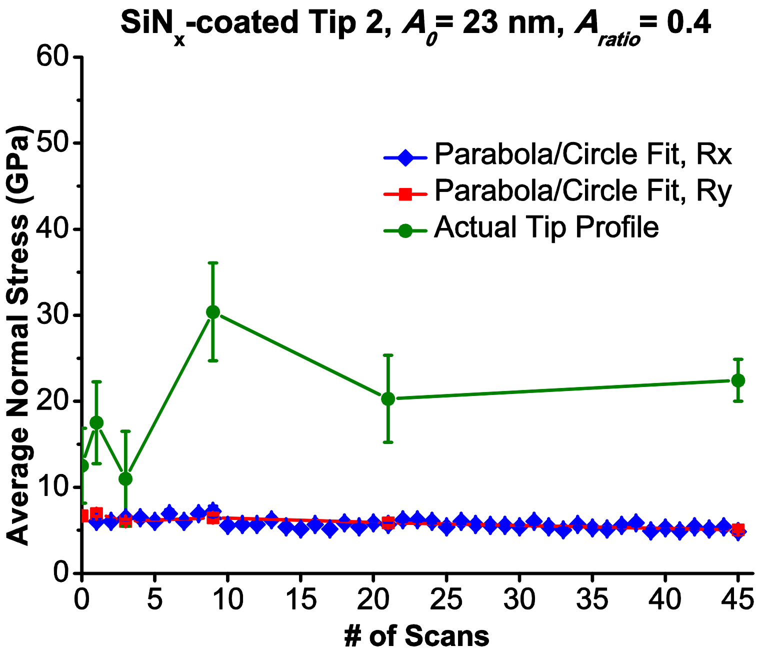

(b)

Figure 4.4: Average elastic normal stress calculated for the SiN$_x$-coated tips based on the tip radii estimated by BTR of the height images' fast scan direction (R_x), combined HR-TEM and BTR of the height images' slow scan direction (R_y), and the actual tip profile.

The wear volume of the SiN_x-coated tips *vs.* number of taps is shown in Figure 4.5. The data show a rapid increase in wear volume during the first one billion taps, and then the wear volume reaches a plateau. One thing to bear in mind when comparing different tips/cantilevers is that the same number of wear scans does not mean the same number of tip-sample interactions, since different cantilevers have different resonance, and consequently, drive frequencies. Therefore, the wear volume is plotted against the number of taps rather than the number of scans in Figure 4.5 and Figure 4.11.

Plotting the average number of taps that is required to remove or plastically displace one atom of the tip can reveal some aspects of the wear process (Figure 4.6). Note that the term "plastic displacement" is used here for silicon nitride tips because the volume displaced from the apex is not necessarily removed: some of it is plastically displaced to the side of the apex leading to the bulging of the worn tip seen clearly in Figure 4.1(a) starting from the 21st scan. Figure 4.6 shows that the number of taps to remove or plastically displace one atom changes by nearly 2 orders of magnitude during the 45 wear scans. This implies a rapid decline in the effectiveness of any wear mechanism governing the wear of silicon nitride.

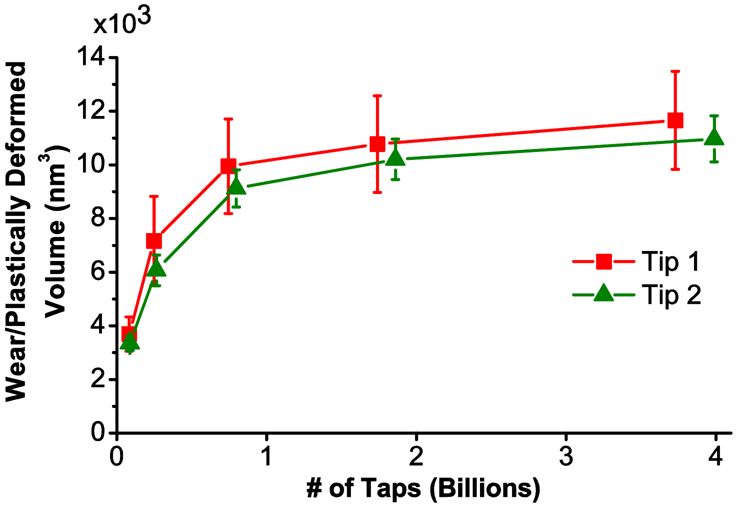

Figure 4.5: Wear volume of the SiN_x-coated tips as a function of number of taps.

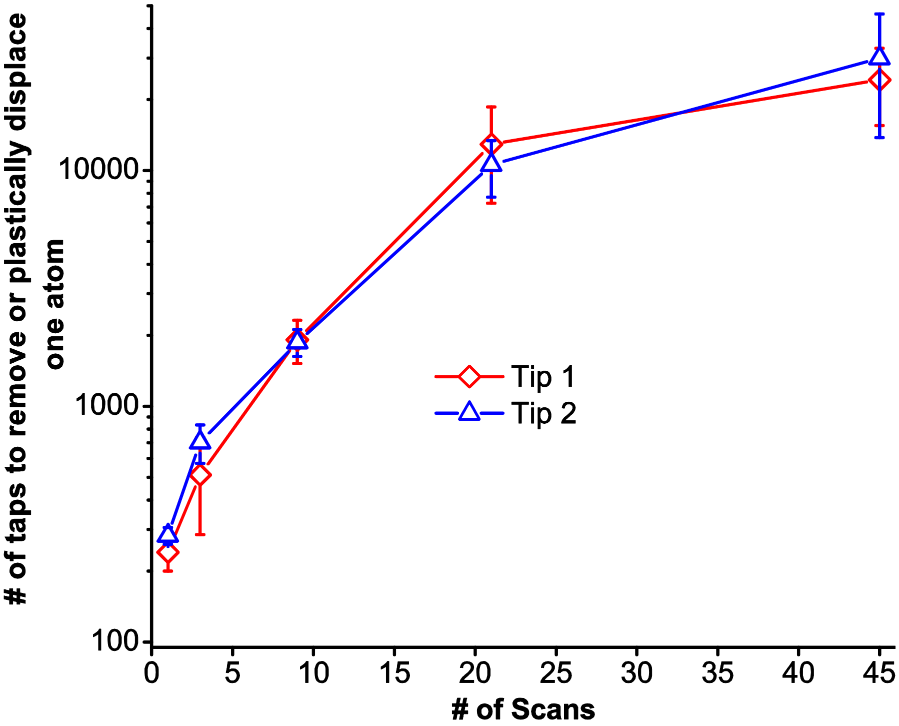

Figure 4.6: Number of taps to remove or plastically displace one atom of the SiN_x-coated tips as they wear out.

4.3: Diamond-Like Carbon Coated Silicon Probes

The frictional and wear behavior of DLC films with different compositions in sliding contact in various environments have been widely studied during the past two decades. The exceptional tribological properties of the DLC such as high hardness, inertness, and low friction coefficient (e.g. 0.003-0.0005 in the case of a-C:H sliding against a-C:H in dry nitrogen or 0.07 in the case of a-C:H sliding against SiC in dry air[67]) and wear rate (e.g. 0.00046-0.00015 [$\times 10^{-6}$mm^3(Nm)$^{-1}$] in the case of a-C:H sliding against a-C:H in dry nitrogen or 0.113 [$\times 10^{-6}$mm^3(Nm)$^{-1}$] in the case of a-C:H sliding against SiC in dry air[67]) in different environments have made DLC a popular material for tribological applications like magnetic hard disk, mechanical seals, microelectromechanical systems, space applications, etc.[59,67]

The low friction coefficient and wear rates are mainly attributed to the formation of graphitic transfer layer between the interacting bodies as the sp^3 bonding of the amorphous DLC is not thermodynamically stable. High contact temperature and loading can result in phase transformation to the more stable form, graphite.[68–70] Despite the widely studied tribological characteristics of DLC in sliding contact, its wear behavior in surface interactions involving repeated contact formation and breakage, specifically in AM-AFM, has not been investigated. This significantly motivates the present studies.

The HR-TEM images of the DLC-coated probes, taken before any AFM scanning, and after completing 1, 3, 9, 21 and 45 scans (1×1 µm^2, 512×512 pixels, 2 Hz scan rate) are presented in Figure 4.7. The contrast difference between the silicon and the respective amorphous coating is not present in these HR-TEM images. The specialty probe holder used for mounting the AFM probes in the HR-TEM allowed only limited sample tilt. Therefore, it was not always possible to tilt the crystalline silicon to an orientation of high-symmetry (*i.e.* high diffraction contrast).

After the 45th scan, the DLC coating of Tip 1 is completely removed and the original silicon tip becomes exposed. Therefore, the values of the calculated parameters such as force, stress, wear volume, etc. at the 45th scan of the Tip 1 are not plotted in the subsequent graphs. Also, a contamination particle becomes attached to Tip 3 sometime between the 3rd and 9th scans. The contaminant is visible in the HR-TEM images after 9th, 21st, and 45th scan, and is not within or close to the region of the tip apex that interacts with the sample. Therefore, it does not introduce any error in the estimation of the tip radius and consequently the calculation of the force and stress. For the wear volume calculation, the original tip profile, which is clearly visible under the contaminant, is used.

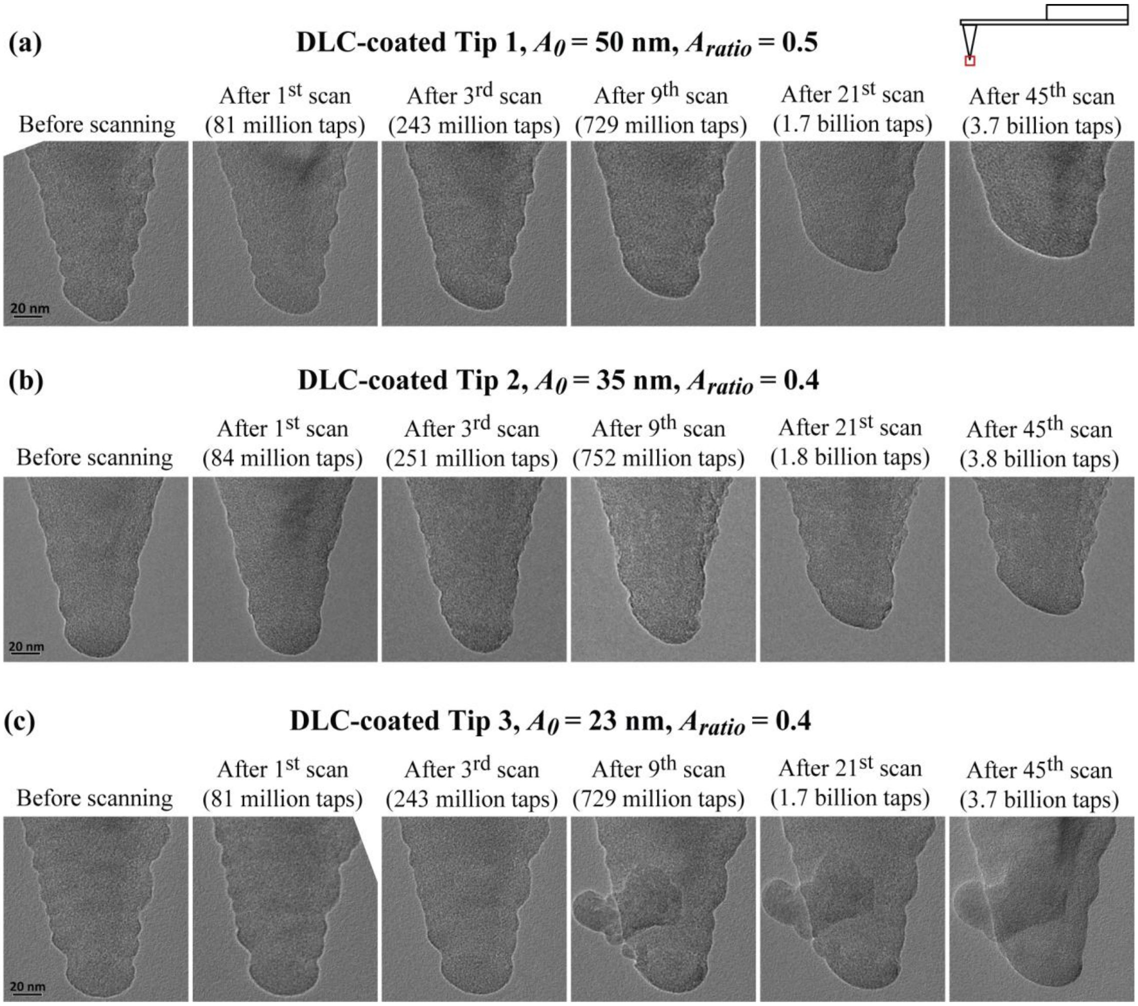

Figure 4.7: HR-TEM images of the three DLC-coated silicon tips before any AFM imaging and after completing 1, 3, 9, 21, and 45 AM-AFM images on the UNCD sample. (a), (b), and (c) correspond to three tips with different free oscillation amplitudes, A_0, and amplitude ratios, A_{ratio}.

Figure 4.8, Figure 4.9, and Figure 4.10 depict the evolution of the tip radii, peak repulsive forces, and average normal stresses of the DLC-coated tips. These plots are similar in character to the plots in Figure 4.2, Figure 4.3, and Figure 4.4 for silicon nitride coated tips; once again, fitting the true tip profile is found to be crucial.

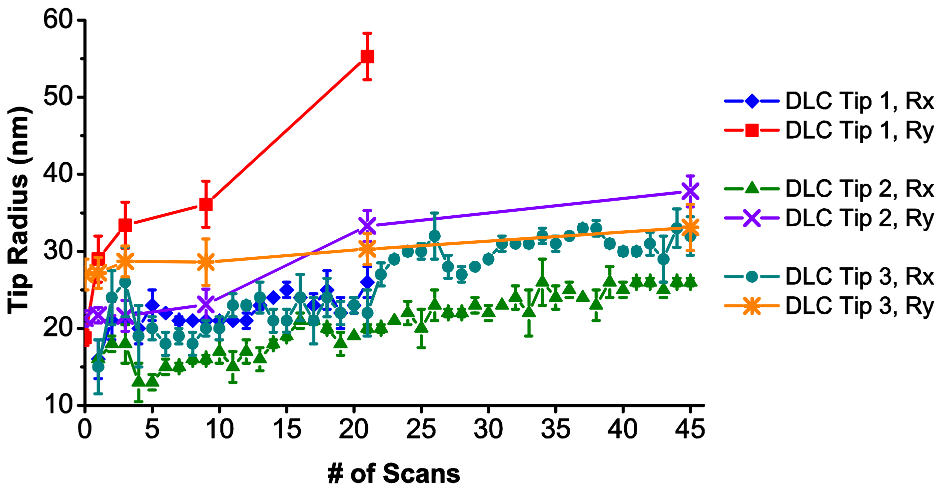

Figure 4.8: Tip radius estimated for the DLC-coated tips by BTR from the height images' fast scan direction (R_x), and combined HR-TEM and BTR of the height images' slow scan direction (R_y).

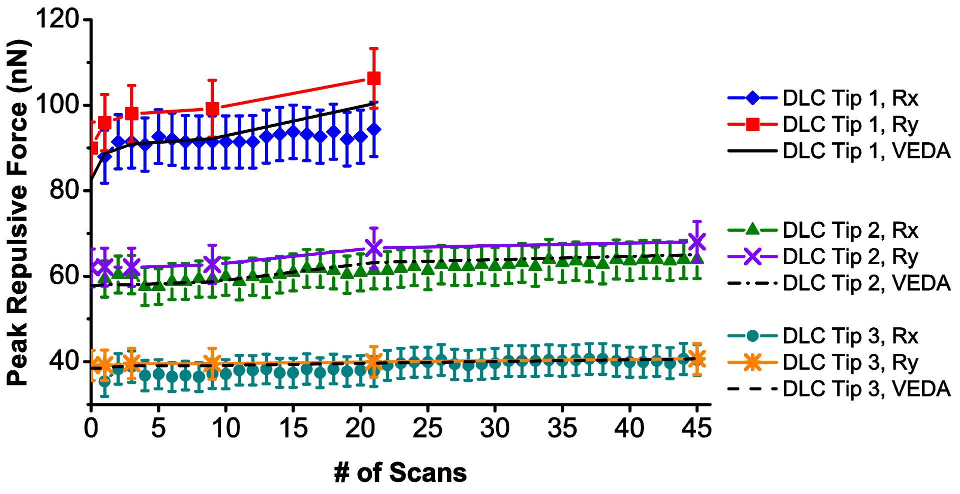

Figure 4.9: Peak repulsive forces calculated for the DLC-coated tips based on the tip radii estimated by BTR from the height images' fast scan direction (R_x), and combined HR-TEM and BTR of the height images' slow scan direction (R_y). Peak repulsive forces are also calculated using VEDA for verification. The data point after 21 scans of the Tip 1 is not shown as the DLC coating is completely removed after this.

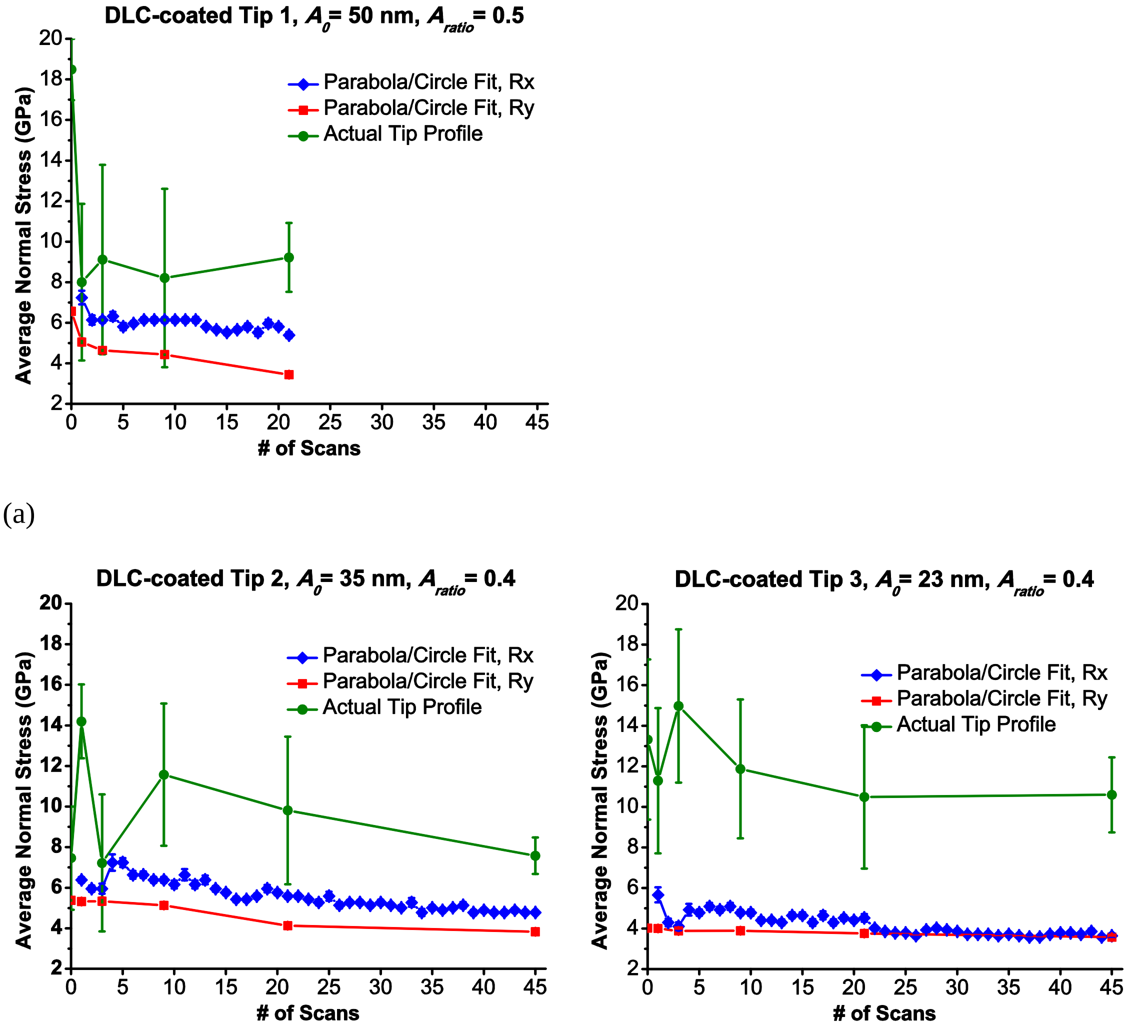

(a)

(b)

(c)

Figure 4.10: Average elastic normal stress calculated for the DLC-coated tips based on the tip radii estimated by BTR of the height images' fast scan direction (R_x), combined HR-TEM and BTR of the height images' slow scan direction (R_y), and the actual tip profile. The data point after 21 scans of the Tip 1 is not shown as the DLC coating is completely removed after this.

The plots in Figure 4.10 show that the average normal stresses calculated using the parabola/circle fit and the actual tip profile of all three tips. The stresses evolve to a steady-state value that is the nearly same for all three tips (≈ 4.1 GPa from parabola/circle fit and ≈ 10.8 GPa from actual tip profile) after a run in period even though the peak repulsive forces are quite different (98, 64, and 40 nN on average calculated using R_y). This reflects that the wear process is stress-controlled: tips experiencing higher normal forces and consequently higher stresses wear more rapidly than the ones with lower force and stress during the initial scans, but eventually the wear reduces once the stress reduces below a threshold value. As with the SiN_x-coated tips, the stress value from parabola/circle fit provide a lower bound, and values from actual tip profiles an upper bound to the true contact stresses.

4.3.1: Preliminary Study of Humidity Effects

A preliminary study of the effect of humidity was also conducted. For Tip 2 and Tip 3, the relative humidity was varied. From scan 1 to scan 45, the humidity was 15%, from scan 46 to scan 57 it was less than 5%, and from scan 58 to 69 it was 40%. The wear volume as a function of number of taps is shown in Figure 4.11. The wear rate is seen to change at different relative humidities; specifically, the presence of moisture promotes the wear mechanism/s and consequently accelerates wear. The effect of humidity can be seen more clearly in Figure 4.12, which plots the average number of taps required to remove one atom for each wear interval. As the humidity increases, fewer tip-sample interactions are required to remove one atom from the tip.

This effect could be due to the tribochemical effect/s that water has on bond formation between atoms at the surface of the tip and the sample. Based on previous studies, the macroscopic friction coefficient and consequently the wear rate of hydrogenated DLC increases as RH increases in the environment.[71–76] Increasing the RH results in the physisorption of water on the tip and sample surface. During the making and breaking of the contact, the high contact stresses can promote the dissociative chemisorption of water or oxygen molecules at dangling bond sites formed by breaking C−C and C−H bonds at the surface. A similar mechanism has been observed for diamond and tetrahedral amorphous carbon films in macroscopic sliding contact in humid environments.[77,78] In the present experiments, the RH is controlled by administration of dry nitrogen to the AFM chamber which is initially filled with laboratory humid air. The lower the RH is, the higher the percentage of nitrogen in the air-nitrogen gas mixture is. As oxygen and water are removed from the test environment, these tribochemical interactions are reduced.

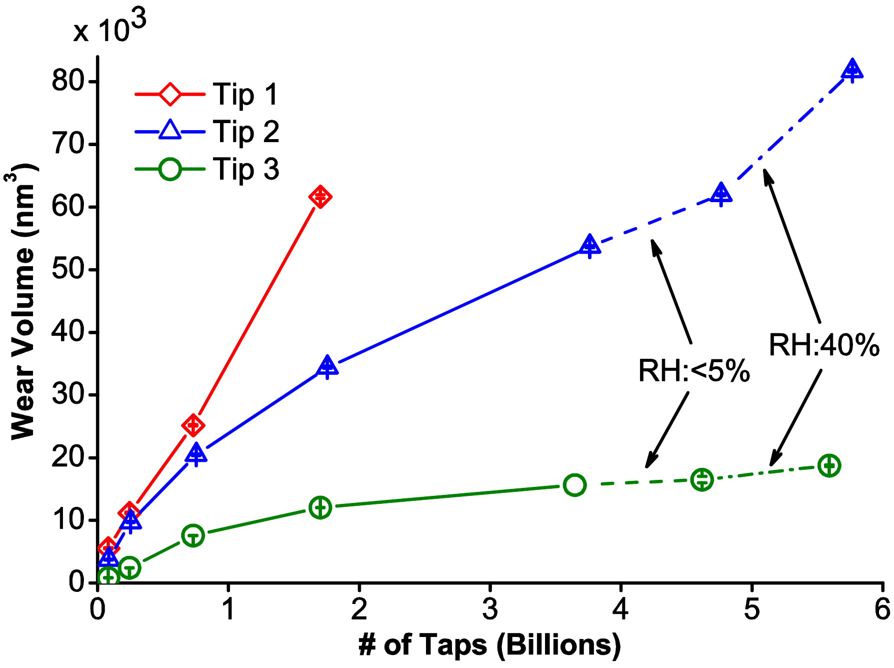

Figure 4.11: Wear volume for the DLC tips as a function of number of taps in a mixture of air and nitrogen gas with 15% RH. The standard error of the measured wear volume is negligible in compare to the wear volume itself and hard to be seen. The data point after 21 scans of the Tip 1 is not shown as the DLC coating is completely removed after this. The wear volume of the Tips 2 and 3 in less than 5% (dashed line) and in 40% (dash-dotted line) RH is also plotted.

4.3.2: Reducing DLC-Coated Tip Wear by Altering AM-AFM Parameters

The experimental results show that the nanoscale wear in DLC-coated AM-AFM probes can be significant. However, tip wear can be significantly reduced by choosing right experimental parameters. Both Figure 4.11 and Figure 4.12 demonstrate the dramatic difference between the wear of Tips 1 and 3. In Figure 4.12, we can clearly see that the number of tip-sample interactions required to remove one atom from Tip 3 is an order of magnitude more than Tip 1.

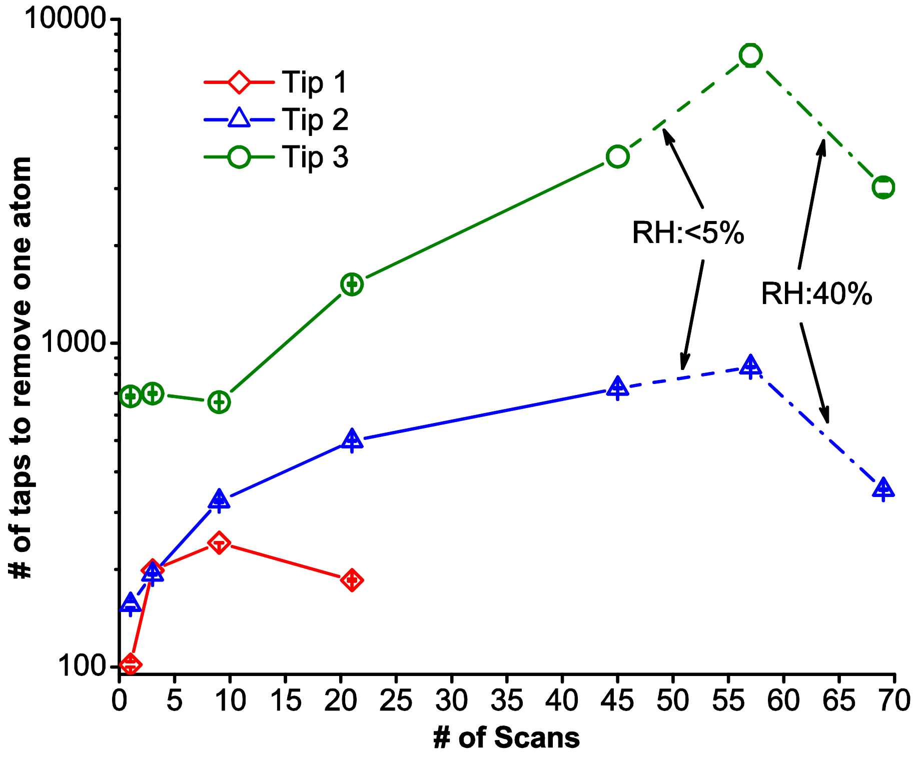

Figure 4.12: Number of taps to remove one atom of the DLC-coated tips as they wear out. The data point after 21 scans of the Tip 1 is not shown as the DLC coating is completely removed after this. The relative humidity up to 45th scan is 15%.

4.3.3: Gradual Wear Process of DLC-Coated Tips

HR-TEM images show no sign of fracture or plastic deformation, suggesting a gradual wear process for the DLC-coated tips. The gradual wear process can be also deduced from Figure 4.11, which shows a gradual change in the wear volume. This gradual wear process could be reasonably described as an atom-by-atom removal process: it can be seen in Figure 4.12 that the average number of taps (between successive HR-TEM images) needed to remove one atom varies from 100 to 8000. Even in the worst case, this is a very slow process. However, as in AM-AFM, tip-sample contact formation and breakage cycles are of the order of a few hundred thousand times per second (here, ~300,000 per second), the wear volume becomes significant after several billion taps over the course of the wear experiment. This behavior suggests utilizing a scheme that can describe this gradual atom removal, *e.g.* reaction rate theory. This is especially true when a modified phenomenological Archard wear model for AM-AFM fails to describe the wear process, which will be discussed in section 4.4.2.

4.4: A Comparison between the Wear of Silicon Nitride and Diamond-Like Carbon

The HR-TEM images show that wear in AM-AFM probes operating in repulsive-mode can be significant even in the case of hard, wear-resistant materials like silicon nitride and DLC. The significant wear observed in AM-AFM probes is evidently related to normal contact stresses exceeding a threshold required for the failure of the tip material, potentially in combination with interfacial chemical reactions that lead to removal of atoms.

The yield strength of silicon nitride thin films is reported to be approximately 13 GPa,[79] but this can vary substantially depending on the growth method. The yield strength of DLC used here varies from 7.3 to 10 GPa. These values are approximated from the hardness of typically 13 GPa and the measured Young's modulus of 120 to 180 GPa reported by K. Sridharan,[52] and the empirical equation proposed by Gan *et al.*[51] for the relationship between the hardness, Young's modulus, and yield strength of thin film DLC as follows:

$$\frac{H}{Y} = -0.36 + 0.67\,ln\left(\frac{E}{Y}\right). \tag{4.1}$$

In both DLC and silicon nitride tips, the calculated average normal stresses from actual tip profiles are above the yield strengths during the entire wear scanning process.

In examining failure, one can seek an appropriate yield criterion based on the material properties or experimental observations. In the case of the DLC, neither brittle fracture nor plastic deformation is observed. Therefore, using any yield criterion suitable for brittle failure, like the Mohr-Coulomb yield criterion,[80] or ductile failure, like the von Mises yield criterion,[80] is not justifiable. However, as mentioned above, in the case of silicon nitride, despite the fact that it is known to be a brittle material, plastic deformation is observed, and this accounts for a significant part of the tip damage that occurs. Therefore, as a first approach, we hypothesize that the von Mises yield criterion can be used to estimate required average normal stress for plastic deformation. Using the von Mises criterion also entails the assumption that the silicon nitride plastic yield strengths in tension and compression are the same, which is not the case as the bulk silicon nitride is known to be brittle. However, as the stress state in AM-AFM is highly compressive (particularly in the DMT regime), this assumption is not highly consequential.

In a Hertzian or DMT contact, the maximum shear stress occurs at $z = 0.57a$ along the z-axis from the interface at the center of contact, where a is the contact radius.[9]

If we express the von Mises yield criterion based on the principal stresses of the Hertzian contact, yield happens when the following is satisfied:

$$\left(\sigma_r - \sigma_\theta\right)^2 + \left(\sigma_\theta - \sigma_z\right)^2 + \left(\sigma_z - \sigma_r\right)^2 = 2S_y^2 ,$$

(4.2)

where σ_r, σ_θ, and σ_z are principal radial, tangential, and normal Hertzian stresses along the z-axis of the contact, and S_y is the yield strength of the tip material. By using the expressions for the Hertzian principal stresses at $z = 0.57a$ into Eq. (4.2), the von Mises criterion reduces to:

$$0.960\sigma_{average,yield}^{norm} = S_y .$$

(4.3)

The yield strength of the silicon nitride thin film is approximately 13 GPa. Using this value, one concludes that an average normal stress equal to or larger than 13.5 GPa will result in yield at $z = 0.57a$. In Figure 4.4, the plot of average normal stress *vs.* number of wear scans, it can be seen that the average normal stresses calculated from the actual tip shape for silicon nitride are in the range of 10 to 50 GPa, far exceeding 13.5 GPa after the first scan in the case of Tip 1, and after the third wear scan for the case of Tip 2. The vertical subsurface position where yield occurs varies from 0.4 to 0.5 nm based on the contact radii calculated from the actual tip shapes for both Tip 1 and 2. The average bond length in silicon nitride is about 1.73 Å,[81,82] which means yield approximately occurs two to three atomic bonds above the contact point.

From these it can be concluded that contact mechanics models used to calculate force and stress assuming fully elastic contact could be inaccurate. This suggests revisiting the solutions for forces and stresses by including the effects of plasticity, particularly for the case of AFM tips subjected to tapping conditions in the repulsive regime. This is a challenging task, since the nature of plasticity at the nanoscale is not fully understood and is still in need of significant development.

4.4.1: Wear Processes Observed in DLC- and SiN_x-Coated Si Tips Operating in Repulsive Mode AM-AFM

Wear of SiN_x-coated tips occurs largely through plastic deformation, which is readily apparent from the bulging of the flattened tip, and contrast changes at the apex in the rightmost images in Figure 4.1(a) and (b). Darker contrast in TEM will occur when a material is compressed and becomes thicker in the direction of the TEM beam (the direction normal to the image). It can be seen that the end of the tip has also become wider where the contrast is darker. Thus, this indicates that a "pancaking" effect has occurred, consistent with plastically deformed material. Also, although silicon nitride is a brittle material, plasticity is well-known to occur in highly compressive stress states such as in nanoindentation of thin-film silicon nitride.[83–85]

Fragmentation of clusters of atoms could be another wear mechanism deduced from the roughened tip apices, which are observed in all of the worn silicon nitride tips' images (Figure 4.13). This increase in roughness is also quantified through measuring the roughness values of the tip apices shown in Figure 4.13. To obtain an equivalent roughness of a flat surface, a parabola is fit to the tip profile captured from a TEM image, and then this best-fit parabola is subtracted from the actual tip profile over a 20 nm extent of the profile's length centered at the bottom of the tip (where it makes contact). The measured values show a decrease in the roughness of the DLC-coated tip and an increase in the roughness of the SiN_x-coated tips. This suggests that material removal in DLC is a gradual, atom-by-atom process as reported previously in a contact mode AFM wear study,[17] while for SiN_x-coated tips, nanoscale clusters of silicon nitride are apparently removed. The exact reasons for the different behavior are unknown, but it may be a result of nanoscale subsurface crack formation and propagation to the surface. This is supported by the fact that silicon nitride has lower macroscopic fracture toughness, $K_{IC} \approx 6.3$ $MPa \cdot m^{1/2}$,[79] than the DLC coating, $K_{IC} \approx 10.1$ $MPa \cdot m^{1/2}$.[86] However, further investigation is required to fully understand this complex process.

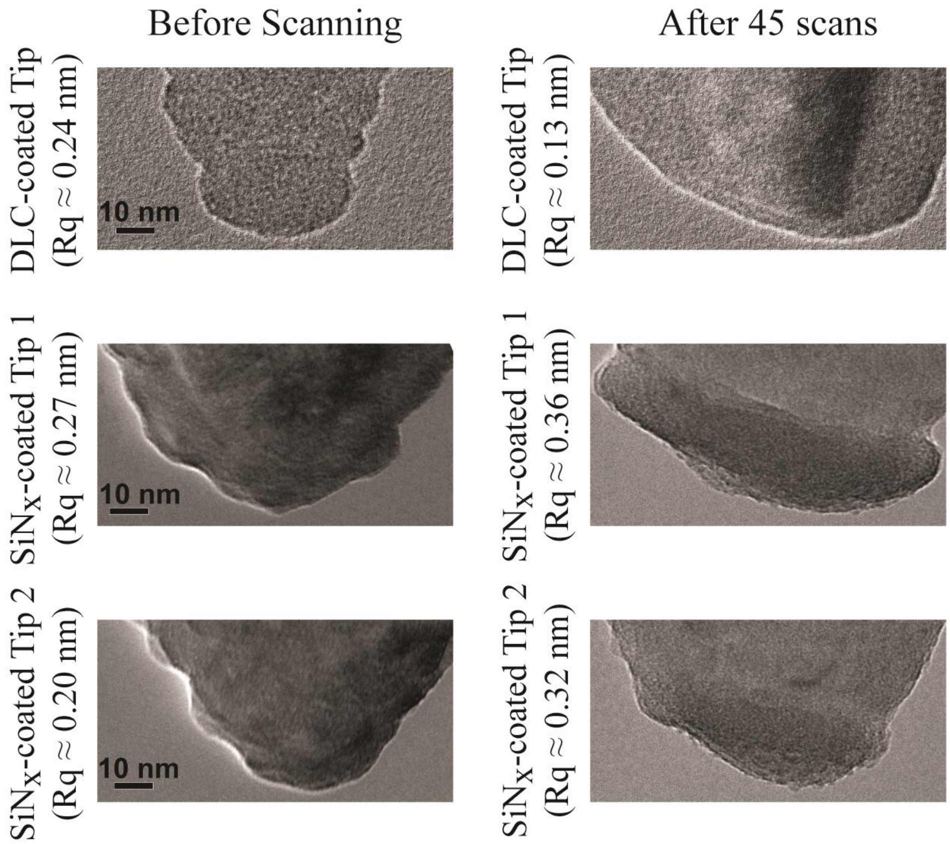

Figure 4.13: High magnification HR-TEM images of the tip apices before any scanning, and after 45 scans. The roughness change of the SiN$_x$-coated tips can be observed in the images after 45 scans. The roughness values measured over 20 nm-wide profiles of the tip apices also show a decrease in the roughness of the DLC-coated tip and an increase in the roughness of the silicon nitride-coated tips.

The roughness change in silicon nitride tips has another interesting consequence that can be seen in Figure 4.4. One can see that despite the overall increase in the tip radius, the stresses calculated from actual tip profiles do not decrease as the tips wear out. As mentioned before, this is because the local curvature of the asperities in contact does not change dramatically throughout the course of blunting. There is always a rather sharp asperity in contact than a broader region of the tip. Therefore, the changes in stresses and forces do not differ significantly. This is not the case with the DLC coated tip, where stresses estimated from the actual tip profile do not increase during the 45 wear scans.

Another difference between the wear behavior of DLC and silicon nitride can be observed in the change of their wear volume throughout the experiment. The rate of wear reduces slowly in DLC while it decreases rapidly and reaches to a plateau in silicon nitride (Figure 4.5 and Figure 4.11).

The different wear behavior for DLC and silicon nitride can be also seen in Figure 4.6 and Figure 4.12. Figure 4.6 shows that the number of taps required to remove or plastically displace one atom of silicon nitride ranges from 240 to 30000, while the number of taps required to remove one DLC atom ranges from 100 to 3500.

The different wear behavior, including the increased wear rate of DLC compared with silicon nitride, may have multiple origins. Once one or more bonds form between a tip atom and atoms on the surface of the sample, when the tip retracts, that tip atom may get left behind on sample's surface (*i.e.*, strained bonds in the tip are preferentially broken). Therefore, higher wear could result if there are a greater number of atoms in the DLC tip compared to silicon nitride which are either weakly bonded, or whose bond strength is easily lowered due to the presence of stress. Furthermore, the DLC may have a greater tendency to form covalent bonds (carbon-carbon bonds) with the UNCD surface as compared with silicon nitride (which would require Si-C or N-C bonds to form). This formation and breaking of such bonds is known to be affected not only by stress but also by environmental species. Finally, the observed plastic flow in the silicon nitride may result in a form of work hardening at the tip apex that makes it more difficult to remove or displace tip atoms. Further studies are needed to elucidate these mechanisms. Our results here provide clear qualitative observations of the characteristics of this nanoscale wear and also provide quantitative values for the forces, stresses, and wear volumes that need to be accounted for in a description of these mechanisms.

4.4.2: An Archard-Like Wear Model

To understand the wear mechanism in AM-AFM probes, one can begin with wear models that exist for wear at the macroscopic scale, and see if they can be related to the wear processes in nanoscale. Archard wear model[87] is the most famous phenomenological model for sliding contact, and is found to apply rather well to macroscopic sliding contacts between a wide range of materials once they have been slid beyond their initial transient "run-in" period. The law states that the worn volume is linearly proportional to the normal applied force times the distance slide:

$$V \propto F \cdot d \,, \tag{4.4}$$

One of the assumptions used in this model is that the contact happens where the surface asperities touch due to the surface roughness. The other assumption is the proportionality of the real contact area with the applied load. However, this formulation cannot be used directly in AM-AFM since the tip and sample interact through cyclic contact formation and breaking, as opposed to sliding. A simple, analogous relation can be constructed by replacing the sliding distance with number of taps. In other words, we can hypothesis that the worn volume is proportional to the number of taps times the peak repulsive force and examine it by the experimental data at hand. Eq. (4.4) can be modified as follows:

$$V \propto F_{peak}^{rep} \cdot (\#\ \text{of Taps}) \,. \tag{4.5}$$

The applicability of Eq. (4.5) is examined by plotting the worn volume *vs.* number of taps multiplied by peak repulsive force in Figure 4.14. Plots for DLC and silicon nitride probes show a sublinear dependence of wear volume on the number of taps times peak repulsive force, in contradiction to Eq. (4.5). Interestingly, the two plots of the SiN_x-coated probes collapse to one curve, suggesting that wear is dependent on the number of taps multiplied by force as a whole. However, DLC-coated probes do not show the same behavior.

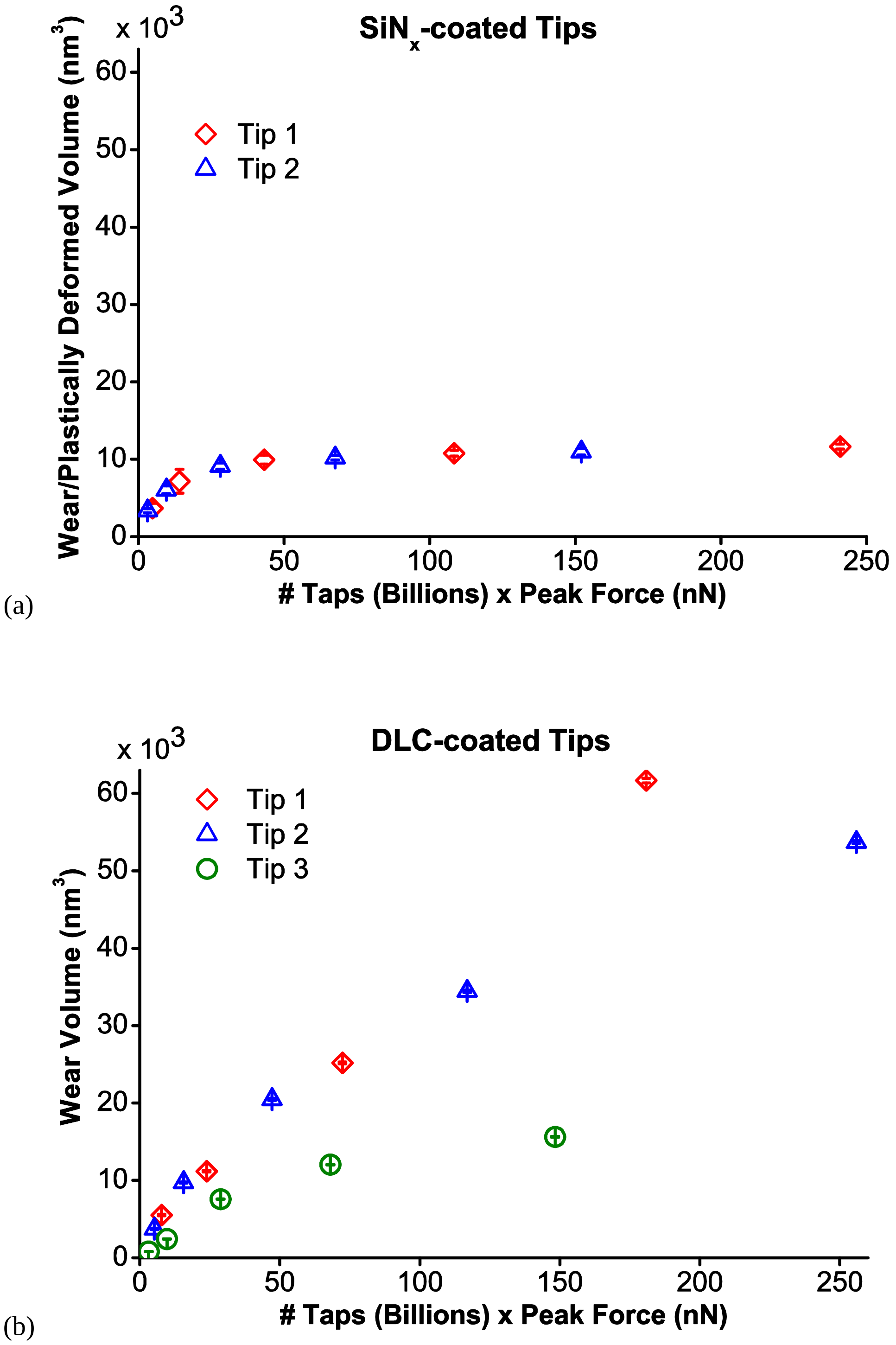

Figure 4.14: Wear/plastically deformed volume as a function of number of taps multiplied by peak repulsive force.

4.5: Reaction Rate Theory Applied to AM-AFM

Some researchers have observed that a thermally activated mechanism (formulated by transition state theory or reaction rate theory) can describe the wear process of DLC. Jiang *et al.*[88] considered the effect of sliding speed on the wear of DLC by sliding a tungsten carbide ball on a DLC coated disk in ambient air with 7% RH. They observed two different regimes: first, the wear rate decreased as the sliding speed increased from 0.048 to 0.25 m/s; second, in contrary to the first regime, the wear rate increased as the sliding speed increased from 0.25 to 0.45 m/s. To describe these opposing behaviors, they proposed a chemically activated debonding process at the tip of the DLC surface cracks promoting the crack propagation. In the first regime, increasing the sliding speed resulted in less available time for reactive species, most probably oxygen and water, to migrate to the crack tip and consequently decreasing the rate of particle removal. In the second regime, as the sliding speed increased, elevated contact temperature enhanced the migration and chemical reaction of the species with the atoms at the crack tip. It also increased the possibility of surface oxidization, resulting in an increase in the rate of crack propagation and particle removal. Their experimental results were in agreement with a thermally activated model predicting the specific wear rate as an exponential function of the velocity dependent temperature. The estimated apparent activation energy was about 27.04 kJ/mol which corresponds to about 0.28 eV per atom.

Also, in a single asperity sliding contact experiment, using a silicon-containing DLC coated AFM tip scanning against SiO_2, Bhaskaran *et al.*[17] observed an atom-by-atom removal process and calculated an effective energy barrier of 1±0.1 eV to remove one atom from fitting their experimental data to a thermally activated wear model proposed by Gotsmann and Lantz.[16] The corresponding effective activation volume was estimated to be 340±200 Å^3. The effective activation volume is equal to $\xi \Delta V_{act}$ where ξ is the pressure dependence of the interfacial shear stress and is not reported by the authors.

The gradual, atom-by-atom wear process observed in the experimental results in this study suggests that the wear of DLC in AM-AFM could be described by a thermally activated mechanism.[16–18] In this mechanism, the transfer of atoms from the tip to the sample are pictured as transferring from an equilibrium state at the bottom of a potential well to another equilibrium state with a minimum potential energy by overcoming an energy barrier (Figure 4.15 and Figure 4.16). This pathway along the reaction coordinate is the one with the lowest energy required for transition among all other possible pathways. The intermediate state at the top of the energy barrier is called activated state. The activated state is assumed to be unstable just along the reaction coordinate and is stable in all other directions. In other words, the atom of interest has one degree of freedom and if it makes to the top of the hill (the activated state), it can then go forward and complete the transition.

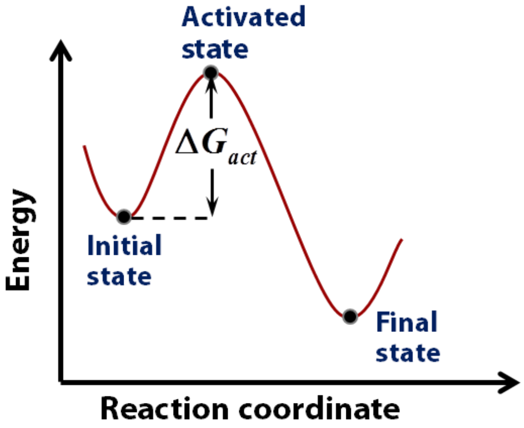

Figure 4.15: The atom transfer from tip to the sample is simulated by a double-well potential. ΔGact is the energy barrier that should be overcome by the tip atom to transfer from initial to final equilibrium state.

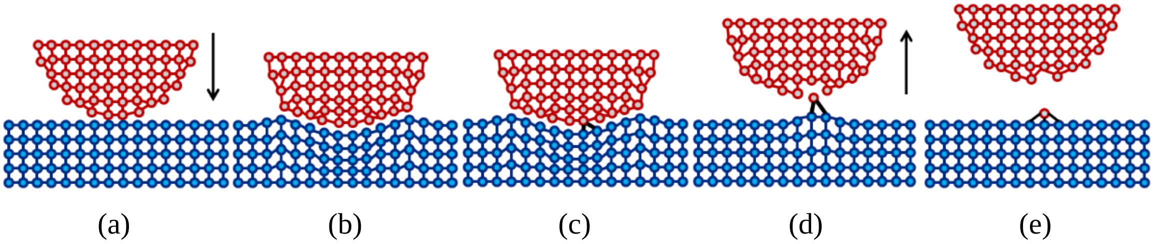

Figure 4.16: A possible atomic-scale schematic of the thermally activated process for atom transfer in AM-AFM. Here, both the initial and activated states could happen in state (b) or (c). The activated state is when the tip atom coordination state is lowered enough to be removed by the bond/s made with the sample atom/s.

The application of reaction rate theory to nanoscale wear is discussed extensively by Jacobs *et al.*[18] and the reader can refer to it for further details. Briefly, based on the reaction rate theory, the rate of atom loss or the number of atoms that can successfully pass the energy barrier per second, $\Gamma_{atom\text{-}loss}$ (s^{-1}), depends exponentially on a stress component promoting the reaction as follows:[89]

$$\Gamma_{atom-loss} = \left\{ \Gamma_0 \, exp\left(-\frac{\Delta U_{act}}{k_B T} \right) \right\} exp\left(\frac{\sigma \Delta V_{act}}{k_B T} \right), \tag{4.6}$$

where Γ_0 is the attempt frequency which is in the order of atomic vibration, $\approx 10^{13}$ Hz, ΔU_{act} is the internal energy of activation which is the energy difference between the activated and initial states and can be reduced by introducing stress, σ is a stress component reducing the energy barrier thus promoting wear, ΔV_{act} is the activation volume, k_B is the Boltzmann's constant, and T is the absolute temperature.

The accurate application of the Eq. (4.6) to the nanoscale wear strongly depends on the choice of stress component which should have the highest impact on the wear process. In AM-AFM, all the stress components are at their maximum value at the closest tip-sample distance in a tapping cycle which is a result of the repulsive force reaching its maximum value. Understanding the possible mechanism that results in atom removal from tip can help to better choose the stress component in charge of pushing the process forward. An atomistic picture can be helpful in this context. Figure 4.16 demonstrates a schematic view of a possible interaction between the tip and sample that actually results in an atom being removed. The cyclic loading and unloading of the tip atoms can result in lowering the coordination state of the atoms that already have distorted (stretched or compressed) or unsaturated bonds, which are abundant in DLC because of its amorphous structure. In parallel, in a different process, the normal compressive stress at the interface promotes the formation/s of the C-C or H-C bonds between the tip and sample. However, these newly formed bond/s between the tip and sample atoms are not necessarily stronger than the bonds that keep the atom/s connected to the tip unless the tip atom/s reach to a low enough coordination state that cannot further support their connection to the tip. Therefore, the rate limiting factors should be both the bond formation and the lowering of the coordination state of the tip atoms. Based on this picture, both the initial and activated states could happen in the configurations depicted in Figure 4.16 (b) or (c). Because of DLC's amorphous structure there is no preferred direction for bond breaking; therefore, any Hertzian stress component can lower the coordination state of the tip atoms. However, the stress component with the largest value is the dominant one. In the Hertzian stress distribution, the normal compressive stress at the interface is the largest (Figure 4.3 of "Contact Mechanics" by Johnson[9]) and for this reason, we choose it as the wear-promoting stress component. It should be noted that interfacial shear stress is minimal in AM-AFM and it is less likely to promote wear more than Hertzian stress components.

To successfully apply Eq. (4.6) to AM-AFM, a few simplifying assumptions need to be made. First, a single value for the normal contact stress is used. In fact, the normal contact stress is not uniform across the interface. In a Hertzian contact, the normal stress is maximum at the center of the contact and in a parabolic fashion approaches zero at its periphery. However, for simplicity, we assign a single value for the stress experienced by the tip atoms at the interface between two successive TEM images by assuming that all atoms are subjected to the average normal stress across the interface. Not utilizing this assumption requires expressing the rate of atom loss as a function of the radial position at the contact and a subsequent integration. However, recent modeling has suggested that the normal stress distribution for a nanocontact between amorphous materials does not strictly follow the Hertzian distribution at the atomic scale (Figures 3 and 4 of the paper by Luan and Robbins[12]). Rather, the normal stress is more evenly distributed over the contact area in comparison to the Hertzian continuum model or a tip with crystalline structure.

Second, we assume that the average normal stress stays constant over the contact time for each cycle. In AM-AFM, the tip-sample interaction force and consequently the stress change during the contact time at each tapping cycle; this is not an issue in contact mode AFM which is performed at a constant force. The error arising from these two assumptions is difficult to determine due to a lack of knowledge of the contact stresses at the atomic scale. However, by using the peak stress during the time of interaction, as opposed to the mean stress during the interaction, the calculations likely represent an upper bound to the stresses that are experienced.

The rate of atom loss of Eq. (4.6) can then be calculated using the following relationship that normalizes the number of atoms being removed in an interval by the contact area and time:[89]

$$\Gamma_{atom-loss} = \frac{V_{wear} \cdot \rho_{bulk}}{A_{cont} \cdot \rho_{surf} \cdot t_{cont}}, \tag{4.7}$$

where V_{wear} is the incremental wear volume measured by subtracting tip volume calculated from the consecutive HR-TEM images, ρ_{bulk} and ρ_{surf} are the number density of the bulk and surface of the material which for a perfectly amorphous material, ρ_{surf} can be approximated by $\rho_{bulk}^{2/3}$, A_{cont} is the contact area which could be calculated using the peak repulsive force and DMT contact model, and t_{cont} is the contact time between the tip and sample which in AM-AFM can be estimated by multiplying the contact time in an oscillation cycle by the number of taps in the given interval of the calculated wear volume. Therefore, Eq. (4.7) can be rewritten for the case of AM-AFM as follows:

$$\Gamma_{atom-loss} = \rho_{bulk}^{\frac{1}{3}} \cdot \frac{V_{wear}}{A_{cont} \cdot \#\ of\ taps \cdot t_{per-cycle}} \cdot \tag{4.8}$$

As mentioned above, each incremental wear volume is calculated by subtracting the estimated tip volume of two successive TEM images. On the other hand, we evaluate average contact stress, contact area, and contact time at every TEM image; therefore, for a given incremental wear volume, we have two values for these parameters and the average of these two values should be used for Eqs. (4.6) and (4.8).

The value of ρ_{bulk} is calculated to be approximately 144±5 atoms per nm^3, using the measured hydrogen content and the density of the DLC. Approximately 85 of these atoms are carbon atoms and 59 of them are hydrogen atoms. As with the average normal stress, the contact area is also assumed to be constant over the contact time in a single contact cycle. Regarding the contact time in a tapping cycle, unfortunately, there is no reliable closed-form equation to calculate it in an oscillation cycle; however, one can numerically solve the equation of motion of the cantilever's first flexural mode using a point-mass spring model with one degree of freedom as it was discussed earlier in section 1.2.[29] One can also use VEDA, mentioned in section 2.2, to calculate the contact time by providing AM-AFM scanning parameters, tip and sample material properties, and an appropriate contact mechanics model. We have verified that the estimated contact time using VEDA is in close agreement with our custom MATLAB script that simulates a cantilever approaching to and retracting from a surface in AM-AFM mode using the point-mas model. The data presented in this work uses the contact time estimated using VEDA.

Figure 4.17 plots the reaction rate, *i.e.*, the rate of atom loss, versus average normal stress for the three DLC-coated tips. Also plotted is an exponential fit (solid line) which agrees within error with the data, indicating that an exponential relationship between the reaction rate and average normal stress is possible. The calculated activation volume associated to the best exponential fit is 5.5±0.8 $Å^3$ and the activation energy is 0.8±0.8 eV. The activation volume is on the order of atomic volume and the activation energy is in the order of bond energies. The large variation in the activation energy is mainly because of the fact that only a limited range of stress values could be accessed, and these experiments are performed at a single temperature. An accurate determination of the activation energy could be more readily determined by conducting experiments at different temperatures.[18] Regardless, the estimated range of activation energies is consistent with the values predicted by Jiang *et al.*[88] (0.28 eV per atom) and Bhaskaran *et al.*[17] (1.0±0.1 eV). Jiang *et al.* did not report any activation volume, but Bhaskaran *et al.* calculated the effective activation volume for the silicon containing DLC to be 340±200

Å^3 which, as discussed above, cannot be broken further as they did not measure the pressure dependence of the interfacial shear stress. While the physical interpretation of the activation volume is subject to debate, it is often associated with the volume on which the stress does work to displace atoms to lead to the activated state. In this picture, the atomic-scale volume determined from these experiments is consistent with an atomic-scale wear process.

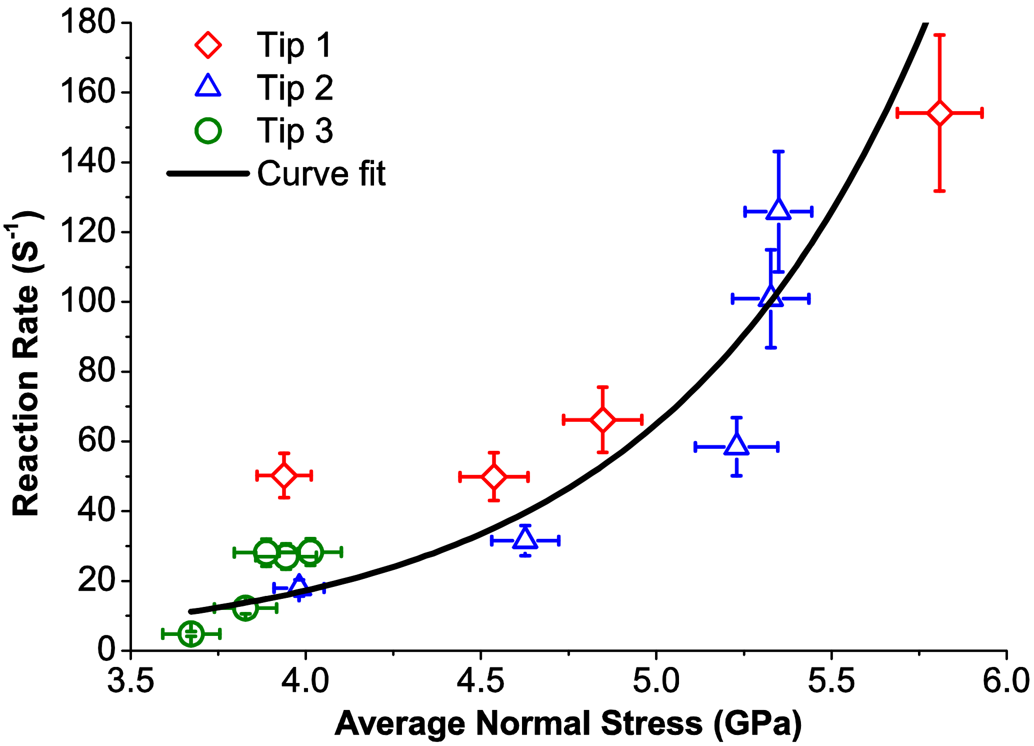

Figure 4.17: Calculated reaction rates plotted as a function of average normal stress for the case of DLC-coated tips. An exponential function is fit to the data points.

In summary, in this chapter we discussed the different wear behavior that DLC- and SiN_x-coated silicon probes show in AM-AFM repulsive mode imaging. Wear of SiN_x is characterized by the plastic deformation and removal of the clusters of atoms and the wear of DLC is consistent with a gradual atom-by-atom removal process. An Archard-like wear model fails to describe wear of these two materials in AM-AFM. The gradual wear of DLC can be modeled as a stress-assisted process formulated in the context of the reaction rate theory.

Chapter 5 : CONCLUSION, AND FUTURE WORK

We have discussed the mechanics of the tip-sample interaction in AM-AFM and introduced the most useful analytical equations to calculate forces and stresses. The analytical solutions are combined, simplified, and visualized in the form of stress maps to help users readily choose an appropriate AM-AFM cantilever and free oscillation amplitude for an AM-AFM experiment to avoid tip/sample damage or plastic deformation.

We have also developed and applied a new AM-AFM wear protocol to study the wear of AFM probe tips operating in tapping mode. The protocol uses a UNCD counter surface. The protocol enables a physically reasonable determination of the interaction forces and the elastic stresses by taking into consideration the complex tip geometry. The protocol was applied to DLC and SiN_x-coated tips tapping against a UNCD sample. We have shown how the peak repulsive force and the average elastic normal stress for these tips evolve as the tip geometry changes. Our results demonstrate that tip wear, even for tips with hard, wear-resistant coatings, can be significant in AM-AFM imaging.

To reduce wear, the AM-AFM user can exercise several choices. First, choosing tapping mode parameters that reduce the peak repulsive force will reduce wear. In particular one should try to operate in attractive regime if there is a wide enough range of amplitude ratios that tip can stay in attractive regime without falling into the bi-stable regime. If operating in repulsive regime, the smaller amplitude ratios way below the 0.5 to 0.6 result in reduced peak repulsive force for a given free oscillation amplitude. Also, operating in small amplitude ratios has the advantage of generating height images with less noise and better resolution in compare to the attractive regime imaging. In addition, choosing appropriate cantilever and free oscillation amplitude as described in section 2.4 reduces the chance of experiencing high contact stresses preserving the tip and sample from being damaged. Choosing a larger tip will also reduce stresses. This has the obvious drawback of reducing spatial resolution. However, in some cases, lower spatial resolution may be a worthwhile trade-off if stable, consistent observations with AM-AFM are desired. For example, if one seeks to compare the properties of a series of samples using AM-AFM, the comparison will be seriously hindered by a changing tip; working with a larger tip radius will alleviate this problem. Finally, using hard tip materials is beneficial, as seen before for contact mode tips.[13,17,90] Advanced materials tolerant to a wide range of environments such as UNCD[13,91] may have potential for such improved performance. Combined with proper selection of AM-AFM operating parameters, AM-AFM operation with significantly extended endurance of the tip is readily attainable.

We find, under harsh AM-AFM operation conditions, that the overall wear rate of SiN_x-coated tips is superior to that of the DLC-coated tips studied here. The observed evolution of the silicon nitride tips is consistent with plastic deformation and removal of nanoscale fragments; further studies are required to fully validate this. For DLC, a smoother evolved tip profile indicating a more gradual wear process is observed. However, depending on the experimental parameters, wear can be significant due to the large number of tip-sample interactions per second (~300,000) and the high contact stresses that are achieved.

A modified Archard wear model for AM-AFM fails to describe the wear behavior of DLC and silicon nitride. However, a stress-assisted thermally activated process is consistent with the dependence of the rate of atom loss with mean normal contact stress for the case of DLC-coated tips operating in AM-AFM. Finally, the presence of water in the environment increases the wear rate of DLC used here. The results are consistent with atom-by-atom removal, as observed in previous studies of sliding contacts.[17,88] This work presents the first report supporting atom-by-atom removing in AM-AFM mode.

The results and discussions in this dissertation shed light on several aspects of the tip-sample interaction, and of wear in AM-AFM. However, there are numerous unknowns and unresolved issues that need to be investigated to more fully understand the governing wear mechanisms. In the following, a list of recommended studies that can extend this work is presented.

1. A direct time-resolved measurement of the instantaneous tip-sample force is crucially important to determine the accuracy of the closed-from equations (such as Eq. (2.1)) and the numerical solutions (such as VEDA). This can be done by utilizing the interferometric-force-sensing AFM probe that Sarioglu *et al.*[92] proposed. In this probe, a small interferometric high-bandwidth grating force sensor is integrated at the end of the cantilever.

2. As mentioned before, the contact stresses can readily pass the elastic limit of the tip and sample materials, invalidating the assumption of fully elastic contact in almost all

the studies performed on the dynamics of the AM-AFM. Therefore, all of the approaches used to derive tip-sample forces and stresses may have significant errors. Replacing elastic contact mechanics models with elastic-plastic ones, such as the models proposed by Chang *et al.*[93] or Zhao *et al.*[94], should be evaluated and potentially applied to examine the impact of plasticity in prediction of the forces and stresses.

3. A direct observation of the tip-sample interaction, such as performing *in-situ* HR-TEM imaging of a vibrating tip similar to what Jacobs *et al.*[89] did for the case of contact mode AFM, can reveal key aspects about the nature of the force interactions in AM-AFM.

4. Molecular dynamics should be utilized to simulate the wear of AM-AFM probes considering the availability of the potentials capable of realistically predicting the bond-formation and breakage to the tip and sample atoms. One advantage of molecular dynamics is the possibility of probing forces and stresses at the atomic level, which is unattainable by any experimental technique. Also, the buried interface of the tip-sample contact can be directly observed, which is again currently inaccessible by any instrument.

5. At the macroscopic scale, when two contacting surfaces slide against each other, the volume removed due to wear is a function of the energy dissipated by frictional forces

(Archard wear mode[87]). Recently, Agrawal *et al.*[95] suggested from experiments that this concept can be applied at the nanometer scale, with a single-asperity, parabolic tip sliding over a sample in contact-mode AFM. Based on this, a wear model was proposed for contact mode. It is not clear, however, what fraction of the frictional work is dissipated by heat or other processes that do not contribute directly to wear. However, regardless of the limitations and shortcomings of this model, it is certainly fruitful to consider the relationship between dissipated energy and wear in AM-AFM as well, as the measured energy dissipated represents an upper bound to that which may be channeled to wear mechanisms. As opposed to contact-mode conditions, dissipation in AM-AFM does not originate substantially from friction. For typical AM-AFM setups, which all have a significant tilt angle of the cantilever with respect to the surface of the sample, the dissipated energy due to friction has been measured to be less than 10% of the total dissipated energy for a silicon tip and substrate.[96] The virial[97], which represents stored energy in the conservative tip-sample interaction, can also be measured and tracked for a possible contribution to the wear.

6. Performing wear experiments on different materials commonly used to fabricate or coat AM-AFM probes such as silicon in various ambient conditions (temperature, gas species, and relative humidity) is also useful to determine if other wear mechanisms are active in AM-AFM.

7. Nanoscale fracture is a phenomenon that has been frequently observed in AFM tips, especially during the initial tip-sample engagement.[20] Atomic-scale fracture could occur during tapping, and could play an important role in tip wear. Therefore, it is worthwhile to be aware of its existence, and to consider mechanisms that initiate and extend nanoscale cracks. While fracture during tip-sample engagement at the scale of tens of nanomaters or larger could be easily observed in our experiments, fracture at the atomic-scale is much more challenging to monitor. In-situ HR-TEM and molecular dynamics simulations similar to the work done by Huang *et al.*[98] to investigate the mechanics of nanoscale cracks could be utilized to investigate fracture as a common mechanism degrading the quality of AFM operations.

8. Some of the differences in the wear behavior of the DLC and SiNx in AM-AFM could be related to the choice of substrate (UNCD) used in these studies. As discussed in section 4.4.1, DLC may have a greater tendency to form covalent bonds (carbon-carbon bonds) with the UNCD surface as compared with silicon nitride (which would require Si-C or N-C bonds to form). To verify if such an atomic interaction causes some of the differences, one should repeat the same experiments using SiN_x as the substrate instead of UNCD. In that case, SiN_x-coated tip may have a greater tendency to form covalent bonds with the SiN_x surface as compared with DLC. This can result in wear processes different from what are observed in this thesis which can further reveal the possible mechanisms governing the wear of DLC and SiN_x in AM-AFM.

APPENDIX

The custom MATLAB script written to apply the solution of an adhesive axisymmetric arbitrary punch to the AFM actual profile is presented here. It should be mentioned here that this script can be modified to perform computationally more effective.

```
function Arbit_punch_ContactMech
%%%%%%%%%%%%%%%%%%%%%%%%%%%%%%%%%%%%%%%%%%%%%%%%%%%%%%%%%%%%%%%%%%%%%%%
%
%
%     This function reads the profile of an arbitrary punch as a text
%     or ascii file and takes the normal applied force as an input.
%     Then, it calculates contact radius, indentation and stress
%     profile. These values are calculated for the left and right
%     profiles of the arbitrary punch, separately. In other words, this
%     code divides the entire tip profile at the point of contact and
%     treats each side as a separate axisymmetric punch. This is based
%     on a solution proposed by S.-S. Zhou et al., "J. Mech. Phys.
%     Solids 59 (2011) 145-159", for the adhesive frictionless contact
%     of an axisymmetric arbitrary punch.
%
%
%%%%%%%%%%%%%%%%%%%%%%%%%%%%%%%%%%%%%%%%%%%%%%%%%%%%%%%%%%%%%%%%%%%%%%%

clear;
close all;
clc;


%%Enter estimated tip radius of the AFM tip estimated through
%circle/parabola fit

R = 17; %in (nm)  %TEM tip radius or tip radius in y direction

%%Enter material properties

E_t = 150;    %Young's Modulus (GPa) of the Tip
E_s = 790;    %Young's Modulus (GPa) of the Sample

Nu_t= 0.23;  %Poisson's ratio of the Tip
Nu_s= 0.057; %Poisson's ratio of the Tip Sample
```

```
Ec=1/((1-Nu_t^2)/E_t+(1-Nu_s^2)/E_s);  %in (GPa), composite/reduced
                                       %Young's modulus


%%
%%Load, read, and interpolate the punch profile
[filename, pathname] = uigetfile({'*.txt;*.asc'}, 'Pick a text/ascii
file for the punch profile');
[head,data] = hdrload([pathname,filename]);
Profile = data;

Profile = flipud(Profile);

%%
% Adjust data points that do not follow ascending/descending nature of
% the right/left side of the profile.

[MinY,K] = min(Profile(:,2));

IT = 30;    %# of iteration

%Adjust the y-coordinates of the data points in a way that all the
%y-coordinates are ascending (right profile) or descending (right
%profile)

for j = 1:IT                %left profile
    for i = (K-1):-1:2
        if Profile(i,2) >= Profile(i-1,2)
            Profile(i,2) = Profile(i,2) - (Profile(i,2)-Profile(i- …
            1,2))/3;
            Profile(i-1,2) = Profile(i-1,2) + 2*(Profile(i,2)- …
            Profile(i-1,2))/3 + 0.02;
        end
    end
end

for l = 1:IT                 %right profile
    for m = K:length(Profile(:,2))-1
        if Profile(m,2)  >= Profile(m+1,2)
            Profile(m,2) = Profile(m,2) - 2*(Profile(m,2)- …
            Profile(m+1,2))/3;
            Profile(m+1,2) = Profile(m+1,2) + (Profile(m,2)- …
            Profile(m+1,2))/3 + 0.02;
        end
    end
end


%Adjust the x-coordinates of the data points in a way that all the
%x-coordinates are ascending

for j = 1:IT                %left profile
```

```
        for i = (K-1):-1:2
            if Profile(i-1,1) >= Profile(i,1)
                Profile(i-1,1) = Profile(i-1,1) - (Profile(i-1,1)- …
                Profile(i,1))/3;
                Profile(i,1) = Profile(i,1) + 2*(Profile(i-1,1)- …
                Profile(i,1))/3 + 0.02;
            end
        end
    end

    for l = 1:IT                %right profile
        for m = K:length(Profile(:,1))-1
            if Profile(m,1) >= Profile(m+1,1)
                Profile(m,1) = Profile(m,1) - 2*(Profile(m,1)- …
                Profile(m+1,1))/3;
                Profile(m+1,1) = Profile(m+1,1) + (Profile(m,1)- …
                Profile(m+1,1))/3 + 0.02;
            end
        end
    end


    %%
    % Here we interpolate the profile using two different methods and then
    % take an average of the resulting interpolations to get a smoother
    % profile

    ppS = interp1(Profile(:,1),Profile(:,2),'spline','pp');
    Prof(:,1) = Profile(1,1):0.002:Profile(end,1);
    ProfS(:,2) = ppval(ppS,Prof);

    ppC = interp1(Profile(:,1),Profile(:,2),'cubic','pp');
    ProfC(:,2) = ppval(ppC,Prof);

    Prof(:,2) = (ProfS(:,2)+2*ProfC(:,2))/3;

    figure;
    plot(Prof(:,1),Prof(:,2),'-r','LineWidth',3), hold on,
    plot(Profile(:,1),Profile(:,2),'k.','MarkerSize',20), hold off
    xlabel('\bf (nm)')
    ylabel('\bf (nm)')
    axis image
```

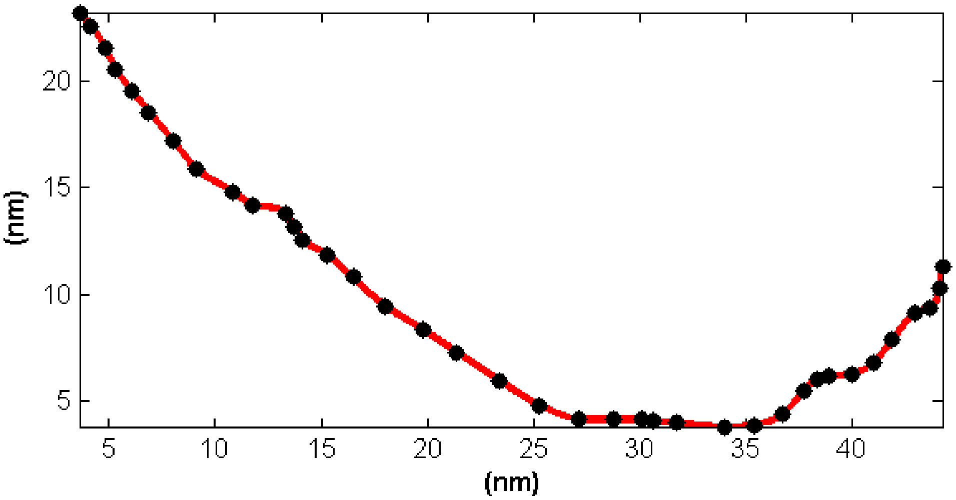

```
%%
%%Find the lowest data point, initial contact point, shift it to the
%origin,(0,0), along with the rest of profile, and divide the profile
into half

[MinY,I] = min(Prof(:,2));

Prof(:,1) = Prof(:,1)-Prof(I,1);
Prof(:,2) = Prof(:,2)-Prof(I,2);

figure;
plot(Prof(1:I,1),Prof(1:I,2),'-b','LineWidth',4), hold
on,plot(Prof(I:end,1),Prof(I:end,2),'-g','LineWidth',4), hold off
xlabel('\bf (nm)')
ylabel('\bf (nm)')
axis image
```

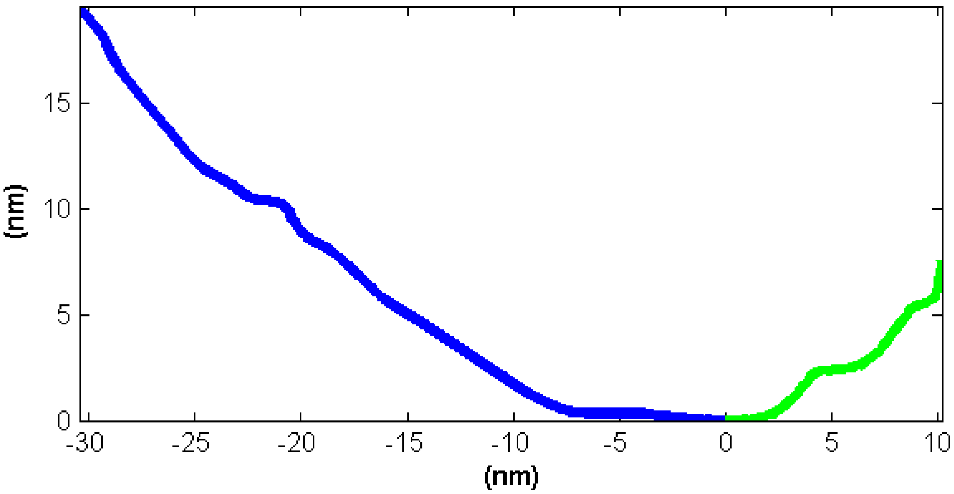

```
ProfR = Prof(I:end,:); %right profile
ProfL = Prof(1:I,:); %left profile

%%
%%Equalize the length of the right and left profiles
RR = length(ProfR(:,1));
LL = length(ProfL(:,1));

if LL > RR
    ProfL = ProfL(I-RR+1:I,:);
elseif LL < RR
    ProfR = ProfR(1:LL,:);
end

figure;
plot(ProfR(:,1),ProfR(:,2),ProfL(:,1),ProfL(:,2))
```

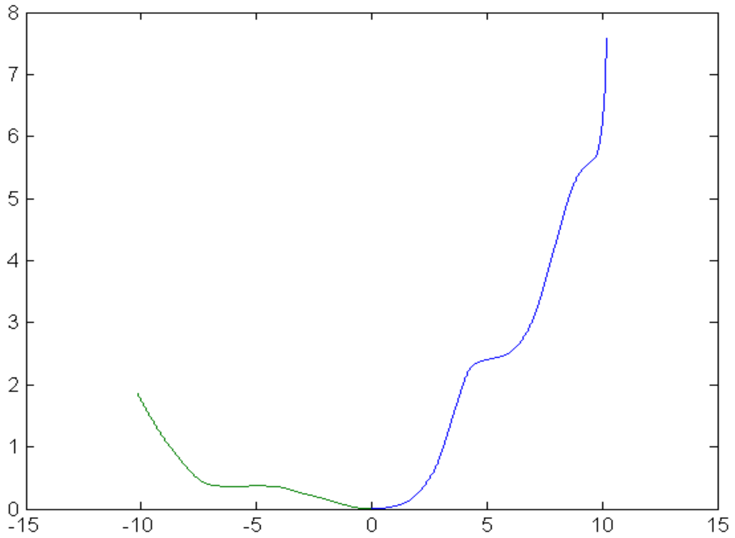

```
%%Ask for total applied load
Load = (inputdlg('Enter the total applied load (nN):','L',1,{''}));
L = eval(Load{1});   %in (nN)



%% solve for the right profile

%%Take the derivative of the profile and add a zero element to the
%beginning of the derivative array. Adding zero guarantees that the
%slope is zero at the point of contact

ProfRd = diff(ProfR(:,2))./diff(ProfR(:,1));

ProfRdd = zeros(length(ProfRd)+1,1);
ProfRdd(2:end) = ProfRd(1:end);
```

```
[ProfRdd] = movAvg(ProfRdd,10);


%%Calculate the contact radius

for i=3:length(ProfR(:,1))
    IntegrandA_R = (ProfR(1:i-1,1).^2).*ProfRdd(1:i-
1)./sqrt(ProfR(i,1)^2-ProfR(1:i-1,1).^2);
    Equn(i-2) = L - 2*Ec*trapz(ProfR(1:i-1,1),IntegrandA_R);
end

[MinE,II] = min (abs(Equn));

a_R = ProfR(II+2,1)  %in (nm), estimated contact radius


%%Calculate the indentation

IntegrandD_R = a_R*ProfRdd(1:II+1)./sqrt(a_R^2-ProfR(1:II+1,1).^2);
Delta_R = trapz(ProfR(1:II+1,1),IntegrandD_R) %in (nm), estimated
                                              %indentation

%%Calculate normal stress profile at z=0

tProfRdd = ProfR(:,1).*ProfRdd;  %this is tf'(t)

DtProfRdd = diff(tProfRdd)./diff(ProfR(:,1)); %this is [tf'(t)]'
[DtProfRdd] = movAvg(DtProfRdd,10);

XX = ProfR(1:II+2,1);
                      % in the following loop XX represents x in the
                      % equation 35a, which is a constant in inner
                      % integral

for kk = 3:length(XX)
    IntegrandSt_R = DtProfRdd(1:kk-1)./sqrt((XX(kk)^2-ProfR(1:kk- …
    1,1).^2));
    IntegrandSSt_R(kk-2) = trapz(ProfR(1:kk-1,1),IntegrandSt_R);
end
IntegrandSSt_R = IntegrandSSt_R';

                      % in the following loop XX represents r in the
                      % equation 35a, which is a constant in the outer
                      % integral

for jj = 2:length(XX)-3
    IntegrandSStt_R = (1./(sqrt((ProfR(jj:II,1).^2-XX(jj- …
    1)^2)))).*IntegrandSSt_R(jj:II);
    Sigma_zz_r_R(jj-1) = (Ec/pi)*trapz(ProfR(jj:II,1),IntegrandSStt_R);
end
```

```
Sigma_zz_r_R = Sigma_zz_r_R';

Sigma_zz_max_R = Sigma_zz_r_R(1)

figure;
plot(ProfR(1:II-2,1),Sigma_zz_r_R)
```

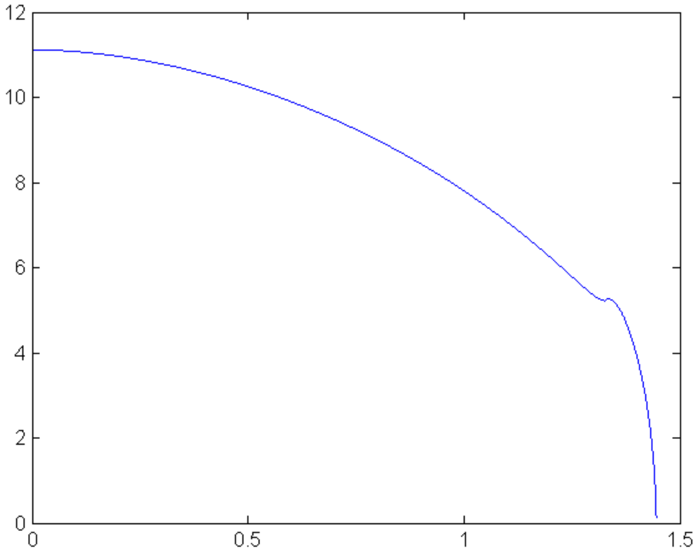

```
%% solve for the left profile

%Reflect the left profile to the other side (mirror)

ProfL(:,1) = -ProfL(:,1);
ProfL = flipud(ProfL);


%Take the derivative of the profile and add a zero element to the
%beginning of the derivative array. Adding zero guarantees that the
%slope is zero at the point of contact

ProfLd = diff(ProfL(:,2))./diff(ProfL(:,1));

ProfLdd = zeros(length(ProfLd)+1,1);
ProfLdd(2:end) = ProfLd(1:end);
[ProfLdd] = movAvg(ProfLdd,10);


%%Calculate the contact radius

for i=3:length(ProfL(:,1))
    IntegrandA_L = (ProfL(1:i-1,1).^2).*ProfLdd(1:i- …
```

```
    1)./sqrt(ProfL(i,1)^2-ProfL(1:i-1,1).^2);
    Equn(i-2) = L - 2*Ec*trapz(ProfL(1:i-1,1),IntegrandA_L);
end

[MinE,JJ] = min (abs(Equn));
a_L = ProfL(JJ+2,1)  %in (nm), estimated contact radius


%%Calculate the indentation

IntegrandD_L = a_L*ProfLdd(1:JJ+1)./sqrt(a_L^2-ProfL(1:JJ+1,1).^2);
Delta_L = trapz(ProfL(1:JJ+1,1),IntegrandD_L) %in (nm), estimated
                                              %indentation


%%Calculate normal stress profile at z=0


tProfLdd = ProfL(:,1).*ProfLdd;  %this is tf'(t)

DtProfLdd = diff(tProfLdd)./diff(ProfL(:,1)); %this is [tf'(t)]'
[DtProfLdd] = movAvg(DtProfLdd,10);

XX = ProfL(1:JJ+2,1);
                      % in the following loop XX represents x in the
                      % equation 35a, which is a constant in inner
                      % integral

for kk = 3:length(XX)
    IntegrandSt_L = DtProfLdd(1:kk-1)./sqrt((XX(kk)^2-ProfL(1:kk- …
    1,1).^2));
    IntegrandSSt_L(kk-2) = trapz(ProfL(1:kk-1,1),IntegrandSt_L);
end
IntegrandSSt_L = IntegrandSSt_L';

                      % in the following loop XX represents r in the
                      % equation 35a, which is a constant in the outer
                      % integral


for jj = 2:length(XX)-3
    IntegrandSStt_L = (1./(sqrt((ProfL(jj:JJ,1).^2-XX(jj- …
    1)^2)))).*IntegrandSSt_L(jj:JJ);
    Sigma_zz_r_L(jj-1) = (Ec/pi)*trapz(ProfL(jj:JJ,1),IntegrandSStt_L);
end

Sigma_zz_r_L = Sigma_zz_r_L';
Sigma_zz_max_L = Sigma_zz_r_L(1)

figure;
plot(ProfL(1:JJ-2,1),Sigma_zz_r_L)
```

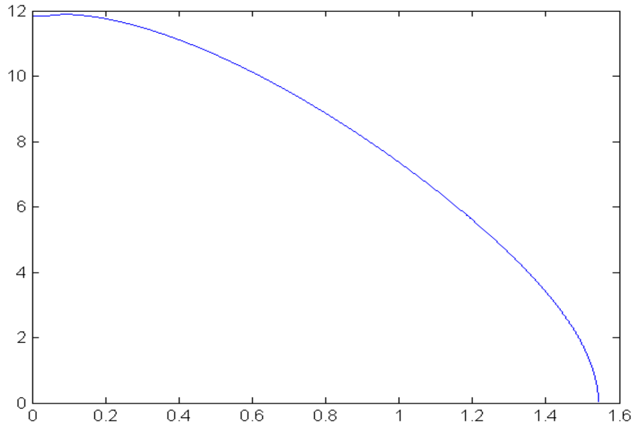

```
%% solve for the average profile
%Reflect the left profile to the other side (mirror)

ProfAV = (ProfL + ProfR)/2;

figure;
plot(ProfR(:,1),ProfR(:,2),'g.',ProfL(:,1),ProfL(:,2),'b.',ProfAV(:,1),
ProfAV(:,2),'r.')
legend('Right Profile','Left Profile','Average Profile')
```

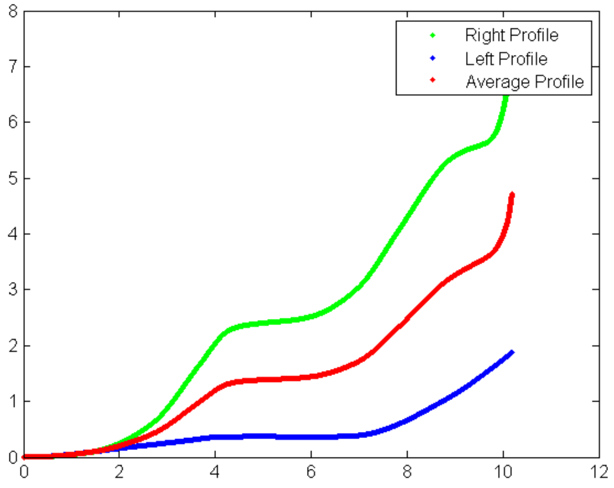

```
%Take the derivative of the profile and add a zero element to the
%begining of the derivative array. Adding zero gaurantees that the
%slope is zero at the point of contact

ProfAVd = diff(ProfAV(:,2))./diff(ProfAV(:,1));
ProfAVdd = zeros(length(ProfAVd)+1,1);
```

```
ProfAVdd(2:end) = ProfAVd(1:end);
[ProfAVdd] = movAvg(ProfAVdd,10);


%%Calculate the contact radius

for i=3:length(ProfAV(:,1))
    IntegrandA_AV = (ProfAV(1:i-1,1).^2).*ProfAVdd(1:i- …
    1)./sqrt(ProfAV(i,1)^2-ProfAV(1:i-1,1).^2);
    Equn(i-2) = L - 2*Ec*trapz(ProfAV(1:i-1,1),IntegrandA_AV);
end
[MinE,KK] = min (abs(Equn));
a_AV = ProfAV(KK+2,1)  % nm, estimated contact radius


%%Calculate the indentation

IntegrandD_AV = a_AV*ProfAVdd(1:KK+1)./sqrt(a_AV^2- …
ProfAV(1:KK+1,1).^2);
Delta_AV = trapz(ProfAV(1:KK+1,1),IntegrandD_AV) %nm, estimated
indentation


%%Calculate normal stress profile at z=0

tProfAVdd = ProfAV(:,1).*ProfAVdd;  %this is tf'(t)
DtProfAVdd = diff(tProfAVdd)./diff(ProfAV(:,1)); %this is [tf'(t)]'
[DtProfAVdd] = movAvg(DtProfAVdd,10);

XX = ProfAV(1:KK+2,1);
                      % in the following loop XX represents x in the
                      % equation 35a, which is a constant in the inner
                      % integaral

for kk = 3:length(XX)
    IntegrandSt_AV = DtProfAVdd(1:kk-1)./sqrt((XX(kk)^2-ProfAV(1:kk-…
    1,1).^2));
    IntegrandSSt_AV(kk-2) = trapz(ProfAV(1:kk-1,1),IntegrandSt_AV);
end
IntegrandSSt_AV = IntegrandSSt_AV';

                      % in the following loop XX represents r in the
                      % equation 35a, which is a constant in the outer
                      % integral

for jj = 2:length(XX)-3
    IntegrandSStt_AV = (1./(sqrt((ProfAV(jj:KK,1).^2-XX(jj- …
    1)^2)))).*IntegrandSSt_AV(jj:KK);
    Sigma_zz_r_AV(jj-1) =
(Ec/pi)*trapz(ProfAV(jj:KK,1),IntegrandSStt_AV);
end
```

```
Sigma_zz_r_AV = Sigma_zz_r_AV';
Sigma_zz_max_AV = Sigma_zz_r_AV(1)


figure;
plot(ProfAV(1:KK-2,1),Sigma_zz_r_AV)
```

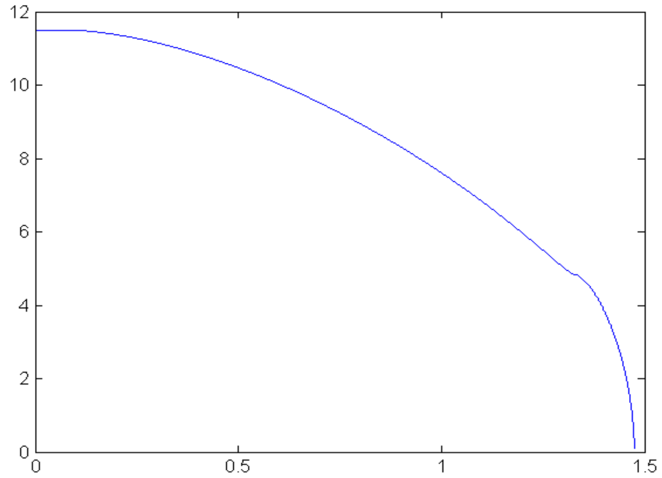

```
%% Hertzian Solution for the profile

a_Hertz = (3*R*L/(4*Ec))^(1/3)
Delta_Hertz = ((9*L^2)/(16*R*Ec^2))^(1/3)
Sigma_zz_max_Hertz = (3/(2*pi))*(4*Ec/(3*R))^(2/3)*L^(1/3)

r = 0.0001:0.0001:a_Hertz;

Sigma_zz_r_Hertz = Sigma_zz_max_Hertz*(1-(r/a_Hertz).^2).^(1/2);

figure;
plot(r,Sigma_zz_r_Hertz,'k.',ProfAV(1:KK-
2,1),Sigma_zz_r_AV,'r.',ProfR(1:II-2,1),Sigma_zz_r_R,'g.',ProfL(1:JJ-
2,1),Sigma_zz_r_L,'b.')
xlabel('\bf r (nm)')
ylabel('\bf \sigma_z_z (GPa)')
legend('Fitted Circle','Average Profile','Right Profile','Left
Profile')
```

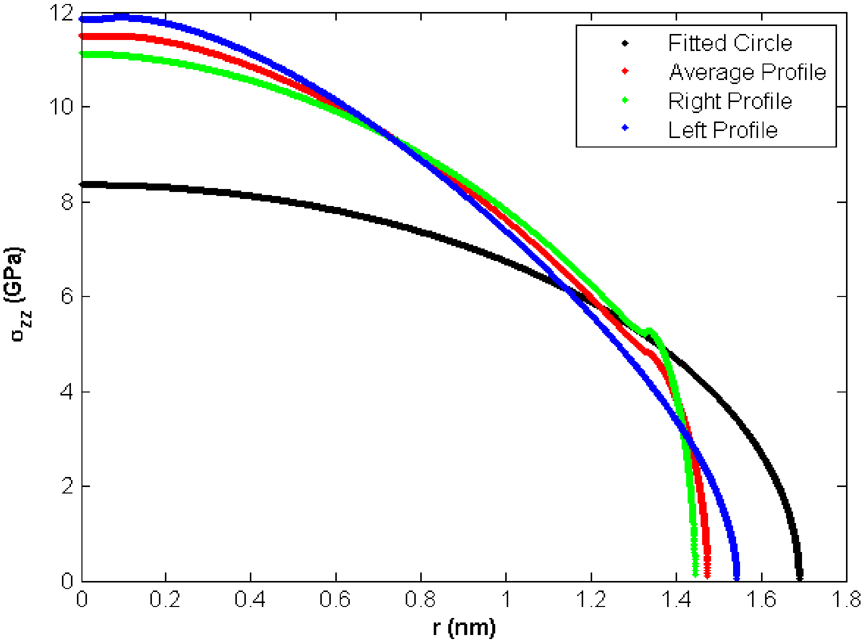

```
%% HEADER LOAD FUNCTION
**********************************************
function [header, data] = hdrload(file)

% HDRLOAD Load data from an ASCII file containing a text header.
%     [header, data] = HDRLOAD('filename.txt') reads a data file
%     called 'filename.txt', which contains a text header.  There
%     is no default extension; any extensions must be explicitly
%     supplied.
%
%     The first output, HEADER, is the header information,
%     returned as a text array.
%     The second output, DATA, is the data matrix.  This data
%     matrix has the same dimensions as the data in the file, one
%     row per line of ASCII data in the file.  If the data is not
%     regularly spaced (i.e., each line of ASCII data does not
%     contain the same number of points), the data is returned as
%     a column vector.
%
%     Limitations:  No line of the text header can begin with
%     a number.  Only one header and data set will be read,
%     and the header must come before the data.
%
%     See also LOAD, SAVE, SPCONVERT, FSCANF, FPRINTF, STR2MAT.
%     See also the IOFUN directory.

% check number and type of arguments
if nargin < 1
  error('Function requires one input argument');
elseif ~isstr(file)
```

```
  error('Input must be a string representing a filename');
end

% Open the file.  If this returns a -1, we did not open the file
% successfully.
fid = fopen(file);
if fid==-1
  error('File not found or permission denied');
  end

% Initialize loop variables
% We store the number of lines in the header, and the maximum
% length of any one line in the header.  These are used later
% in assigning the 'header' output variable.
no_lines = 0;
max_line = 0;

% We also store the number of columns in the data we read.  This
% way we can compute the size of the output based on the number
% of columns and the total number of data points.
ncols = 0;

% Finally, we initialize the data to [].
data = [];

% Start processing.
line = fgetl(fid);
if ~isstr(line)
  disp('Warning: file contains no header and no data')
  end;
[data, ncols, errmsg, nxtindex] = sscanf(line, '%f');

% One slight problem, pointed out by Peter vanderWal: If the
% first character of the line is 'e', then this will scan as
% 0.00e+00. We can trap this case specifically by using the
% 'next index' output: in the case of a stripped 'e' the next
% index is one, indicating zero characters read.  See the help
% entry for 'sscanf' for more information on this output
% parameter. We loop through the file one line at a time until
% we find some data.  After that point we stop checking for
% header information. This part of the program takes most of the
% processing time, because fgetl is relatively slow (compared to
% fscanf, which we will use later).
while isempty(data)|(nxtindex==1)
  no_lines = no_lines+1;
  max_line = max([max_line, length(line)]);
  % Create unique variable to hold this line of text information.
  % Store the last-read line in this variable.
  eval(['line', num2str(no_lines), '=line;']);
  line = fgetl(fid);
  if ~isstr(line)
    disp('Warning: file contains no data')
    break
```

```
    end;
  [data, ncols, errmsg, nxtindex] = sscanf(line, '%f');
  end % while

% Now that we have read in the first line of data, we can skip
% the processing that stores header information, and just read
% in the rest of the data.
data = [data; fscanf(fid, '%f')];
fclose(fid);

% Create header output from line information. The number of lines
% and the maximum line length are stored explicitly, and each
% line is stored in a unique variable using the 'eval' statement
% within the loop. Note that, if we knew a priori that the
% headers were 10 lines or less, we could use the STR2MAT
% function and save some work. First, initialize the header to an
% array of spaces.
header = setstr(' '*ones(no_lines, max_line));
for i = 1:no_lines
  varname = ['line' num2str(i)];
  % Note that we only assign this line variable to a subset of
  % this row of the header array.  We thus ensure that the matrix
  % sizes in the assignment are equal. We also consider blank
  % header lines using the following IF statement.
  if eval(['length(' varname ')~=0'])
    eval(['header(i, 1:length(' varname ')) = ' varname ';']);
    end
  end % for

% Resize output data, based on the number of columns (as returned
% from the sscanf of the first line of data) and the total number
% of data elements. Since the data was read in row-wise, and
% MATLAB stores data in columnwise format, we have to reverse the
% size arguments and then transpose the data.  If we read in
% irregularly spaced data, then the division we are about to do
% will not work. Therefore, we will trap the error with an EVAL
% call; if the reshape fails, we will just return the data as is.
eval('data = reshape(data, ncols, length(data)/ncols)'';', '');


%% Moving Average Function
***********************************************
function [ys] = movAvg(y,window)

ys = zeros(size(y));
% Weighted moving average

% For testing

% x = 0:pi/100:2*pi; x = x';

% y = 2*cos(x)+rand(length(x'),1);
```

```
for i=1:length(y)
    sum = 0;
    n = 0;
    for j = -window:1:window
        if i+j>=1 && i+j<=length(y)
            n = n+1;
            sum = sum + y(i+j);
        end
    end

    ys(i,1) = sum/n;
end
```

BIBLIOGRAPHY

1. Binnig, G.; Quate, C. F.; Gerber, C. Atomic Force Microscope. *physical review letters* **1986**, *56*, 930–933.

2. Liu, Z.; Li, Z.; Wei, G.; Song, Y.; Wang, L. I.; Sun, L. Manipulation , Dissection , and Lithography Using Modified Tapping Mode Atomic Force Microscope. **2006**, *69*, 998–1004.

3. Wang, Y.; Hong, X.; Zeng, J.; Liu, B.; Guo, B.; Yan, H. AFM Tip Hammering Nanolithography. *Small* **2009**, *5*, 477–83.

4. Paolicelli, G.; Mougin, K.; Vanossi, a; Valeri, S. Adhesion Detachment and Movement of Gold Nanoclusters Induced by Dynamic Atomic Force Microscopy. *Journal of Physics: Condensed Matter* **2008**, *20*, 354011.

5. Martínez, N. F.; Kamiński, W.; Gómez, C. J.; Albonetti, C.; Biscarini, F.; Pérez, R.; García, R. Molecular Scale Energy Dissipation in Oligothiophene Monolayers Measured by Dynamic Force Microscopy. *Nanotechnology* **2009**, *20*, 434021.

6. Dietz, C.; Zerson, M.; Riesch, C.; Franke, M.; Magerle, R. Surface Properties of Elastomeric Polypropylenes Studied with Atomic Force Microscopy. *Macromolecules* **2008**, *41*, 9259–9266.

7. Solares, S. D. Characterization of Deep Nanoscale Surface Trenches with AFM Using Thin Carbon Nanotube Probes in Amplitude-modulation and Frequency-force-modulation Modes. *Measurement Science and Technology* **2008**, *19*, 015503.

8. Martin, Y.; Williams, C.; Wickramasinghe, H. Atomic Force Microscope-force Mapping and Profilling on a Sub 100-Angstom Scale. *J. Appl. Phys.* **1987**, *61*, 4723–9.

9. Johnson, K. L. *Contact Mechanics*; Cambridge University Press, 1985.

10. Johnson, K.; Kendall, K.; Roberts, A. D. Surface energy and the contact of elastic solids. In *Proc. R. Soc. Lond. A.*; 1971; Vol. 324, pp. 301–313.

11. Derjaguin, B. .; Muller, V. .; Toporov, Y. . Effect of Contact Deformations on the Adhesion of Particles. *Journal of Colloid and Interface Science* **1975**, *53*, 314–326.

12. Luan, B.; Robbins, M. O. The Breakdown of Continuum Models for Mechanical Contacts. *Nature* **2005**, *435*, 929–32.

13. Liu, J.; Grierson, D. S.; Moldovan, N.; Notbohm, J.; Li, S.; Jaroenapibal, P.; O’Connor, S. D.; Sumant, a V; Neelakantan, N.; Carlisle, J. a; *et al.* Preventing Nanoscale Wear of Atomic Force Microscopy Tips Through the Use of Monolithic Ultrananocrystalline Diamond Probes. *Small* **2010**, *6*, 1140–9.

14. Liu, J.; Notbohm, J. K.; Carpick, R. W.; Turner, K. T. Method for Characterizing Nanoscale Wear of Atomic Force Microscope Tips. *ACS nano* **2010**, *4*, 3763–72.

15. Fletcher, P. C.; Felts, J. R.; Dai, Z.; Jacobs, T. D.; Zeng, H.; Lee, W.; Sheehan, P. E.; Carlisle, Ḱ. J. A.; Carpick, R. W.; King, W. P. Wear-Resistant Diamond Nanoprobe Tips with Integrated Silicon Heater for Tip-Based Nanomanufacturing. *ACS nano* **2010**, *4*, 3338–3344.

16. Gotsmann, B.; Lantz, M. Atomistic Wear in a Single Asperity Sliding Contact. *Physical Review Letters* **2008**, *101*, 125501.

17. Bhaskaran, H.; Gotsmann, B.; Sebastian, A.; Drechsler, U.; Lantz, M. a; Despont, M.; Jaroenapibal, P.; Carpick, R. W.; Chen, Y.; Sridharan, K. Ultra-low Nanoscale Wear Through Atom-by-atom Attrition in Silicon-containing Diamond-like Carbon. *Nature nanotechnology* **2010**, *5*, 181–5.

18. Jacobs, T. D. B.; Gotsmann, B.; Lantz, M. a.; Carpick, R. W. On the Application of Transition State Theory to Atomic-Scale Wear. *Tribology Letters* **2010**, *39*, 257–271.

19. Auciello, O.; Birrell, J.; Carlisle, J. a; Gerbi, J. E.; Xiao, X.; Peng, B.; Espinosa, H. D. Materials Science and Fabrication Processes for a New MEMS Technology Based on Ultrananocrystalline Diamond Thin Films. *Journal of Physics: Condensed Matter* **2004**, *16*, R539–R552.

20. Chung, K.-H.; Lee, Y.-H.; Kim, D.-E. Characteristics of Fracture During the Approach Process and Wear Mechanism of a Silicon AFM Tip. *Ultramicroscopy* **2005**, *102*, 161–71.

21. Merkle, A. P.; Marks, L. D. Liquid-like Tribology of Gold Studied by in Situ TEM. *Wear* **2008**, *265*, 1864–1869.

22. Jacobs, T. D. B.; Carpick, R. W. Nanoscale Wear as a Stress-assisted Chemical Reaction. *Nature nanotechnology* **2013**, *8*, 108–12.

23. Ho, H. J. Near-Contact Mode: A novel AFM operation mode for non-destructive, ultra-high lateral resolution topography measurement in air. In *Proceedings of SPIE*; 1998; Vol. 3512, pp. 40–53.

24. Chung, K.; Lee, Y.; Kim, D.; Yoo, J.; Hong, S. Tribological Characteristics of Probe Tip and PZT Media for AFM-based Recording Technology. *IEEE Transactions on Magnetics* **2005**, *41*, 849–854.

25. Nie, H.-Y.; McIntyre, N. S. Unstable Amplitude and Noisy Image Induced by Tip Contamination in Dynamic Force Mode Atomic Force Microscopy. *Review of Scientific Instruments* **2007**, *78*, 023701.

26. Kim, H. J.; Moldovan, N.; Felts, J. R.; Somnath, S.; Dai, Z.; Jacobs, T. D. B.; Carpick, R. W.; Carlisle, J. a; King, W. P. Ultrananocrystalline Diamond Tip

Integrated onto a Heated Atomic Force Microscope Cantilever. *Nanotechnology* **2012**, *23*, 495302.

27. Qian, L.; Xiao, X.; Wen, S. Tip in Situ Chemical Modification and Its Effects on Tribological Measurements. *Langmuir* **2000**, *16*, 662–670.

28. *A Practical Guide to Scanning Probe Microscopy*; Veeco Instruments Inc., 2005.

29. García, R.; Paulo, A. S. Attractive and Repulsive Tip-sample Interaction Regimes in Tapping-mode Atomic Force Microscopy. *Physical Review B* **1999**, *60*, 4961–4967.

30. García, R.; Perez, R. Dynamic Atomic Force Microscopy Methods. *Surface science reports* **2002**, *47*, 197–301.

31. García, R.; Paulo, A. S. Dynamics of a Vibrating Tip Near or in Intermittent Contact with a Surface. *Physical Review B* **2000**, *61*, 381–384.

32. Doris, B. B.; Hegde, R. I. Improved Atomic Force Microscopy Imaging Using Carbon-coated Probe Tips. *Applied Physics Letters* **1995**, *67*, 3816.

33. Larsen, T.; Moloni, K.; Flack, F.; Eriksson, M. a.; Lagally, M. G.; Black, C. T. Comparison of Wear Characteristics of Etched-silicon and Carbon Nanotube Atomic-force Microscopy Probes. *Applied Physics Letters* **2002**, *80*, 1996.

34. Su, C.; Huang, L.; Kjoller, K.; Babcock, K. Studies of Tip Wear Processes in Tapping Mode^{TM} Atomic Force Microscopy. *Ultramicroscopy* **2003**, *97*, 135–144.

35. Bassani, R.; D'Acunto, M. Nanotribology : Tip – Sample Wear Under Adhesive Contact. *Tribology international* **2000**, *33*, 443–452.

36. Tello, M.; Paulo, A. S.; Rodríguez, T. R.; Blanco, M. C.; García, R. Imaging Cobalt Nanoparticles by Amplitude Modulation Atomic Force Microscopy: Comparison Between Low and High Amplitude Solutions. *Ultramicroscopy* **2003**, *97*, 171–175.

37. Chen, L.; Cheung, C. L.; Ashby, P. D.; Lieber, C. M. Single-Walled Carbon Nanotube AFM Probes : Optimal Imaging Resolution of Nanoclusters and Biomolecules in Ambient and Fluid Environments. *Nano Letters* **2004**, *4*, 1725–1731.

38. Katan, A. J.; Es, M. H. van; Oosterkamp, T. H. Quantitative Force Versus Distance Measurements in Amplitude Modulation AFM: a Novel Force Inversion Technique. *Nanotechnology* **2009**, *20*, 165703.

39. Katan, A. J. Exploring the Limints of Amplitude Modulation Force Spectroscopy with Numerical Experiments. In *Measuring interactions in fluids with small-cantilever AFM*; PhD Thesis, Leiden University, Leiden, Netherlands, 2007; pp. 65–82.

40. Hu, S. Analytical Formulas and Scaling Laws for Peak Interaction Forces in Dynamic Atomic Force Microscopy. In *Nonlinear dynamics and force spectroscopy in dynamic atomic force microscopy*; PhD Thesis, Purdue University, West Lafayette, Indiana, 2007; pp. 74–101.

41. Melcher, J.; Kiracofe, D.; Hu, S.; Raman, A. VEDA 2.0 (Virtual Environment for Dynamic AFM) **2012**.

42. Sader, J. E.; Uchihashi, T.; Higgins, M. J.; Farrell, A.; Nakayama, Y.; Jarvis, S. P. Quantitative Force Measurements Using Frequency Modulation Atomic Force Microscopy-theoretical Foundations. *Nanotechnology* **2005**, *16*, S94–S101.

43. Johnson, K. L.; Greenwood, J. A. An Adhesion Map for the Contact of Elastic Spheres. *Journal of Colloid and Interface Science* **1997**, *192*, 326–333.

44. Grierson, D. S.; Flater, E. E.; Carpick, R. W. Accounting for the JKR–DMT Transition in Adhesion and Friction Measurements with Atomic Force Microscopy. *Journal of Adhesion Science and Technology* **2005**, *19*, 291–311.

45. Zhou, S.-S.; Gao, X.-L.; He, Q.-C. A Unified Treatment of Axisymmetric Adhesive Contact Problems Using the Harmonic Potential Function Method. *Journal of the Mechanics and Physics of Solids* **2011**, *59*, 145–159.

46. Szoszkiewicz, R.; Riedo, E. Nucleation Time of Nanoscale Water Bridges. *Physical Review Letters* **2005**, *95*, 135502.

47. Restagno, F.; Bocquet, L.; Biben, T. Metastability and Nucleation in Capillary Condensation. *Physical review letters* **2000**, *84*, 2433–6.

48. Sahagún, E.; García-Mochales, P.; Sacha, G.; Sáenz, J. Energy Dissipation Due to Capillary Interactions: Hydrophobicity Maps in Force Microscopy. *Physical Review Letters* **2007**, *98*, 176106.

49. Zitzler, L.; Herminghaus, S.; Mugele, F. Capillary Forces in Tapping Mode Atomic Force Microscopy. *Physical Review B* **2002**, *66*, 155436.

50. Petersen, K. E. Silicon as a Mechanical Material. In *Proceedings of the IEEE*; 1982; pp. 420–456.

51. Gan, Z.; Zhang, Y.; Yu, G.; Tan, C.; Lau, S.; Tay, B. Intrinsic Mechanical Properties of Diamond-like Carbon Thin Films Deposited by Filtered Cathodic Vacuum Arc. *Journal of Applied Physics* **2004**, *95*, 3509.

52. Bares, J. a.; Sumant, A. V.; Grierson, D. S.; Carpick, R. W.; Sridharan, K. Small Amplitude Reciprocating Wear Performance of Diamond-like Carbon Films: Dependence of Film Composition and Counterface Material. *Tribology Letters* **2007**, *27*, 79–88.

53. Marques, F. C.; Lacerda, R. G.; Champi, a.; Stolojan, V.; Cox, D. C.; Silva, S. R. P. Thermal Expansion Coefficient of Hydrogenated Amorphous Carbon. *Applied Physics Letters* **2003**, *83*, 3099.

54. Olliges, S.; Frank, S.; Gruber, P. a.; Auzelyte, V.; Solak, H.; Spolenak, R. Thermo Mechanical Properties and Plastic Deformation of Gold Nanolines and Gold Thin Films. *Materials Science and Engineering: A* **2011**, *528*, 6203–6209.

55. Horiuchi, S.; Hanada, T.; Ebisawa, M.; Matsuda, Y.; Kobayashi, M.; Takahara, A. Contamination-Free Transmission Electron Microscopy for High-Resolution Carbon Elemental Mapping of Polymers. *ACS nano* **2009**, *3*, 1297–1304.

56. Sader, J. E.; Chon, J. W. M.; Mulvaney, P. Calibration of Rectangular Atomic Force Microscope Cantilevers. *Review of Scientific Instruments* **1999**, *70*, 3967.

57. Hutter, J. L.; Bechhoefer, J. Calibration of Atomic-force Microscope Tips. *Review of Scientific Instruments* **1993**, *64*, 1868–73.

58. Martínez, N. F.; García, R. Measuring Phase Shifts and Energy Dissipation with Amplitude Modulation Atomic Force Microscopy. *Nanotechnology* **2006**, *17*, S167–72.

59. Robertson, J. Diamond-like Amorphous Carbon. *Materials Science and Engineering: R: Reports* **2002**, *37*, 129–281.

60. Khan, A.; Philip, J.; Hess, P. Young’s Modulus of Silicon Nitride Used in Scanning Force Microscope Cantilevers. *Journal of Applied Physics* **2004**, *95*, 1667.

61. Dai, C.-L.; Chang, Y.-M. A Resonant Method for Determining Mechanical Properties of Si3N4 and SiO2 Thin Films. *Materials Letters* **2007**, *61*, 3089–3092.

62. Chuang, W.; Luger, T.; Fettig, R. K.; Ghodssi, R. Mechanical Property Characterization of LPCVD Silicon Nitride Thin Films at Cryogenic Temperatures. *Journal of Microelectromechanical Systems* **2004**, *13*, 870–879.

63. Edwards, R. L.; Coles, G.; Sharpe, W. N. Comparison of Tensile and Bulge Tests for Thin-Film Silicon Nitride. *Experimental Mechanics* **2004**, *44*, 49–54.

64. Adiga, V.; Sumant, A.; Suresh, S.; Gudeman, C.; Auciello, O.; Carlisle, J.; Carpick, R. Mechanical Stiffness and Dissipation in Ultrananocrystalline Diamond Microresonators. *Physical Review B* **2009**, *79*, 245403.

65. Howard-Knight, J. P.; Hobbs, J. K. Finite Element Modeling of Atomic Force Microscopy Cantilever Dynamics During Video Rate Imaging. *Journal of Applied Physics* **2011**, *109*, 074309.

66. Jacobs, T. D. B.; Ryan, K. E.; Keating, P. L.; Grierson, D. S.; Lefever, J. a.; Turner, K. T.; Harrison, J. a.; Carpick, R. W. The Effect of Atomic-Scale Roughness on the Adhesion of Nanoscale Asperities: A Combined Simulation and Experimental Investigation. *Tribology Letters* **2013**, *50*, 81–93.

67. *Tribology of Diamon-Like Carbon Films*; Donnet, C.; Erdemir, A., Eds.; Springer Science: New York, NY, 2008.

68. Ronkainen, H.; Koskinen, J.; Likonen, J.; Varjus, S.; Vihersalo, J. Characterization of Wear Surfaces in Dry Sliding of Steel and Alumina on Hydrogenated and Hydrogen-free Carbon Films. *Diamond and Related Materials* **1994**, *3*, 1329–1336.

69. Donneta, C.; Belina, M.; Augea, J. C.; Martina, J. M.; Grill, A.; Patep, V. Tribochemistry of Diamond-like Carbon Coatings in Various Environments. *Surface and Coatings Technology* **1994**, *68/69*, 626–631.

70. Liu, Y.; Erdemir, A.; Meletis, E. I. A Study of the Wear Mechanism of Diamond-like Carbon Films. *Surface and Coatings Technology* **1996**, *82*, 48–56.

71. Donnet, C.; Mogne, T. Le; Ponsonnet, L.; Belin, M.; Grill, A.; Patel, V.; Jahnes, C. The Respective Role of Oxygen and Water Vapor on the Tribology of Hydrogenated Diamond-like Carbon Coatings ∗ . **1998**, *4*, 259–265.

72. Erdemir, a The Role of Hydrogen in Tribological Properties of Diamond-like Carbon Films. *Surface and Coatings Technology* **2001**, *146-147*, 292–297.

73. Tsuchitani, S.; Sogawa, Y.; Kaneko, R.; Hirono, S.; Umemura, S. Humidity Dependence of Microwear Characteristics of Amorphous Carbon Films on Silicon Substrates. *Wear* **2003**, *254*, 1042–1049.

74. Li, H.; Xu, T.; Wang, C.; Chen, J.; Zhou, H.; Liu, H. Humidity Dependence on the Friction and Wear Behavior of Diamond-like Carbon Film in Air and Nitrogen Environments. *Diamond and Related Materials* **2006**, *15*, 1585–1592.

75. Sobota, J.; Grossman, J.; Bursikova, V.; Dupak, L.; Vyskocil, J. Evaluation of Hardness, Tribological Behaviour and Impact Load of Carbon-based Hard Composite Coatings Exposed to the Influence of Humidity. *Diamond and Related Materials* **2011**, *20*, 596–599.

76. Ronkainen, H.; Holmberg, K. *Environmental and Thermal Effects on the Tribological Performance of DLC Coatings*; Donnet, C.; Erdemir, A., Eds.; Springer Science: New York, NY, 2008; pp. 172–177.

77. Konicek, a.; Grierson, D.; Gilbert, P.; Sawyer, W.; Sumant, a.; Carpick, R. Origin of Ultralow Friction and Wear in Ultrananocrystalline Diamond. *Physical Review Letters* **2008**, *100*, 235502.

78. Konicek, a. R.; Grierson, D. S.; Sumant, a. V.; Friedmann, T. a.; Sullivan, J. P.; Gilbert, P. U. P. a.; Sawyer, W. G.; Carpick, R. W. Influence of Surface Passivation on the Friction and Wear Behavior of Ultrananocrystalline Diamond and Tetrahedral Amorphous Carbon Thin Films. *Physical Review B* **2012**, *85*, 155448.

79. Merle, B.; Göken, M. Fracture Toughness of Silicon Nitride Thin Films of Different Thicknesses as Measured by Bulge Tests. *Acta Materialia* **2011**, *59*, 1772–1779.

80. Boresi, A. P.; Schmidt, R. J. Inelastic Material Behavior. In *Advanced Mechanics of Materials*; John Wiley & Sons, Inc.: New York, NY, 2003.

81. Julian, M. M.; Gibbs, G. V. Bonding in Silicon Nitrides. *The Journal of Physical Chemistry* **1985**, *89*, 5476–5480.

82. Ohdomari, I.; Yamakoshi, Y.; Kameyama, T.; Akatsu, H. Structural Model of Amorphous Silicon Nitride. *Journal of non-crystalline solids* **1987**, *89*, 303–310.

83. Martyniuk, M.; Musca, C. A.; Dell, J. M.; Elliman, R. G.; Faraone, L. Elasto-Plastic Characterization of Low-Temperature Plasma-Deposited Silicon Nitride Thin Films Using Nanoindentation. *international journal of surface science and engineering* **2009**, *3*, 3–22.

84. Matoy, K.; Schönherr, H.; Detzel, T.; Schöberl, T.; Pippan, R.; Motz, C.; Dehm, G. A Comparative Micro-cantilever Study of the Mechanical Behavior of Silicon Based Passivation Films. *Thin Solid Films* **2009**, *518*, 247–256.

85. Martyniuk, M.; Antoszewski, J.; Walmsley, B. a.; Musca, C. a.; Dell, J. M.; Jung, Y.-G.; Lawn, B. R.; Huang, H.; Faraone, L. Determination of mechanical

properties of silicon nitride thin films using nanoindentation. In *Proceedings of SPIE*; Tchoryk, Jr., P.; Holz, B., Eds.; 2005; Vol. 5798, pp. 216–225.

86. Nastasi, M.; Kodali, P.; Walter, K. C.; Embury, J. D.; Raj, R.; Nakamura, Y. Fracture Toughness of Diamondlike Carbon Coatings. *Journal of Materials Research* **1999**, *14*, 2173–2180.

87. Archard, J. F. Contact and Rubbing of Flat Surfaces. *Journal of Applied Physics* **1953**, *24*, 981.

88. Jiang, J.; Arnell, R. The Effect of Sliding Speed on Wear of Diamond-like Carbon Coatings. *Wear* **1998**, *218*, 223–31.

89. Jacobs, T. D. B.; Carpick, R. W. Nanoscale Wear as a Stress-assisted Chemical Reaction. *Nature nanotechnology* **2013**, *8*, 108–12.

90. Lantz, M. a.; Gotsmann, B.; Jaroenapibal, P.; Jacobs, T. D. B.; O'Connor, S. D.; Sridharan, K.; Carpick, R. W. Wear-Resistant Nanoscale Silicon Carbide Tips for Scanning Probe Applications. *Advanced Functional Materials* **2012**, *22*, 1639–1645.

91. Moldovan, N.; Dai, Z.; Zeng, H.; Carlisle, J. A.; Jacobs, T. D. B.; Vahdat, V.; Grierson, D. S.; Liu, J.; Turner, K. T.; Carpick, R. W. Advances in Manufacturing of Molded Tips for Scanning Probe Microscopy. *Journal of Microelectromechanical Systems* **2012**, *21*, 431–442.

92. Sarioglu, A. F.; Liu, M.; Solgaard, O. High-Resolution Nanomechanical Mapping Using Interferometric-Force-Sensing AFM Probes. *Journal of Microelectromechanical Systems* **2011**, *20*, 654–664.

93. Chang, W. R.; Etsion, I.; Bogy, D. B. An Elastic-plastic Model for a Contact of Rough Surfaces. *Journal of Tribology* **1987**, *109*, 257–263.

94. Zhao, Y.; Maietta, M.; Chang, L. An Asperity Micro- Contact Model Incorporating the Transion from Elastic Deformation to Fully Plastic Flow. *Journal of Tribology* **2000**, *107*, 86–93.

95. Agrawal, R.; Moldovan, N.; Espinosa, H. D. An Energy-based Model to Predict Wear in Nanocrystalline Diamond Atomic Force Microscopy Tips. *Journal of Applied Physics* **2009**, *106*, 064311.

96. Carpick, R. W.; Eriksson, M. A. Measurements of In-Plane Material Properties with Scanning Probe Microscopy. *MRS Bulletin* **2004**, 472–477.

97. Paulo, A. S.; García, R. Tip-surface Forces, Amplitude, and Energy Dissipation in Amplitude-modulation (tapping Mode) Force Microscopy. *Physical Review B* **2001**, *64*, 193411.

98. Huang, S.; Zhang, S.; Belytschko, T.; Terdalkar, S. S.; Zhu, T. Mechanics of Nanocrack: Fracture, Dislocation Emission, and Amorphization. *Journal of the Mechanics and Physics of Solids* **2009**, *57*, 840–850.